REPORT DOCUMENTATION PAGE

Public reporting burden for this collection of information is estimated to average 1 hour per response, including the time for reviewing instructions, searching existing data sources, gathering and maintaining the data needed, and completing and reviewing the collection of information. Send comments regarding this burden estimate or any other aspect of this collection of information, including suggestions for reducing this burden, to Washington Headquarters Services, Directorate for Information Operations and Reports, 1215 Jefferson Davis Highway, Suite 1204, Arlington, VA 22202-4302, and to the Office of Management and Budget, Paperwork Reduction Project (0704-0188), Washington, DC 20503.

1. AGENCY USE ONLY (Leave blank)	2. REPORT DATE 10 Sep 95	3. REPORT TYPE AND DATES COVERED

4. TITLE AND SUBTITLE
Modeling of Ground Magnetic Signatures Associated With High Latitude Ionospheric Current Systems

5. FUNDING NUMBERS

6. AUTHOR(S)
Paul Gerald Gifford

7. PERFORMING ORGANIZATION NAME(S) AND ADDRESS(ES)
AFIT Students Attending:

Utah State University

DTIC SELECTED OCT 1 9 1995

8. PERFORMING ORGANIZATION REPORT NUMBER

95-110

9. SPONSORING/MONITORING AGENCY NAME(S) AND ADDRESS(ES)
DEPARTMENT OF THE AIR FORCE
AFIT/CI
2950 P STREET, BLDG 125
WRIGHT-PATTERSON AFB OH 45433-7765

10. SPONSORING/MONITORING AGENCY REPORT NUMBER

11. SUPPLEMENTARY NOTES

12a. DISTRIBUTION/AVAILABILITY STATEMENT
Approved for Public Release IAW AFR 190-1
Distribution Unlimited
BRIAN D. GAUTHIER, MSgt, USAF
Chief of Administration

12b. DISTRIBUTION CODE

Accesion For	
NTIS CRA&I	☒
DTIC TAB	☐
Unannounced	☐
Justification	

By	
Distribution /	

Availability Codes	
Dist	Avail and / or Special
A-1	

13. ABSTRACT (Maximum 200 words)

19951017 166

DTIC QUALITY INSPECTED 8

14. SUBJECT TERMS

15. NUMBER OF PAGES
126

16. PRICE CODE

17. SECURITY CLASSIFICATION OF REPORT	18. SECURITY CLASSIFICATION OF THIS PAGE	19. SECURITY CLASSIFICATION OF ABSTRACT	20. LIMITATION OF ABSTRACT

MODELING OF GROUND MAGNETIC SIGNATURES ASSOCIATED WITH

HIGH LATITUDE IONOSPHERIC CURRENT SYSTEMS

by

Paul Gerald Gifford

A thesis submitted in partial fulfillment
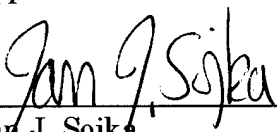of the requirements for the degree

of

MASTER OF SCIENCE
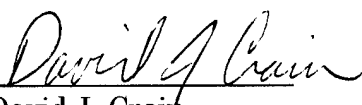
in
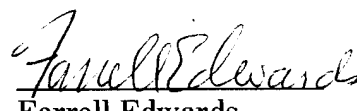
Physics
(Upper Atmospheric Physics)
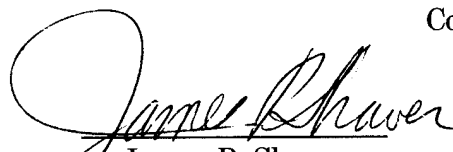
Approved:

_____
Jan J. Sojka
Major Professor

_____
David J. Crain
Committee Member

_____
Lie Zhu
Committee Member

_____
Farrell Edwards
Committee Member

_____
James P. Shaver
Dean of Graduate Studies

UTAH STATE UNIVERSITY
Logan, Utah

1995

ABSTRACT

Modeling of Ground Magnetic Signatures Associated with

High Latitude Ionospheric Current Systems

by

Paul G. Gifford, Master of Science

Utah State University, 1995

Major Professor: Dr. Jan J. Sojka
Department: Physics

Due to their location, ionospheric currents are difficult to study directly.
To gather information indirectly, magnetometers have been placed throughout
the polar regions to measure perturbations in the geomagnetic field caused by
the currents. The placement of these magnetometers has not been a
coordinated effort, with the result that coverage is far from uniform and large
gaps in the coverage exist. Understanding the abilities and limitations of the
magnetometer networks to resolve details about changes in the magnetic field
provides insight into the accuracy of the data. Discovering these abilities and
limitations is the focus of this research.

For use with ionospheric current system models, a simulation was made
of a ground magnetometer. After validation of this simulation, it was used to
verify Fukushima's theory on the cancellation of the ground magnetic

signatures caused by the field-aligned currents and Pedersen current. A distribution of the simulated magnetometers, patterned after the Scandinavian Magnetometer Array, proved successful in gathering information about traveling convection twin vortices. A global distribution of the magnetometers was tested with an ionospheric substorm model to find out what effects gaps in magnetometer coverage would have on the accuracy of data collected. It was found existing magnetometer networks do a reasonable job in returning accurate data, and the addition of more magnetometers to provide more uniform coverage did little to enhance the network's abilities.

(142 pages)

To my wonderful mother, Virginia Gifford,

who has always given me all her love and support.

ACKNOWLEDGMENTS

I would like to thank the Air Force Institute of Technology for allowing me to continue my education at their expense. I would also like to acknowledge the contribution of the 3M Company. If it weren't for Scotch Removable Magic Tape, I would likely still be cutting and pasting.

It is the people I've met here at Utah State University who made this a positive experience. My major professor, Dr. Jan Sojka, provided guidance, motivation, knowledge, and friendship. His continuous enthusiasm kept me believing that if I did "just this one last thing," I'd be done. All those "last things" are the reason this research is as complete as it is. Dr. Lie Zhu was an invaluable source of information, references, and data. He was always willing to drop everything to discuss my work, and he helped me get over several significant roadblocks in my work. Dr. Don Thompson's programming expertise, sense of humor, and plotting software kept me always moving in the right direction.

I am gratefully indebted to my mother, Virginia Gifford. She has always been my greatest fan, and raised me to believe in myself. Without that belief I would not have made it this far.

I would be quite insane if it weren't for the companionship of Maggie and Katie, the two best friends a man could have.

Finally, I have been truly blessed with the love and support of my beautiful wife, Louise. She has given my life new meaning, and has been my light at the end of the tunnel.

Paul Herald Kfford

CONTENTS

LIST OF TABLES

LIST OF FIGURES

CHAPTER I

INTRODUCTION

Currents flowing in the ionosphere, because of the ionosphere's inconvenient location, are difficult to study directly. Other methods must be devised to gather information about these ionospheric currents. Satellites can be used, as can sounding rockets. However, neither of these devices is as cost-effective as using ground-based magnetometers.

The first observation of the Earth's magnetic field was probably around 83 A.D., when Chinese "geomancers" noticed that a spoon made from lodestone spun on a smooth surface will come to rest pointing in the same direction every time. It was also the Chinese who developed the first compass, in the 11th century. Along with the discovery of the compass came the discovery of declination, the deflection of a compass needle to the east due to the difference between geomagnetic north and geographic north [Needham, 1962]. The earliest magnetic observatory was run by Sir Nicholas Millet, who recorded the declination at the same location from 1652 to 1670. Continuous recording was not possible until the development in 1847 of photographic recording. Since that time, the number of observatories has grown, reaching about 200 during the International Geophysical Year of 1957-58 [Jacobs, 1987]. Currently the number of magnetometers is about 150-200 in the northern hemisphere.

These ground-based magnetometers provide a glimpse into the workings of the ionosphere by observing perturbations in the geomagnetic field caused currents flowing in the ionosphere. By measuring these variations in the field, researchers can work backwards to reconstruct the conditions that could have caused the variations. While 200 magnetic observing stations may seem to be a large number, when considering the area and topography to be covered there are many gaps. Obviously, an incomplete data set will provide an incomplete picture of the ground magnetic signature and hence the currents flowing in the ionosphere. The question is: how much data is needed for an accurate reconstruction? The purpose of this study is to determine if the existing magnetometer distribution is adequate, and if not, what gains can be made by adding more magnetometers.

The study begins in Chapter II with an examination of the theory used to calculate the magnetic field from a current. Several simple cases are studied to gain a basic understanding of the effects of varying conditions on the magnetic field. Chapter III uses the model of a ground magnetometer to test Fukushima's theory on the cancellation of different types of ionospheric currents. In Chapter IV a small, short-lived current system, traveling convection twin vortices, is used to examine the capabilities of ground magnetometer networks in detecting small-scale events. A model of the

ionospheric current system is used to drive the magnetometer simulation, and the magnetic field pattern constructed from magnetometer data is compared to the known magnetic field pattern generated from a high density array of magnetometers that provides uniform coverage of the simulation domain. Chapter V uses a similar method to that used in Chapter IV, except the current system being studied is a global ionospheric substorm. A global distribution of magnetometers is used in an attempt to reconstruct the known pattern as observed by a uniform, dense array of magnetometers covering the simulation domain. Conclusions and further areas for research are presented in Chapter VI.

CHAPTER II

THEORY OF CURRENT–INDUCED

MAGNETIC FIELD PERTURBATIONS

When studying the effects of ionospheric storms and substorms on the geomagnetic field, it is important first to understand the effects of a simplified version of ionospheric current systems. Simulating simple current systems allows the examination of the individual components comprising a more complex system, and can provide insight into the importance of the relative effects of these components on the geomagnetic field. This in turn will make it easier to understand results from more complex models, and help predict what to expect from ionospheric currents.

The strength and direction of the magnetic field created by a current can be found by the Biot-Savart Law:

$$d\vec{B} = \frac{\mu_0}{4\pi} \frac{I d\vec{l} \times \vec{r}}{\left|\vec{r}\right|^3} \tag{1}$$

where $\vec{B}$ is the magnetic field vector, μ_0 is the permeability constant, I is the current strength, $d\vec{l}$ is the direction of the current, and $\vec{r}$ is the vector from the current to the point of interest [*Reitz et al.*, 1993]. Since this study will deal with simulated ionospheric currents, a number of assumptions must be

made. The Biot-Savart law is derived from one of Maxwell's equations,

$$\vec{\nabla} \times \vec{B} = \mu_0 \left(\vec{J} + \varepsilon_0 \frac{\partial \vec{E}}{\partial t} \right) \tag{2}$$

where $\vec{J}$ is the current density, ε_0 is the permittivity constant, and $\vec{E}$ is the electric field. The Biot-Savart law is based on static conditions, and so ignores the second term on the right-hand side of the equation, the displacement current. While the ionosphere is not a static environment, the conduction current $\vec{J}$ is much larger than the displacement current for the ionospheric currents that will be studied here so the displacement current can be ignored [*Kelley*, 1989]. There are other assumptions made in the simulations that should be mentioned. These assumptions are made to reduce the number of factors that could potentially contribute to errors, and by simplifying the simulations the results are more easily interpreted. Currents induced in the Earth's surface by the changing magnetic field are ignored. The field-aligned currents are assumed to be perpendicular to the Earth's surface. A field-aligned current not perpendicular to the Earth's surface would induce a vertical magnetic field – in the simulations here the vertical magnetic field is always caused by the horizontal currents. Field-aligned currents are treated as Gaussian distributions of current, while in the real ionosphere and magnetosphere they will have more complex

distributions. The horizontal currents in the ionosphere are treated as flat sheets with no vertical extent. The real ionosphere has a vertical dimension, and the currents flowing in the ionosphere will vary in the vertical direction. This research is not dependent on the accuracy of the ionospheric model used, so these factors will not affect the results obtained.

When describing geomagnetism, the magnetic field is measured in a coordinate system oriented with respect to the geomagnetic field. This system has three components: H, D, and Z. The H component points towards magnetic north, the D component to magnetic east, and the Z component is orthogonal to both of them, pointing downward. The orientation of this coordinate system is therefore not constant, but is dependent on the location the magnetic field is being measured at. The interrelationship of the three components is shown in Figure 1.
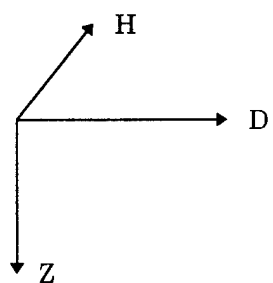
Figure 1: Spatial relationship of the H, D, and Z components.

Equation 1 is the basis of several computer models used to run a number of tests to determine the effect of various current configurations on the magnetic field at the ground. It is important to note that throughout all of the tests and simulations run in support of this thesis, the ionosphere was placed parallel to the H-D plane, 100 km above the ground. The field-aligned currents were perpendicular to the ionosphere and hence the ground. For the initial tests, three types of current systems were used: a line current, a line current with vertical currents at the end, and a current sheet, which was made up of many parallel line currents. The line currents represented currents in the ionosphere, with the vertical currents acting as field-aligned currents. The variables changed were the length of the line current, the height above the ground of the current system, the angle of the current relative to the coordinate system, and the number of wires and spacing in the current sheet. The output from the tests were either individual graphs of the H, D, and Z components versus distance from the current, or a ratio of the B-field strength to a baseline field strength versus a changing parameter. An example of the latter would be varying the length of the current from 1 km to 2,000 km, and comparing the field strengths calculated at each length to the field strength of a 2,000-km long current.

In the first test, the current was oriented to be parallel to the H-axis with the current flowing north, running through the origin of the coordinate

system. The magnetic signature on the ground was recorded along the D-axis, centered on the origin, for a distance of 500 km to the east and west of the origin. The program calculates the B-field by summing the contributions from each point along the current over its length for each point on the ground. Steps of 1 km were used on the current and on the ground. In the first run an "infinitely" long current was used – one where its length was much greater than its altitude. For this test, a 10,000-A current, 2,000 km long, was used. The results from this run are shown in Figure 2.

To verify that the magnitude of the result was correct, Ampère's Law was applied at the origin. Ampère's Law, for the case of a line current above a point, states:

$$B=\frac{\mu_0 I}{2\pi r} \qquad (3)$$

where B is the magnetic field strength, μ_0 is the permeability constant, I is the current strength, and r is the distance from the current to the point of interest. According to Ampère's Law, a current of 10,000 A at a distance of -100 km, the magnetic field strength is -20 nT, very close to the -19.9 nT obtained by the computer program discretely integrating the Biot-Savart Law. Note that the above calculation was done in Cartesian coordinates, so
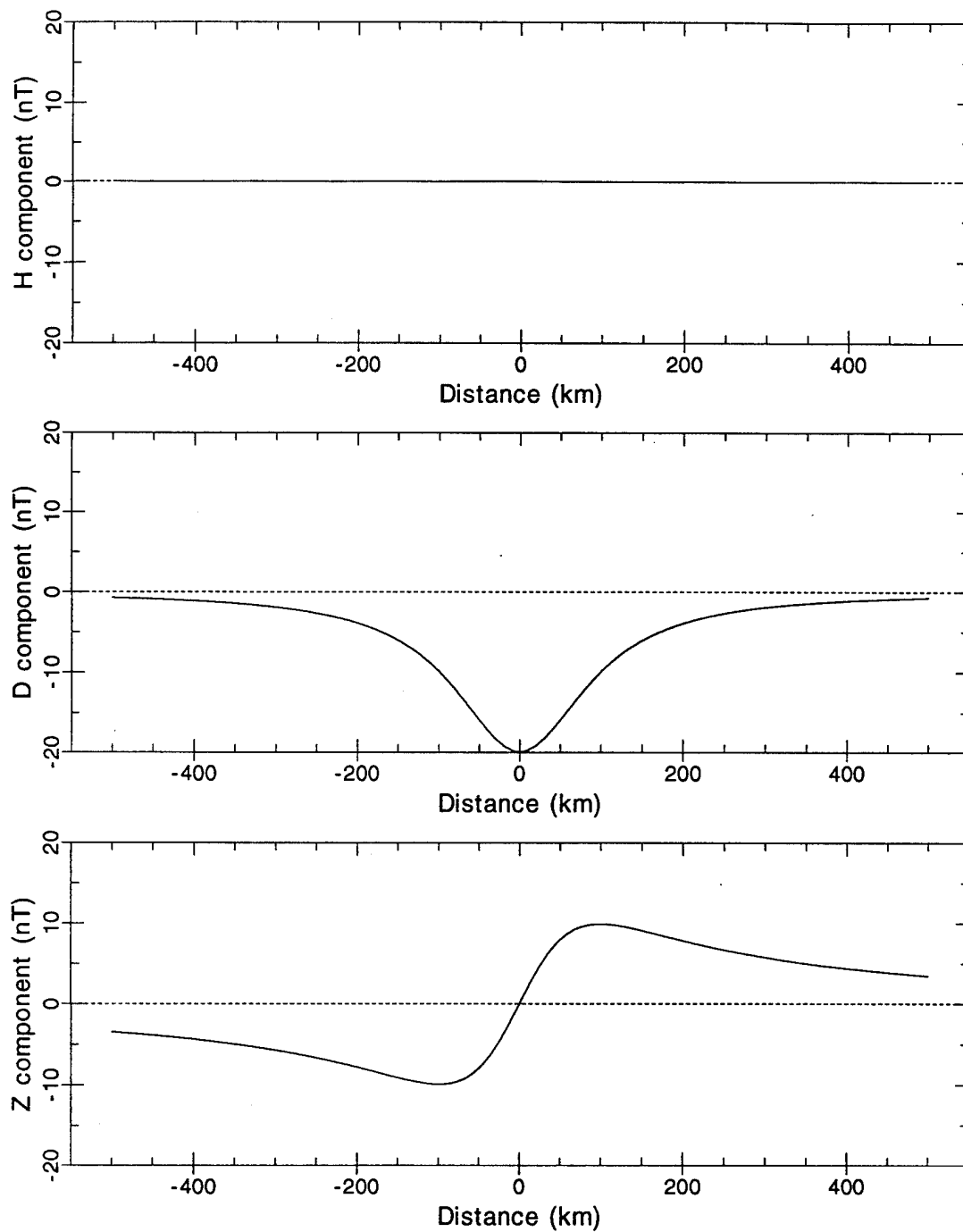
Figure 2: H (top), D (middle), and Z (bottom) components for a single wire running north-south carrying 10,000 A at an altitude of 100 km.

the distance from the current to the ground is negative. The current strength
and height above the ground are the key variables for this run, but the
length of the wire also has some importance. To determine what role the
length of the current plays, the magnetic field was calculated using shorter
lengths of wire. A 2000-km long current was used to generate the baseline
field strength, which is calculated at the origin. Field strengths from shorter
wires are then compared to the baseline. Figure 3 shows the effects of
decreasing wire length on magnetic field strength. As the length of the wire
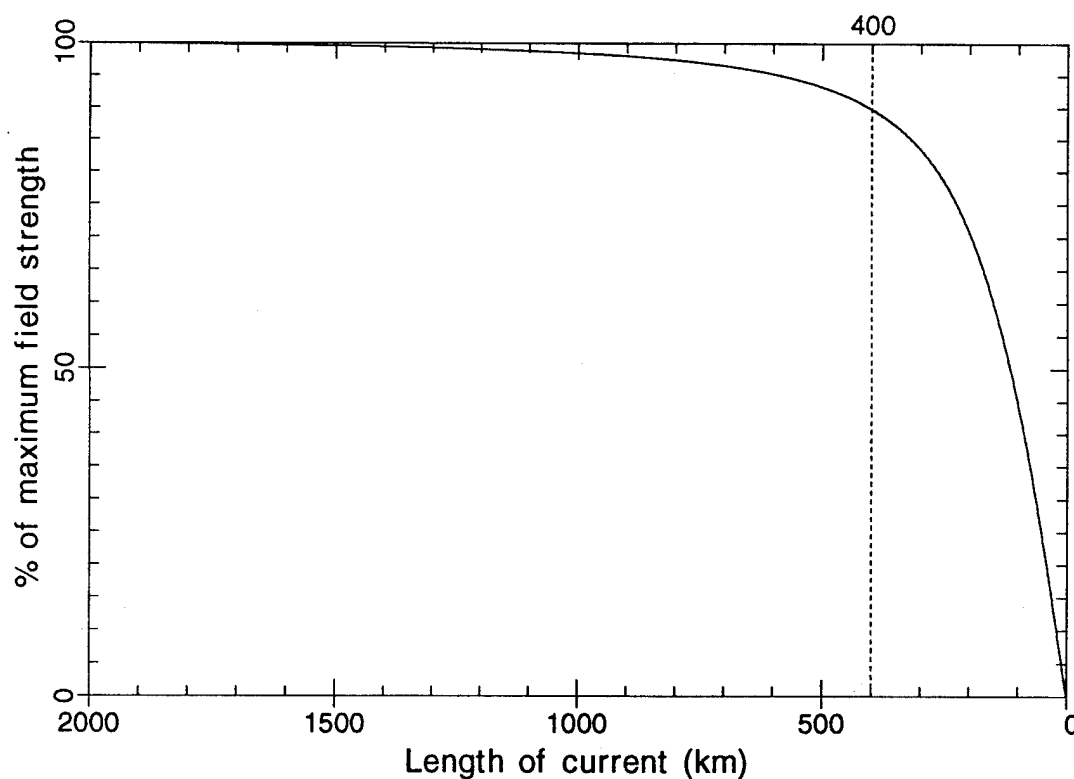
Figure 3: Diminishing magnetic field strength with decreasing current
length for a single wire. D component shown.

begins to decrease, the field strength slowly drops off, and at a length of 400 km the field strength has only decreased by 10%. As the current length becomes even less, the rate at which the field strength diminishes increases. On a global scale, 400 km is not very large, meaning horizontal currents have only a relatively local effect.

The next step was to rotate the current relative to the origin. The same current was used as in the first test, except that the current has been rotated 30° clockwise. The results are shown in Figure 4. As expected, the H and D components changed only by a factor of sine and cosine of the rotation angle, while the Z component remained unchanged.

Treating an atmospheric current as a thin wire served two purposes: to test the algorithms used to calculate the magnetic field, and to give a rough idea of the magnitudes expected in the field strength. To add more realism, the thin wire was replaced by a collection of wires to simulate a current sheet. The total current being carried (10,000 A) remained the same, except it was evenly distributed over a number of parallel, evenly-spaced wires. Figure 5 shows the magnetic signature along the D-axis due to 100 wires spaced 3 km apart. The resultant magnetic field is similar that of Figure 2. There is a slight decrease in the strength of the D and Z components, and the shape of the curve has been widened. Figure 6 shows the decrease in relative D component strength at the origin as the number of
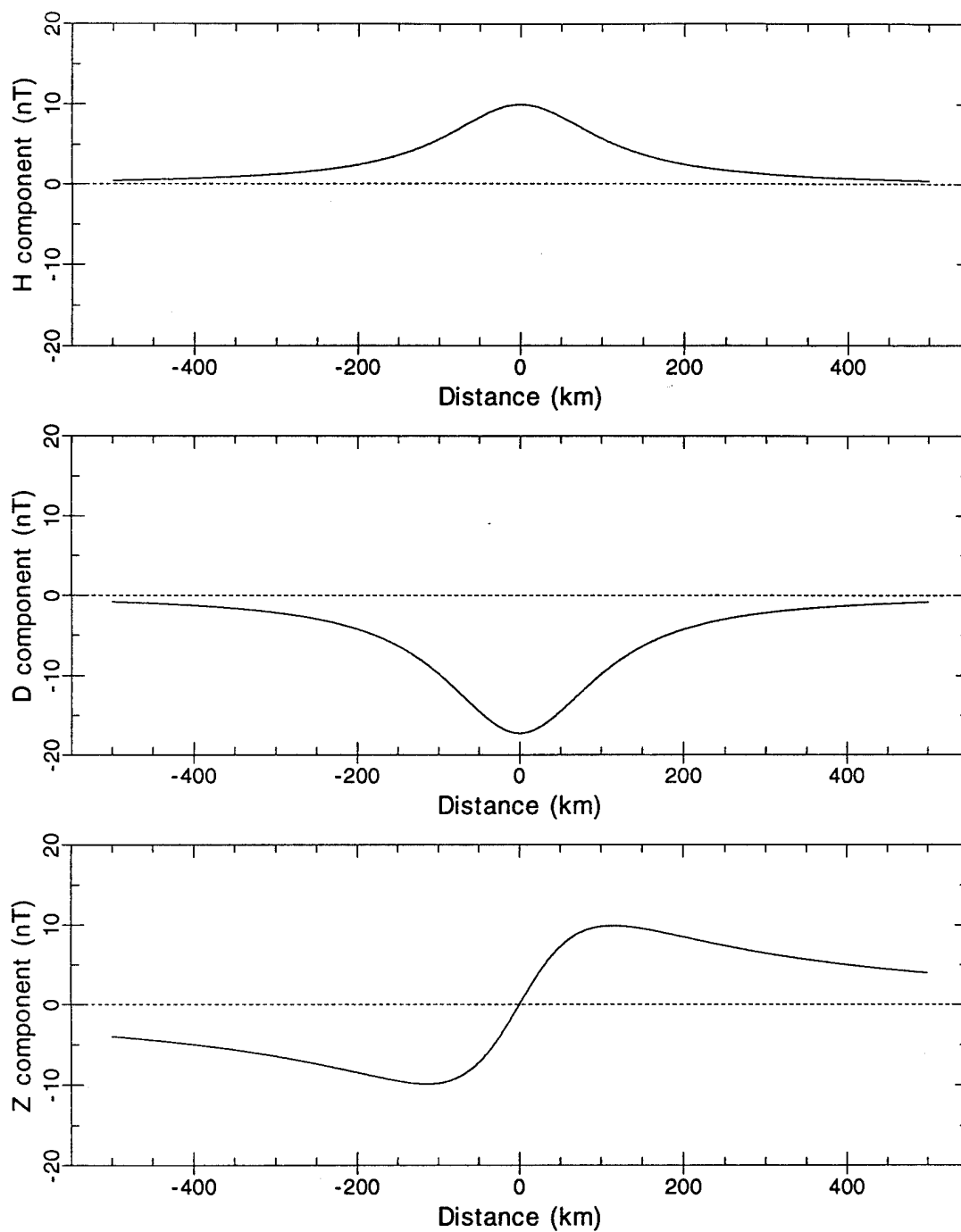
Figure 4: H (top), D (middle), and Z (bottom) components of the current system used for Figure 2 rotated 30° clockwise.
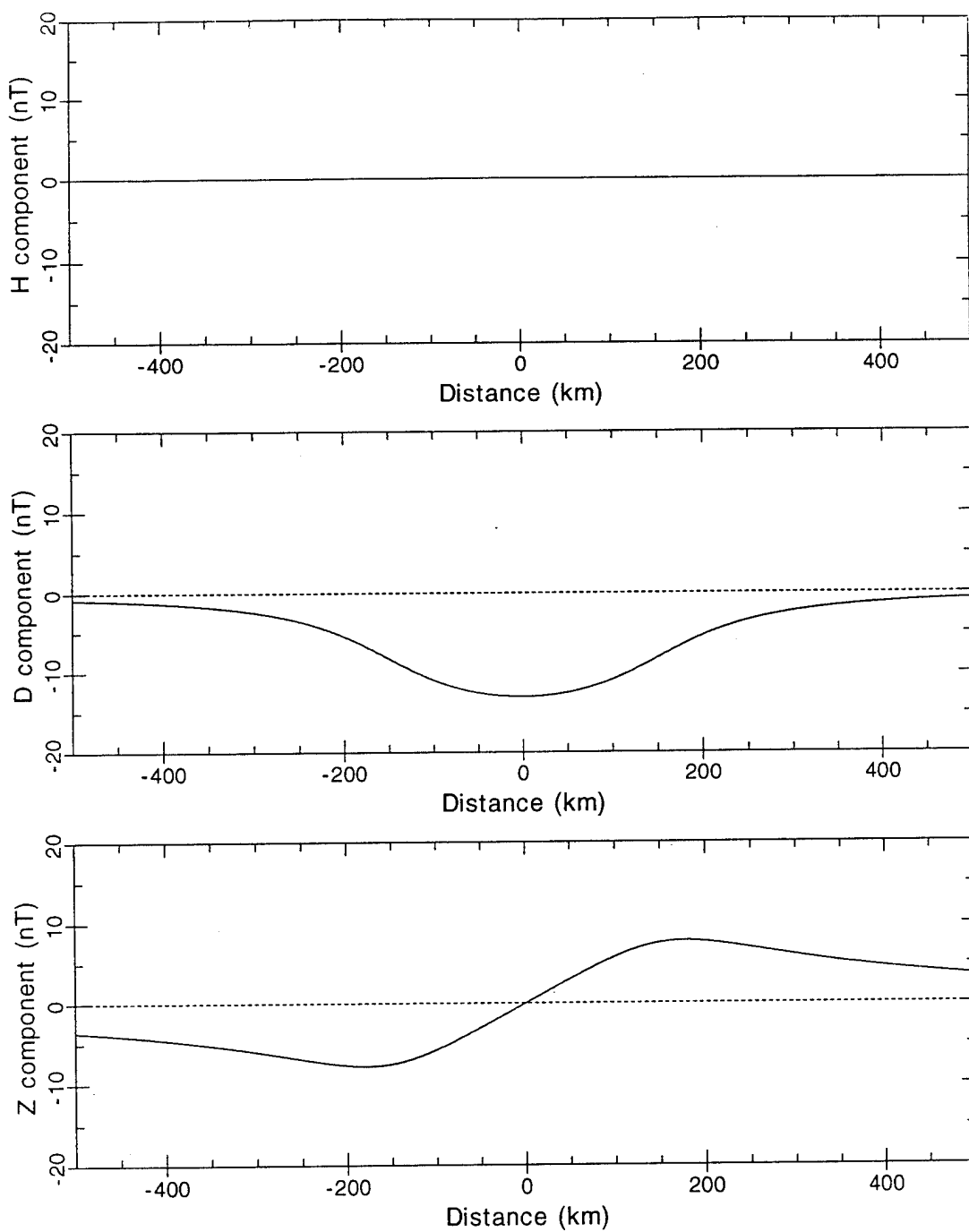
Figure 5: H (top), D (middle), and Z (bottom) components for a current sheet made up of 100 individual wires spaced 3 km apart.

wires is increased, at 1-km intervals. Only the D component is shown because the Z component cancels out at the origin. The current sheet is made up of wires evenly spaced around the origin, so the vertical magnetic field created by a wire some distance to the east of the origin will be canceled by the field created by a wire an equal distance to the west of the origin. The field strength decreases rather slowly, reaching 50% of its maximum value when there are about 460 wires, or a sheet extending 230 km to either side of the origin. From Figure 3 above, at a distance of 230 km the field strength is
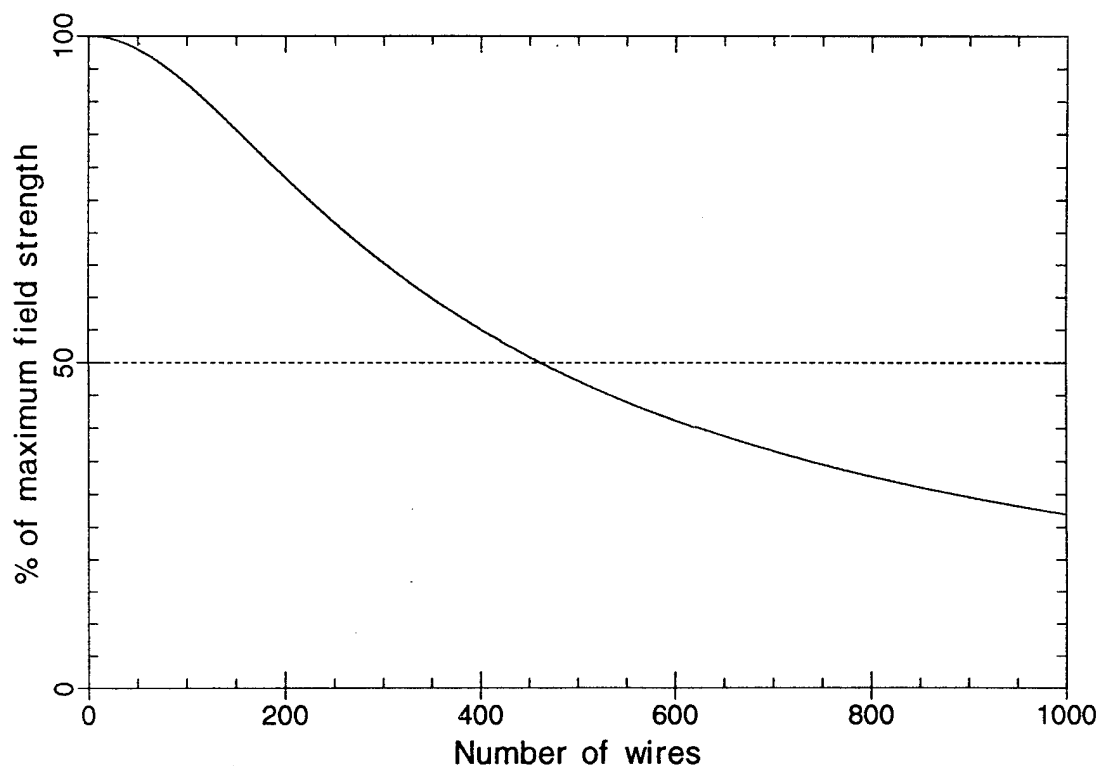
Figure 6: Diminishing magnetic field strength with increasingly wide current sheet. D component shown.

about 20% of maximum (for the same current and altitude). Therefore, as the current sheet broadens, the diminishing magnetic field strength is due to the weakening of currents near the point of interest rather than the decreasing effect of currents at farther distances.

Up to this point, all the currents examined have been parallel to the ground. To create a more realistic scenario, vertical currents were added to the horizontal current used to generate Figure 2. As described above, these currents are parallel to the Z-axis and act as field-aligned currents, providing a source and an outlet for the horizontal current. The magnetic field from this configuration is shown in Figure 7. Vertical currents do not contribute to the vertical magnetic field, and since they are parallel to the H-axis, the H component cancels out along the D-axis. For this case, then, only the D component has been affected. The net effect of vertical currents is the creation of a magnetic field that opposes the magnetic field created by the horizontal current between them, as can be seen when comparing Figure 7 to Figure 2. In other words, the vertical currents can make it more difficult to detect some horizontal currents.

The creation of a magnetic field is a local effect, on the global scale. This is as expected from the Biot-Savart law, which is an inverse square law. The relative strength of the magnetic field caused by a current diminishes rapidly with distance, when compared to a current overhead. It might
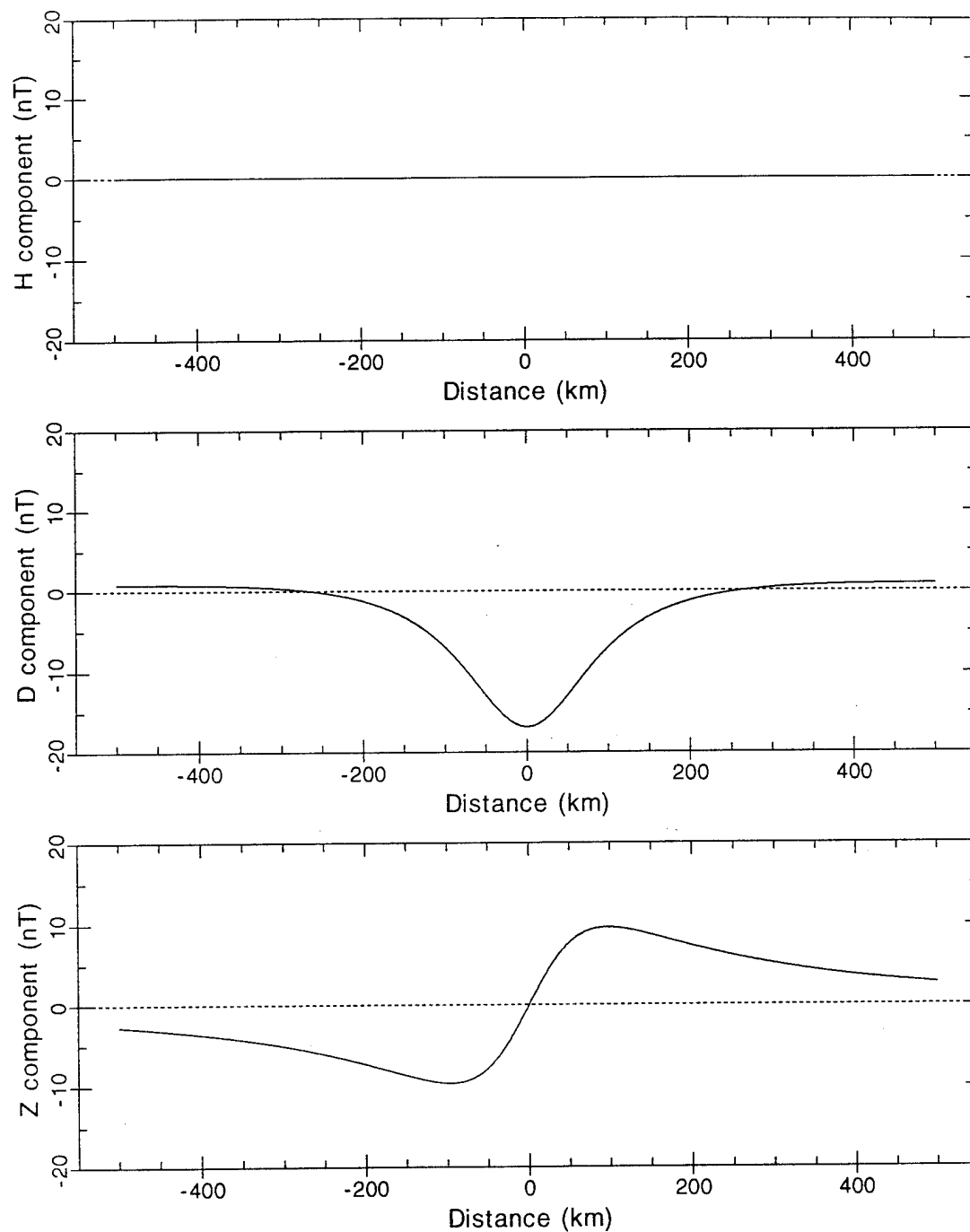
Figure 7: H (top), D (middle), and Z (bottom) components of a north-south oriented wire with opposite-oriented currents at each end.

appear that a dense magnetometer network would be needed to accurately map the magnetic field from ionospheric currents. However, with larger currents a larger magnetic field is created, and a small percentage of a large number can still be significant. Subsequent chapters will examine just how dense magnetometer networks must be to map both local and global ionospheric current systems.

CHAPTER III

TESTS OF FUKUSHIMA'S THEORY

The ionospheric models used to drive the ground magnetometer simulation can provide the ionospheric currents broken down into their component currents, i.e., field-aligned, Hall, and Pedersen currents. In these models, the field-aligned current runs parallel to the Z-axis, the Pederson current is perpendicular to the Z-axis and parallel to the electric field created by the field-aligned currents, and the Hall current is perpendicular to both the Z-axis and the electric field [*Tascione*, 1988]. Having the ionospheric currents broken down into their component parts provided the opportunity to test a theory put forth by *Fukushima* [1969]. This theory states that for an ionosphere with uniform conductivity parallel to the ground and field-aligned currents parallel to the Z-axis, the field-aligned and Pedersen currents combined will produce no ground magnetic signature. The current system is illustrated in Figure 8, where (B) is the field-aligned and Pedersen currents combined. Current system (B) is made up of (B1) and (B2), and Fukushima argues that since neither (B1) nor (B2) produces a ground magnetic signature, (B) will not produce one either.

This theory was tested three ways. The first test used a current system modeled after (B1) in Figure 8. The second test used currents more
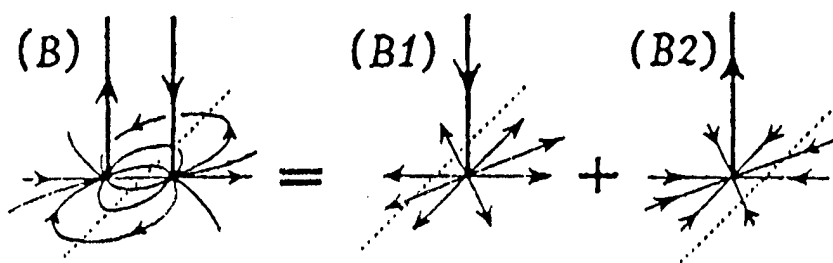
Figure 8: An illustration of field-aligned and Pedersen current (B), and its component parts (B1) and (B2) [*Fukushima*, 1969].

similar to that of (B) in Figure 8. Finally, the theory was tested using currents generated by more complex ionospheric models.

The first test calculated the ground magnetic signature of a single downward field-aligned current coupled to a plane of outward-flowing radial currents. There was no return current flow, and the current grid was 200-points by 200-points, with grid spacing of 20 km. The size of this grid was a compromise between the desire to achieve good results and keeping the program run time reasonable. Currents were treated as wires, with no physical dimensions other than length. The field-aligned current carried 100,000 A, which connected to 360 radial wires 100 grid points long at an altitude of 100 km. The magnetic fields produced by the field-aligned and horizontal currents individually are shown in Figures 9-12, and the total magnetic field is shown in Figures 13-15. Since the magnetic field produced

by the field-aligned current has no Z component, this means the Z component produced by the horizontal current must be self-canceling. Figure 15 shows the Z component from the horizontal currents is about 97% canceled. The oddly symmetrical pattern in Figure 15 is because radial currents were overlaid on a Cartesian grid. Using polar coordinates would have eliminated the symmetry around the four axes and given a pattern with radial symmetry instead. The total H and D components, shown in Figures 13 and 14, are about 90% canceled. There are several factors inherent in the model that prevent the total cancellation of the magnetic field for this current system. Resolution is probably the leading cause of error. The grid spacing of 20 km is too large, especially near the origin where the radial currents begin. Only beginning at 44 grid points out from the origin are there enough grid points to prevent overlapping of neighboring wires onto a single grid point. Technically the model is actually depicting discrete points of current spaced 20 km apart along 360 radials. Smaller grid spacing would be closer to the concept of continuous wires. It is clear, though, that for at least this current system, Fukushima was correct in stating there would be no ground magnetic signature under ideal conditions.

For the second test, a simplified current distribution with two field-aligned currents was used, as in (B) of Figure 8. In this case, the currents were distributions rather than wire currents. The field-aligned currents
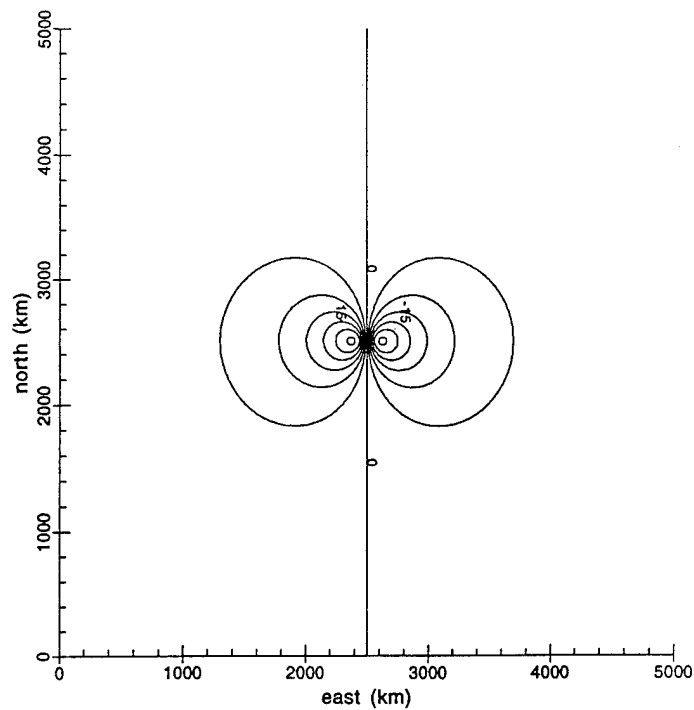
Figure 9: H component of the single wire field-aligned current.
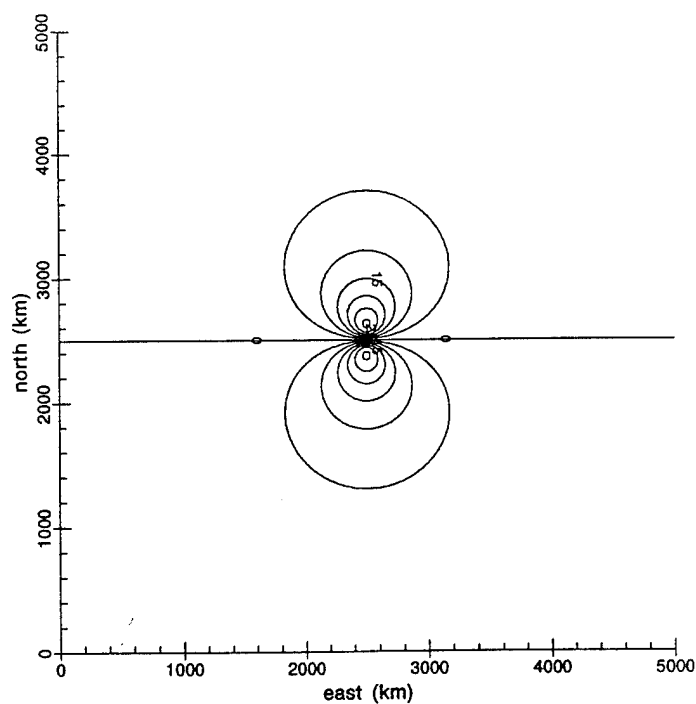
Figure 10: D component of the single wire field-aligned current.
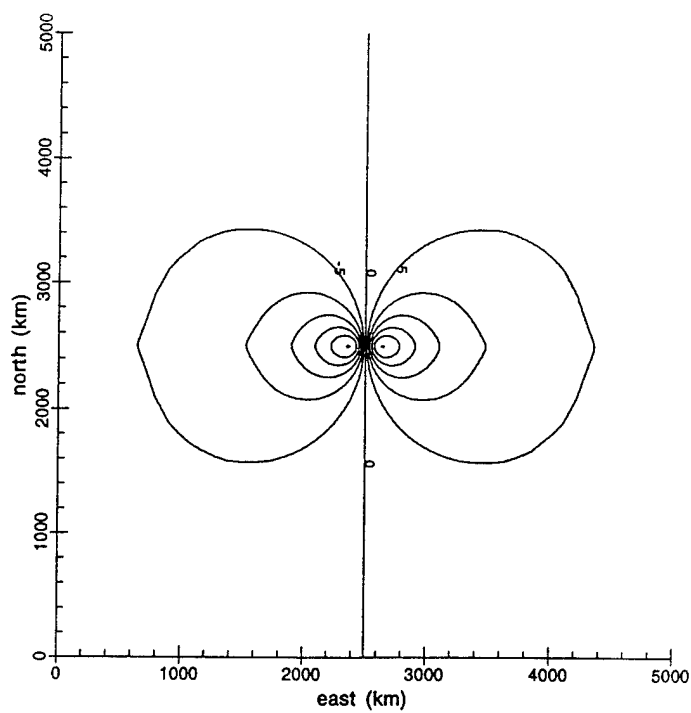
Figure 11: H component of the radial horizontal currents.
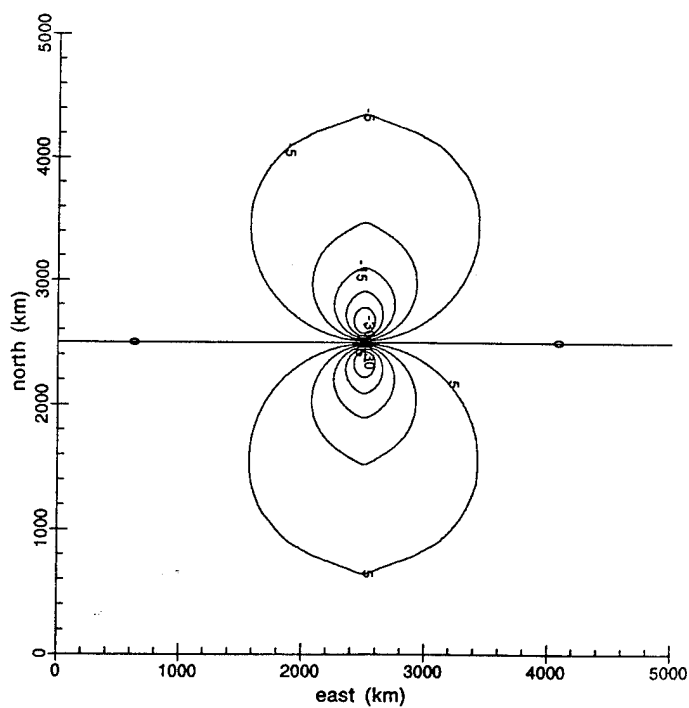
Figure 12: D component of the radial horizontal currents.

23
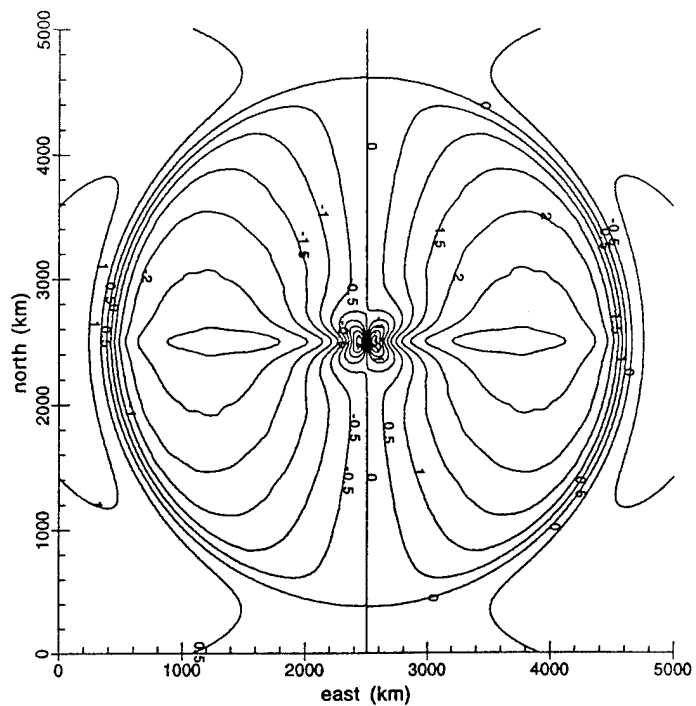
Figure 13: Total H component from field-aligned and horizontal currents combined.
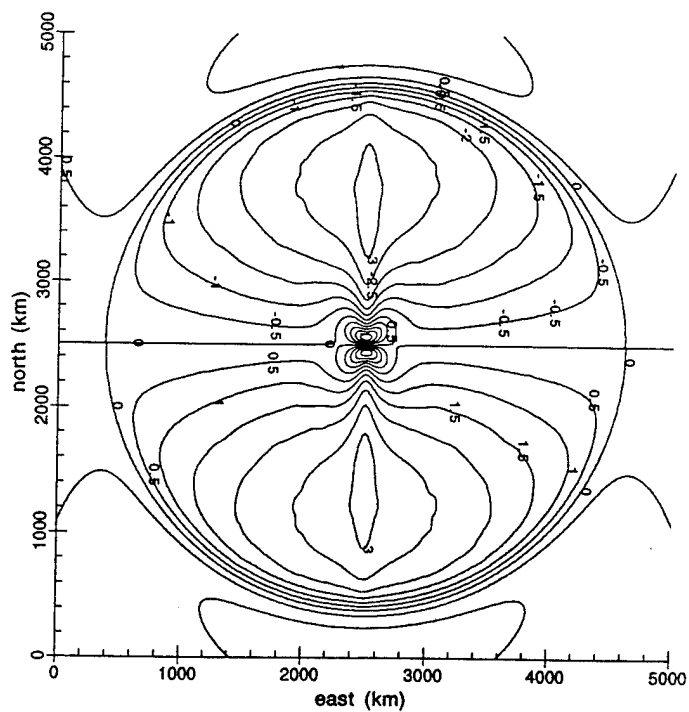
Figure 14: Total D component from field-aligned and horizontal currents combined.
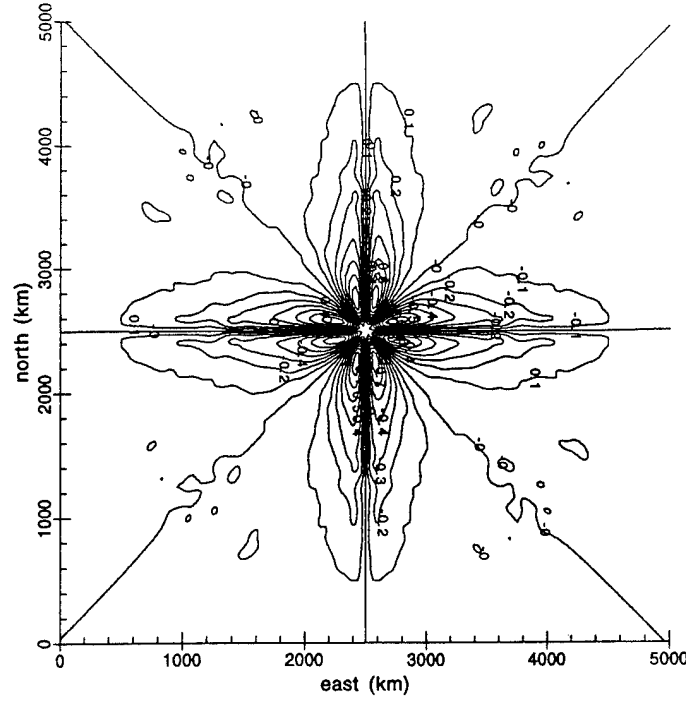
Figure 15: Total Z component. This is due to only the horizontal currents.

were generated using a Gaussian distribution. The electric potential of the modeled ionosphere was set to zero everywhere, and a boundary condition of zero electric potential was imposed along the entire boundary. With the field-aligned currents acting as a source, through conservation of charge,

$$\vec{J}_{\parallel} = \nabla \cdot \vec{J}_{hor} \tag{4}$$

where $\vec{J}_{\parallel}$ is the field-aligned current and $\vec{J}_{hor}$ is the horizontal current, the potential is calculated at each point on the grid iteratively. If the largest

change on the grid from one iteration to the next falls below a specified threshold, then the solution has converged and the potential has been determined. Once the potential is generated, the electric field is calculated from

$$\vec{E} = -\vec{\nabla}V \qquad (5)$$

where $\vec{E}$ is the electric field and V is the electric potential. The Pedersen current is then calculated from

$$\vec{I}_p = \Sigma_p \vec{E} \qquad (6)$$

where $\vec{I}_p$ is the Pedersen current, and Σ_p is the Pedersen conductivity. The D component of the magnetic field caused by these currents are shown in Figures 16-18. These figures show a 90-95% cancellation of the magnetic field. The imposed boundary condition described above could be a reason there was not complete cancellation, because the horizontal currents are forced to zero there. Also, using a finer grid mesh than the 20 km used might contribute to a greater cancellation of the magnetic field.

The third test used a simplified version of the ionospheric model
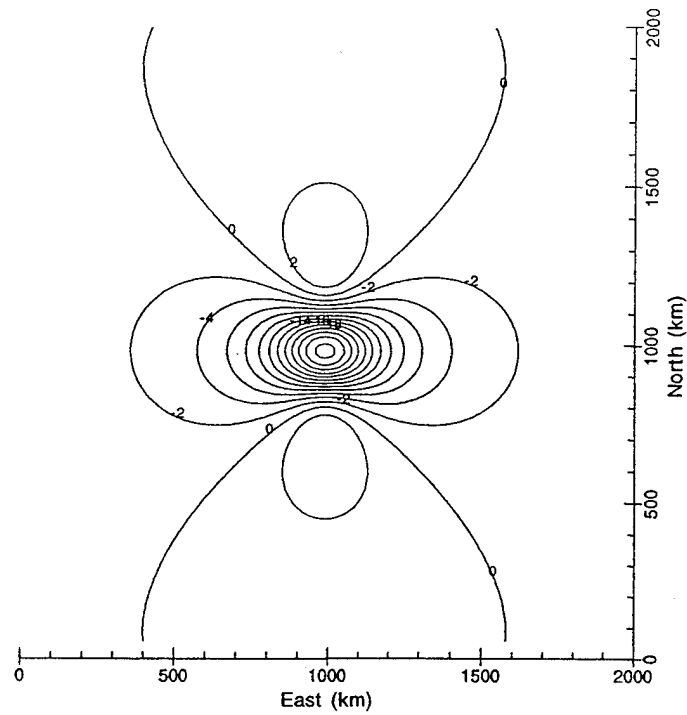
Figure 16: D component of the Pedersen current for a simple current distribution.
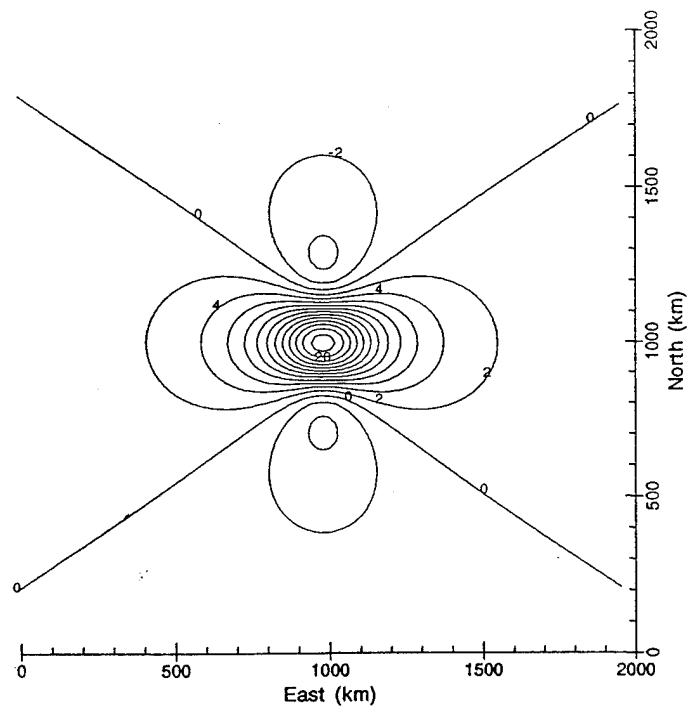
Figure 17: D component for two field-aligned currents of opposite polarity.
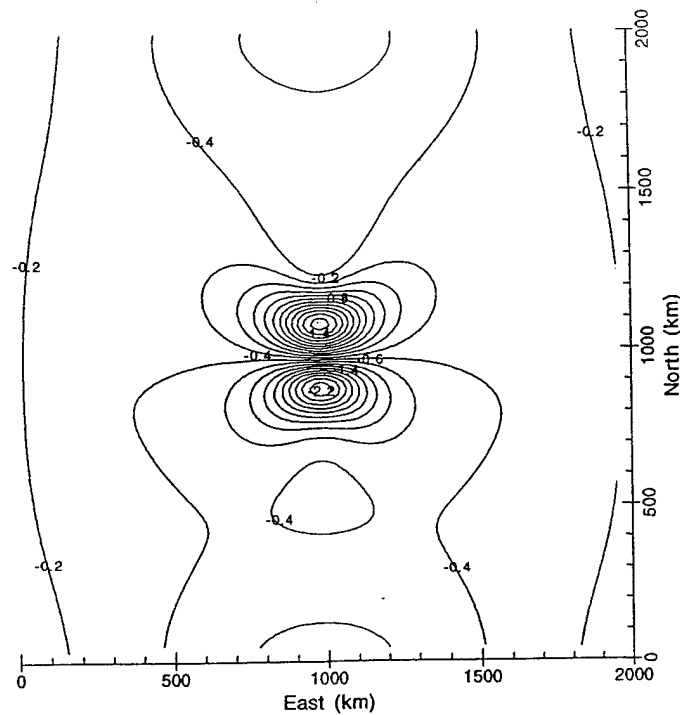
Figure 18: D component for the field-aligned and Pedersen currents combined.

created by *Schunk et al.* [1994]. This is a model of traveling twin convection vortices, and has been simplified by using uniform ionospheric conductivity. This model is described in greater detail in the next chapter. The simulation domain of this model encompasses approximately 30% of the area in the model from the second test, as the currents are calculated for a 55-by-55 point grid. The magnetic field was calculated over a 220-by-95 point grid. The large x-dimension is to allow the twin vortices room to travel; this is

taken advantage of in the next chapter. Output from this test is shown in Figures 19-25. This run was not as successful, with only 50% cancellation of the field-aligned and Pedersen currents. This large residue can be attributed to the much smaller simulation domain. The same boundary conditions were imposed on both the second and third test. The condition that the electric potential be zero at the boundary will have a greater effect on the third test, because it is causing a greater gradient in the potential, which leads to a greater gradient in the horizontal currents. The horizontal currents are, in effect, compressed. The field-aligned currents are not affected by this boundary condition. The net result is the third test has very similar field-aligned currents to the second test, but with very different horizontal currents.
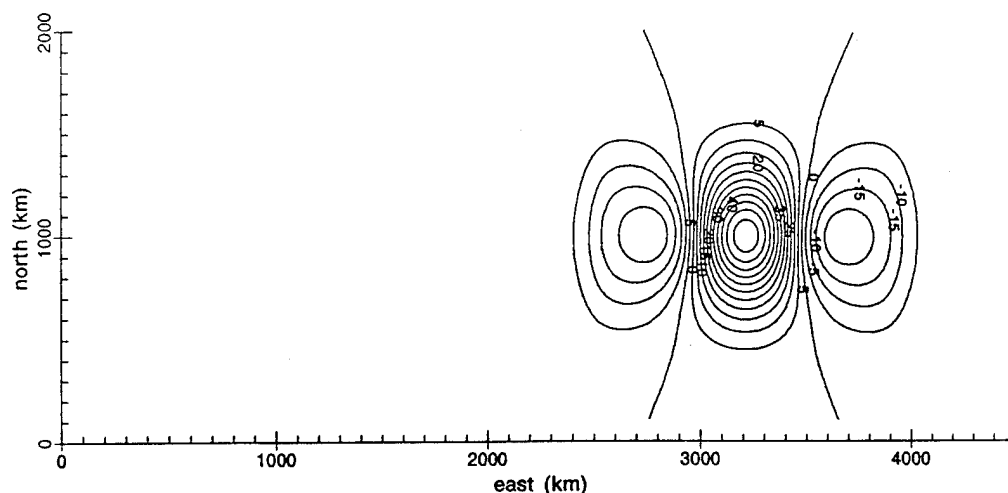
Figure 19: H component of Pedersen current from simplified twin vortices.
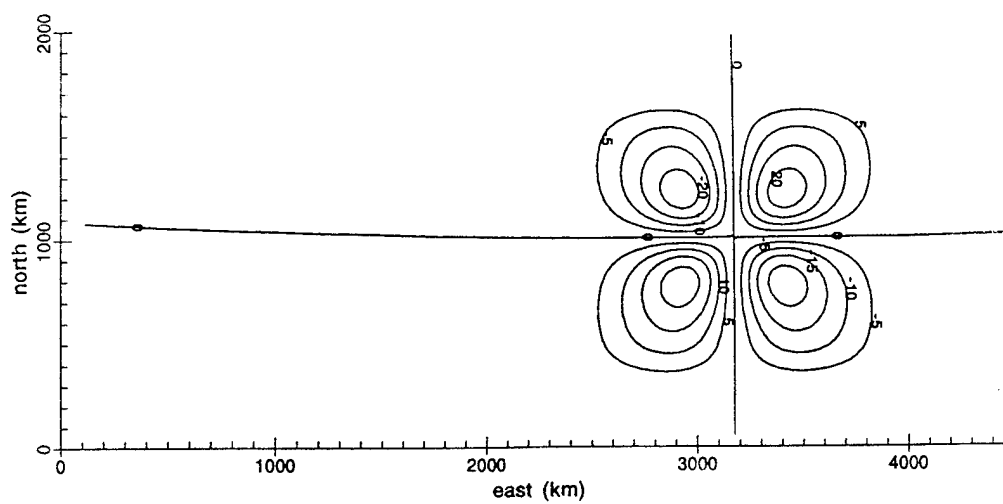
Figure 20: D component of Pedersen current from simplified twin vortices.
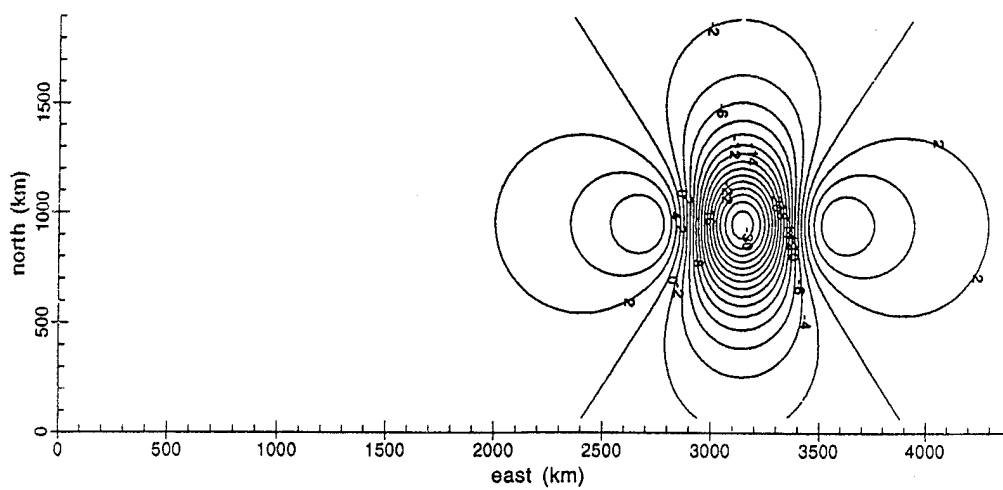
Figure 21: H component of field-aligned current from simplified twin vortices.
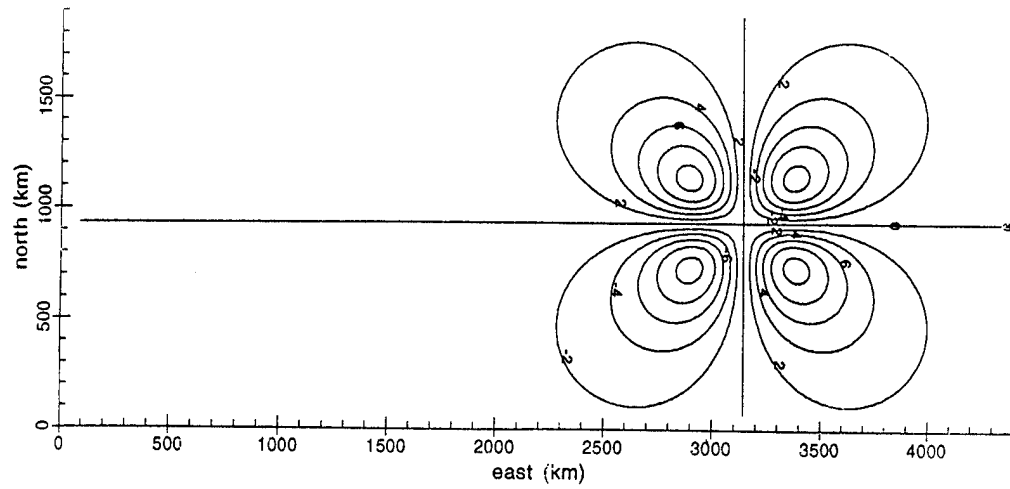
Figure 22: D component of field-aligned currents from simplified twin vortices.
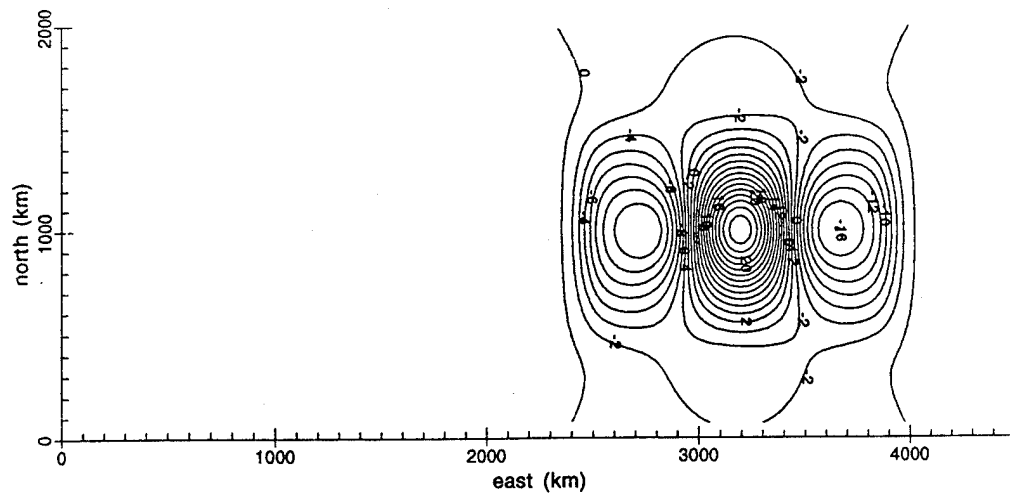
Figure 23: H component of combined field-aligned and Pedersen currents from simplified twin vortices.
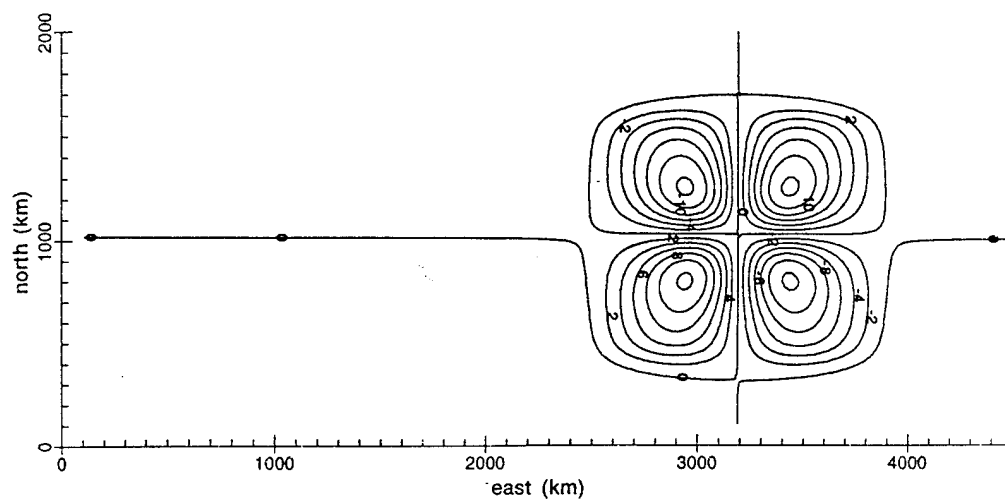
Figure 24: D component of combined field-aligned and Pedersen currents from simplified twin vortices.
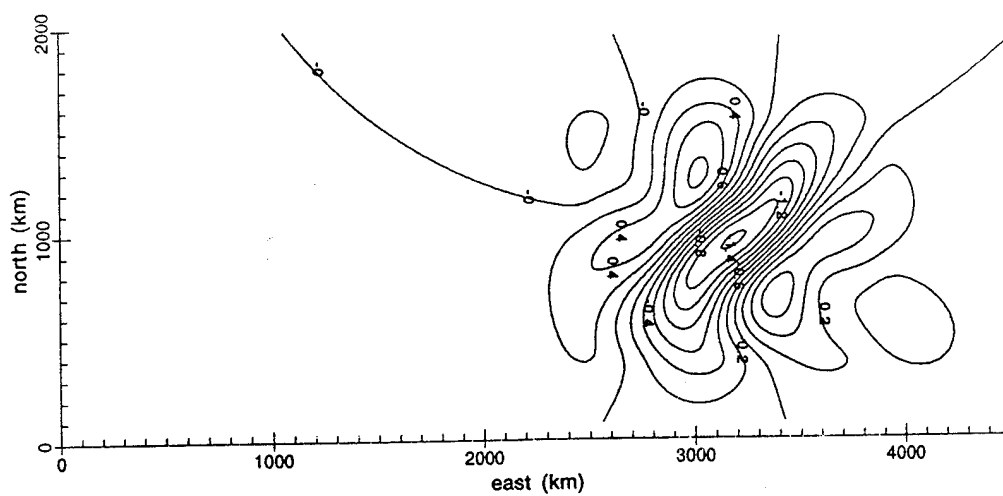
Figure 25: Z component of Pedersen current from simplified twin vortices. The field-aligned current makes no contribution to this component.

The tests run confirm Fukushima's theory. Errors encountered can be explained by deficiencies in the models. These models can be improved by increasing the size of the simulation domain and by decreasing the grid spacing in the grids. However, increasing the number of grid points causes a proportional increase in model run time, and these times can quickly become prohibitive. For example, changing the grid spacing in the third test to 5 km and doubling the dimensions of the grid would cause the model run to take over a week on a very fast workstation.

There are also other considerations. The theory is valid for an ionosphere parallel to the ground with perpendicular field-aligned currents, conditions that may not always be present in a real ionosphere. Also, artificial constraints placed on a simulated ionosphere can skew the results such that there is not a complete cancellation between the magnetic fields caused by the field-aligned and Pedersen currents. This theory does provide an excellent way for modelers to test their methods of modeling ionospheric currents. Adjustments to initial and boundary conditions can be made until the ground magnetic signature of the combined field-aligned and Pedersen currents approaches zero.

CHAPTER IV

A STUDY OF TRAVELING CONVECTION VORTICES

After validating the modeled ground magnetometer signatures and gaining some insight into the properties of perturbed magnetic fields, the next step was to use the simulated magnetometers to study small-scale events. The events chosen were traveling convection twin vortices. Twin vortices are convection cells embedded in a larger convection pattern, and have enhanced electric fields as well as opposite flowing field-aligned currents. The size of the vortex pattern can be up to 1000 km in the east-west direction, and 500 km in the north-south direction. The vortices move at 3-6 km/s towards the night side and last for 10-20 min [*Schunk et al.,* 1994]. The objective of studying traveling twin vortices was to determine how much detail ground-based magnetometer networks can provide. *Glassmeier et al.* [1989] used the Scandinavian Magnetometer Array in conjunction with satellite observations to study these events. *Glassmeier* [1992] goes into great detail discussing possible sources for twin vortices. A comprehensive study of a single event can be found in *Heikkila et al.* [1989].

Input into the simulated magnetometer network was provided by the *Zhu et al.* [1993] electrodynamic model. This model is similar to the model used for the third test in Chapter III. It provides field-aligned and horizontal

current distributions over a 181 (east-west)-by-55 (north-south) grid with 20 km spacing, although the currents are limited to a 55-by-55 grid within the larger grid. This model also adds decay over time of the field-aligned currents, as well as gradients in the ionospheric conductivity. These gradients are important to include because they occur in the actual ionosphere from two sources. One source of the gradient is solar radiation: The ionospheric conductivity is high in the dayside region, lower in the nightside region. The other source of the gradient is electron precipitation associated with the field-aligned currents. It was shown in the previous chapter that this model produces horizontal currents that are confined to a disproportionately small area when compared to the field-aligned currents. However, for the purposes of this chapter the model provides a sufficient representation of ionospheric currents.

Three variations of the vortices were used. In the first variation, the upward field-aligned current is at the leading edge of the motion, and will be used to examine the general features of the resultant ground magnetic field. The second variation has a leading downward field-aligned current. This will show whether or not it is possible to determine the polarity of the traveling vortices from the induced ground magnetic field. The third case is the same as the first, except that there is no decay of the field-aligned currents over time. In all cases the vortices are moving at 3 km/s. The

electrodynamic model was run for 1, 3, and 6 min after the vortices reached maximum intensity, to study the general features of each case. The model was also run at 10-s intervals for 41 intervals, again starting after the vortices reached maximum intensity. These data were used in conjunction with the simulated ground magnetometer network. Field-aligned and horizontal currents for the first case are shown in Figure 26. Rather than attempt to re-create the input current system from magnetometer data, the data were instead used to re-create the total ground magnetic signature. The magnetic field was calculated over a 221 (east-west)-by-95 (north-south) point grid with 20-km spacing, with the input current system centered on, but 100 km above, this grid. Figure 27 shows the relation between the grid on the ground and the grid used for the current system. If the simulated magnetometer networks could re-create the field with limited error, then data from the networks would be sufficient to re-create ionospheric currents. The 6 min runs will be used for the comparisons with the data from the simulated ground magnetometer network, because at this time the twin vortices were completely over the simulated ground network. Results from all three cases at 6 min are shown in Figures 28-30. The 1- and 3- min runs for case 1 are in Appendix A, for case 2 in Appendix B, and for case 3 in Appendix C.
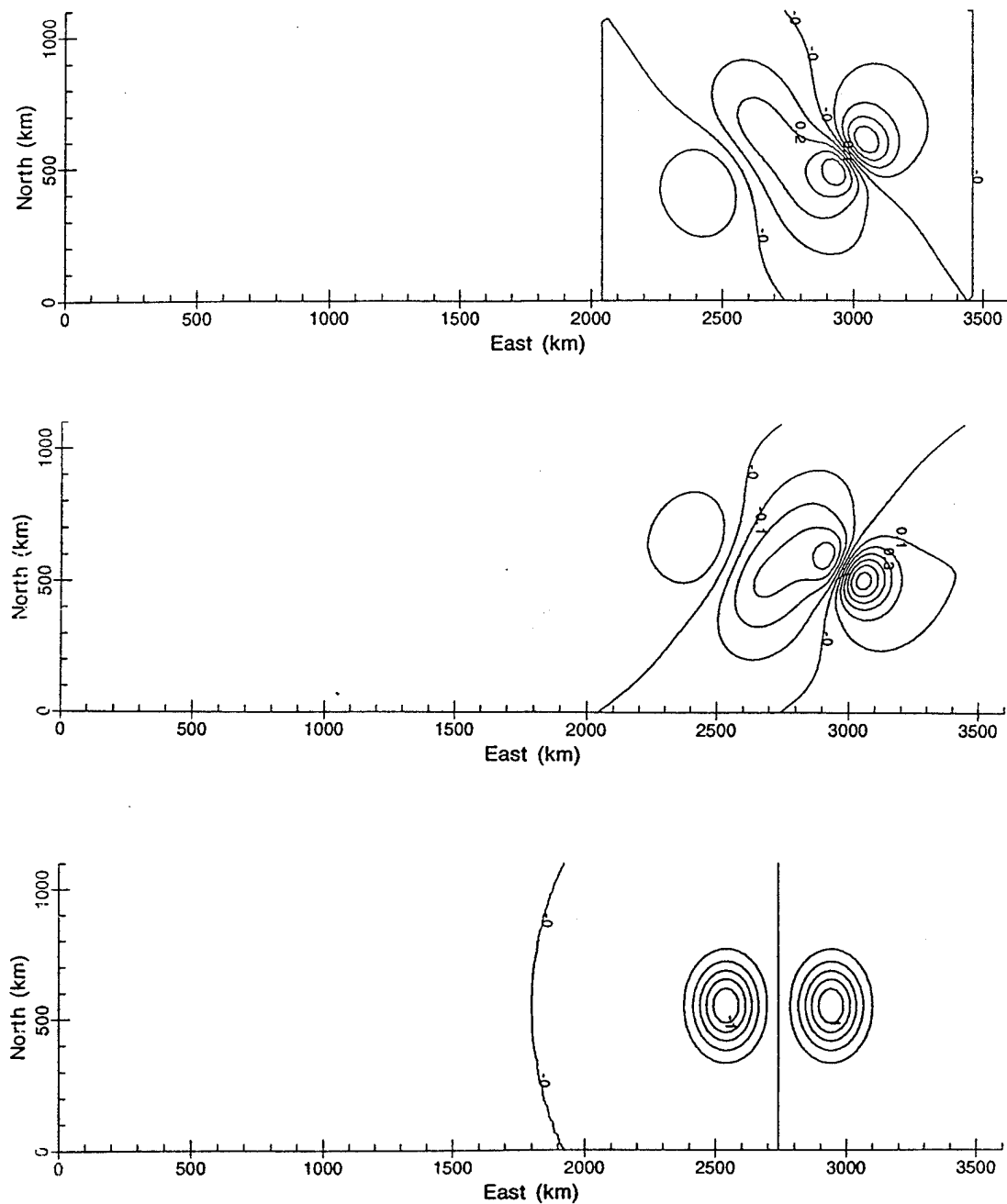
Figure 26: Field-aligned (top), east-west horizontal current (middle), and north-south horizontal current (bottom) from twin vortices model of case 1 at 1 min. Units for field-aligned current are μA/m², units for horizontal currents are A/m.
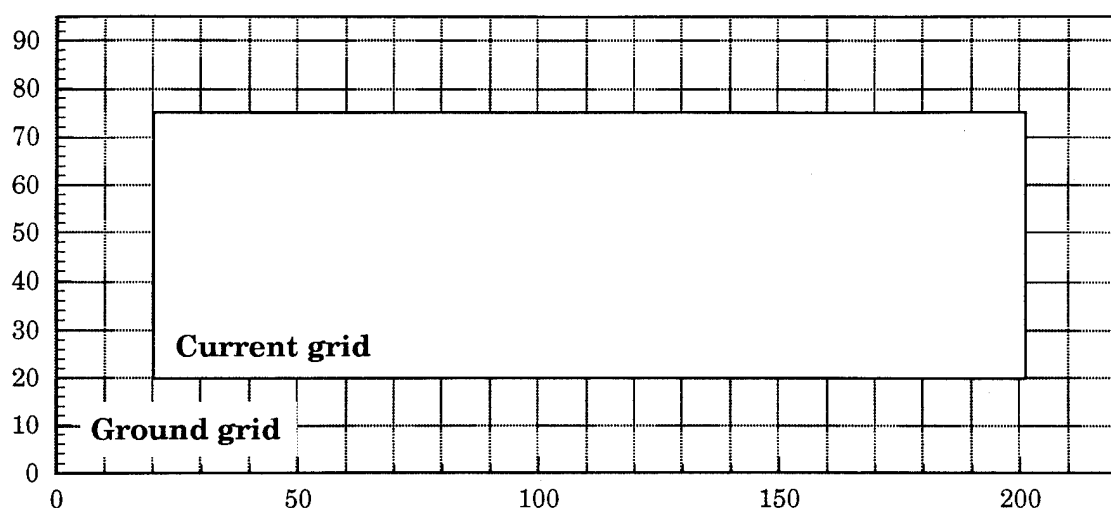
Figure 27: Comparison between grid used for ground magnetic field (large grid) and grid containing current data. The grid containing current data is located 100 km above the grid used for the ground magnetic field. 1 unit equals 20 km.

There are several features to look for in Figures 28-30 and Appendices A, B, and C. The polarity of the field-aligned current in case 2 is opposite that of case 1, which causes the polarities of the ground magnetic signatures to be opposite as well. The center cell in the H and D components of case 1 and case 2 becomes less intense with time. This is due to the decay of the field-aligned current. Case 3, in which the field-aligned current does not decay, has a nearly constant center cell.

It is important to note the distortion of the magnetic field. The magnetic field is not, as might be expected, perpendicular to the line connecting the vortices. *Friis-Christensen et al.* [1988], and *McHenry and*
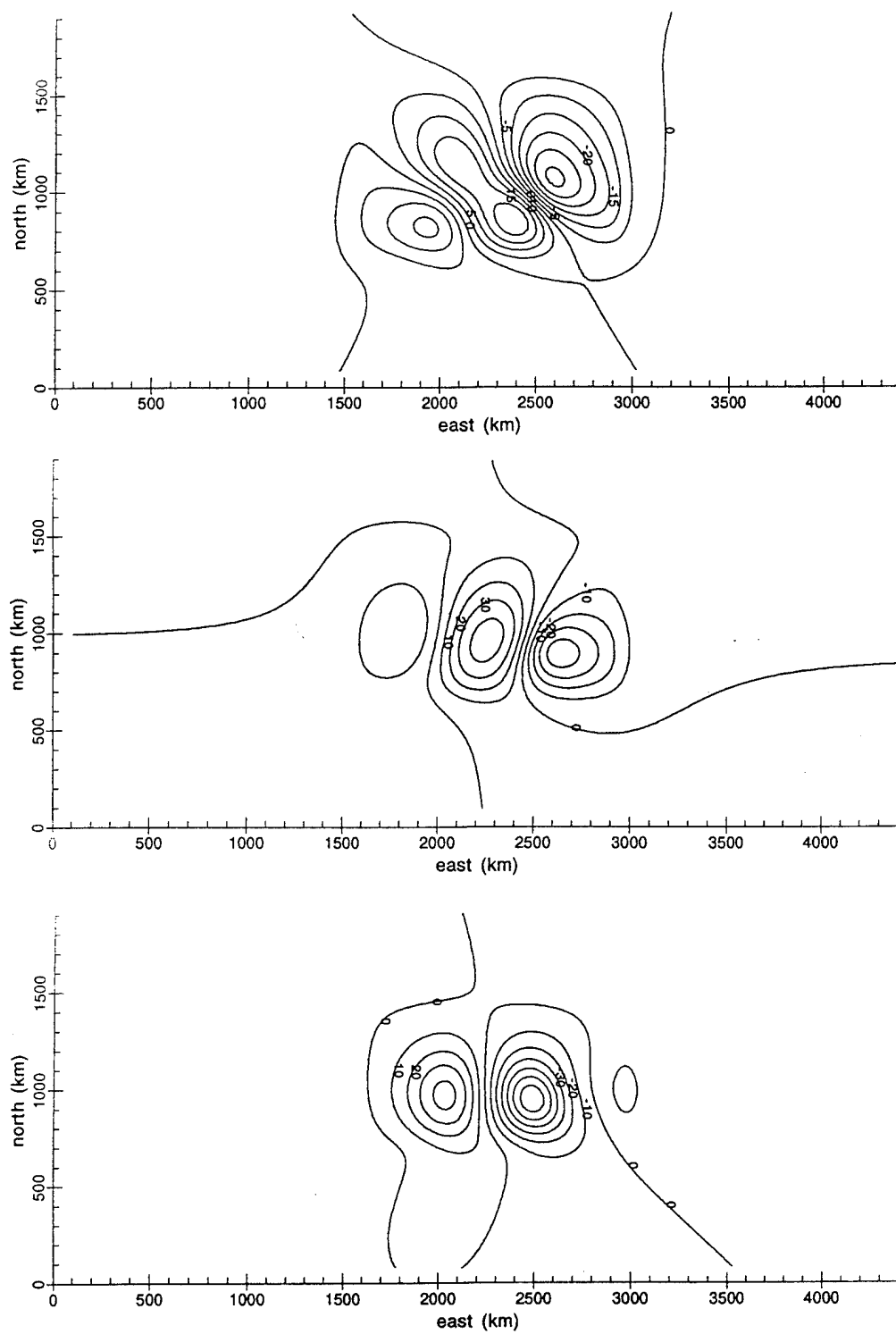
Figure 28: H (top), D (middle), and Z (bottom) components of case 1 at 6 min, in nT.
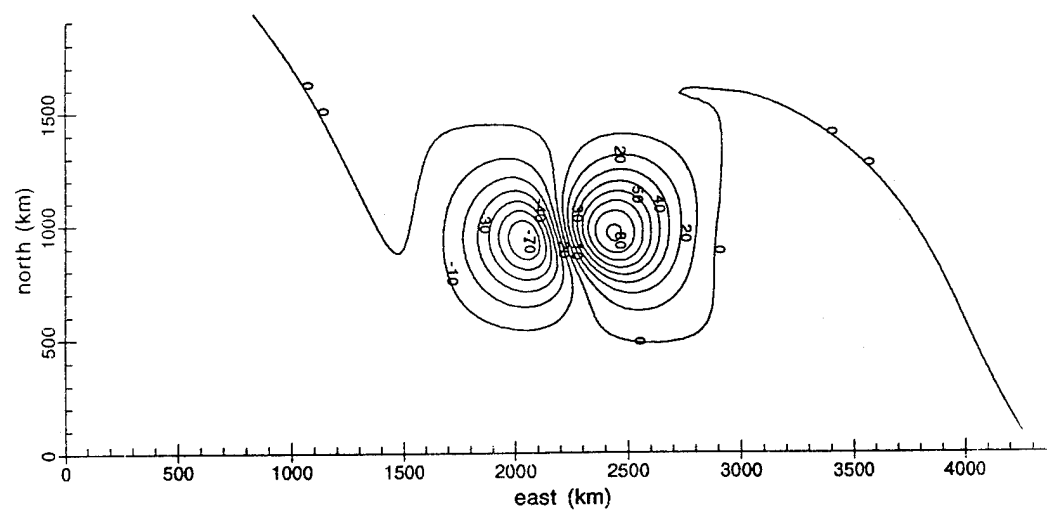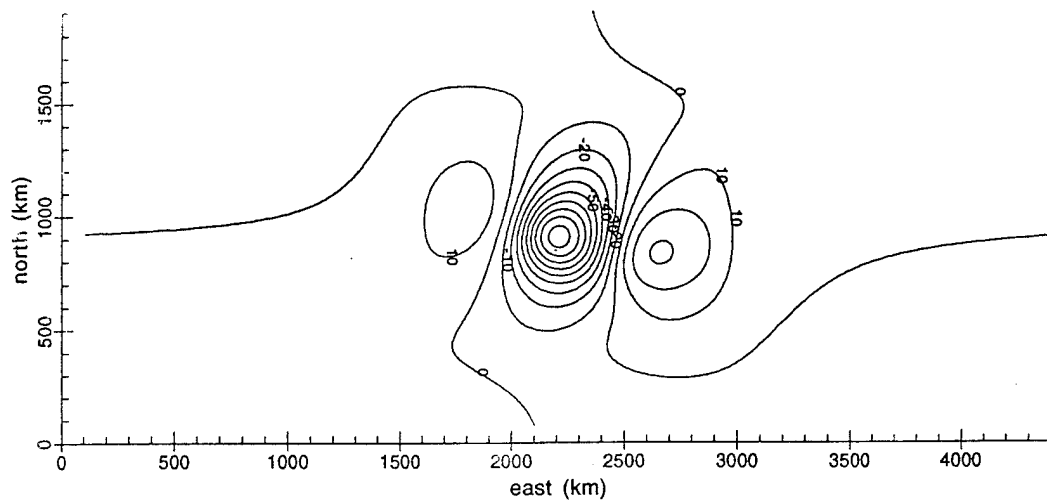
Figure 29: H (top), D (middle), and Z (bottom) components of case 2 at 6 min, in nT.
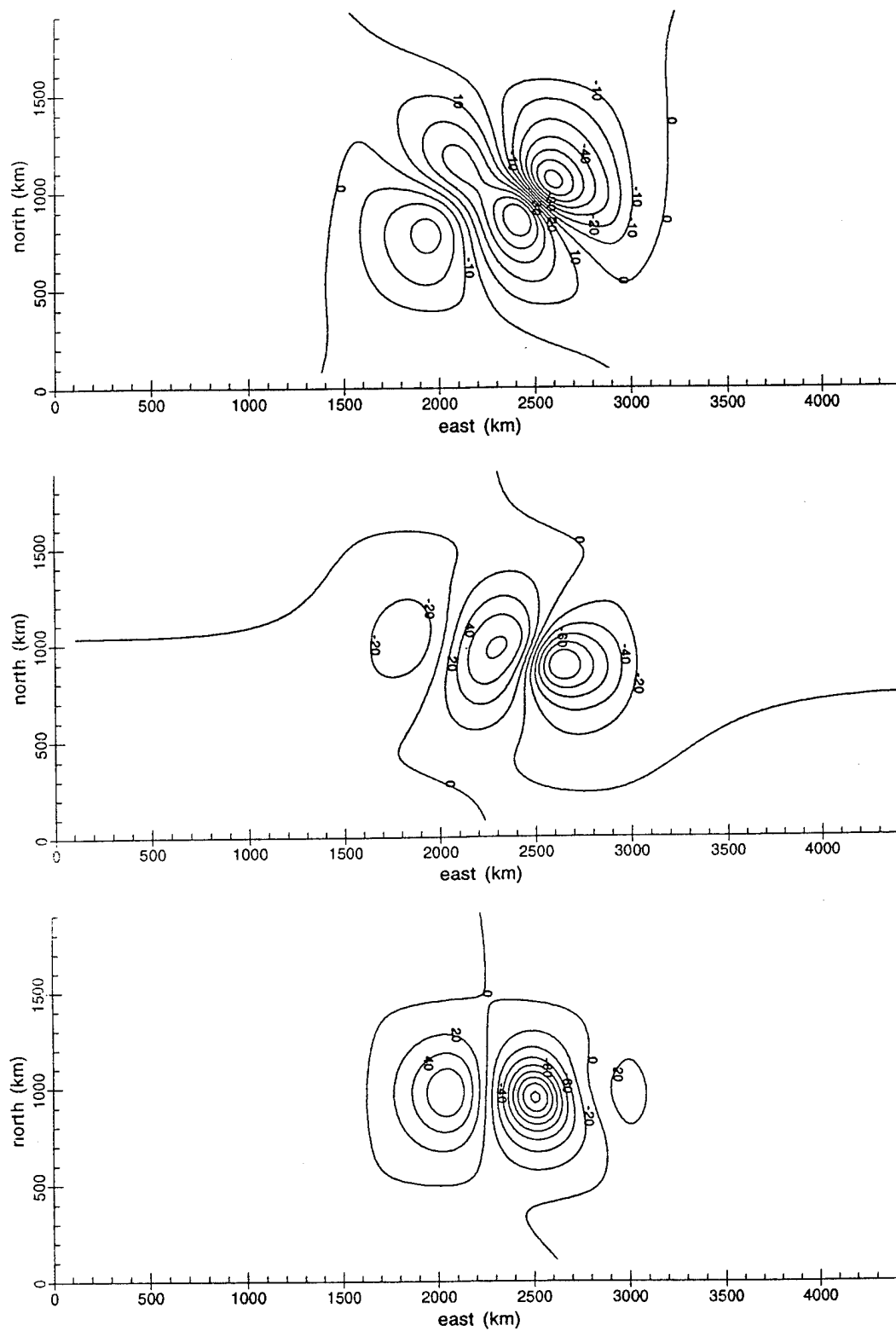
Figure 30: H (top), D (middle), and Z (bottom) components of case 3 at 6 min, in nT.

Clauer [1987] also observed this distortion. *McHenry and Clauer* [1987] ignored the effects of the conductivity gradient, and *Friis-Christensen et al.* [1988] postulated that the conductivity gradient might be the cause of the distortion. Figures 19-24 in the previous chapter do not show a similar distortion, and for that case the model was run with no conductivity gradient. This pinpoints the gradient in conductivity as the cause of the distortion.

The second series of runs used the 10-s interval data. Part of the Scandinavian magnetometer network was placed in the ground simulation grid, and the twin vortices were run overhead. The stations used are shown in Figure 31. Initially, the data were plotted out in traditional stacked magnetogram format, as in Figure 32. However, this format is difficult to interpret and could not be directly compared to the contoured output shown earlier, so contour plots were instead generated from the data. This had the additional benefits of providing a better picture of the structure of the twin vortices, and being an easier way to visualize large amounts of data.

Plots using the selected 22 Scandinavian stations are showing in Figures 33-35. These plots show all three cases at 6 min, and can be compared to Figures 28-30. Runs at 1 min and 3 min for case 1 are found in Appendix A, for case 2 in Appendix B, and for case 3 in Appendix C. These plots can be considered to be "best-case" plots. The twin vortices moved directly over and centered on the modeled ground magnetometer network.
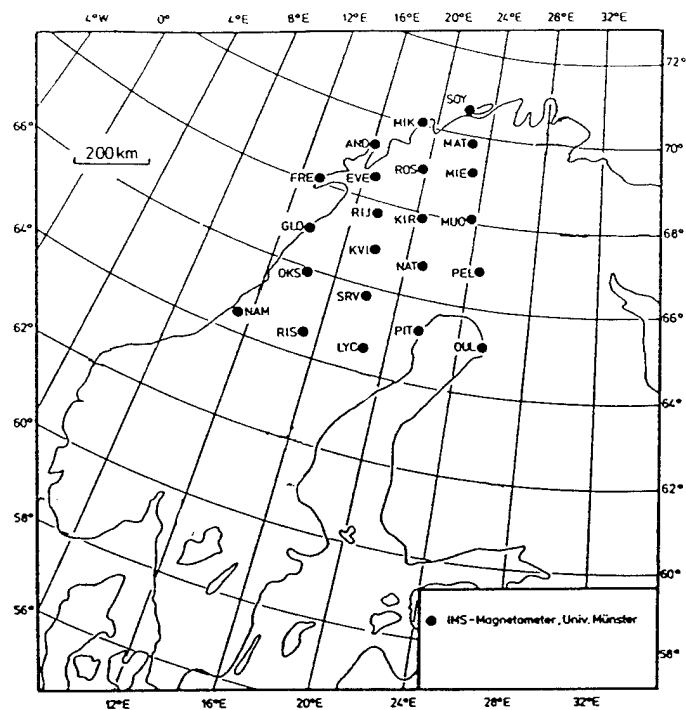
Figure 31: Location of Scandinavian stations used in simulation [*Glassmeier et al.*, 1989].
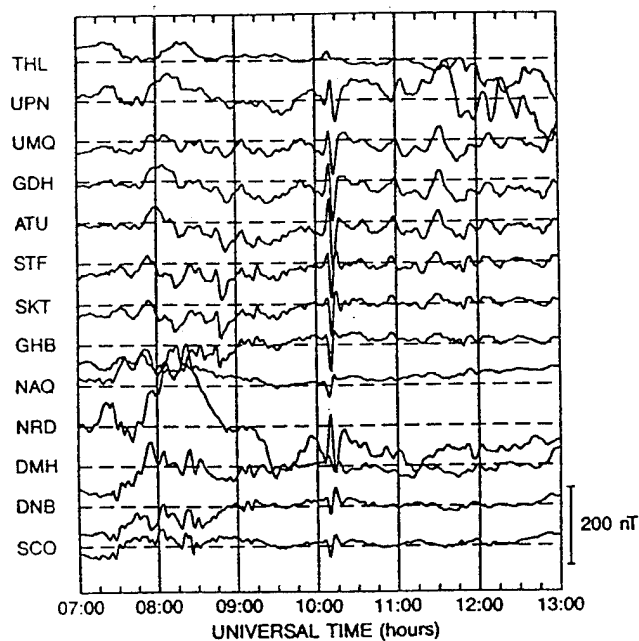
Figure 32: Sample of data presented as a stacked magnetogram [*Friis-Christensen et al.*, 1988].

Comparing these figures reveals surprisingly good results, considering howfew points were used to create the latter plots. For example, comparing the H component of Figure 28 with that of Figure 33 shows the polarity of the cells to be correct. The central values of the three cells in each plot are approximately the same. The general shape and orientation of the cells is similar also. Subjectively, the re-created plot is quite close to the original data plot.

Objectively, the data match very well also. The data from the simulated magnetometer stations were interpolated to fill a grid of the same spacing as original data over the station area, giving a one-to-one correspondence between the two data sets. This allowed the correlation coefficient to be calculated for all three cases at the 6-min interval. Appendix D discusses how correlation coefficients are calculated, how they are to be interpreted, and limitations on their use. Table 1 lists the correlation coefficients calculated for the twin vortices. The 95% confidence interval for each correlation coefficient was calculated and found to be the coefficient $\pm$~0.07. This interval is the range within which there is a 95% probability of finding the true correlation coefficient, that is, the coefficient that would be calculated if the data sets were infinitely large. The narrow intervals are due to the large number of points in each data set, and indicate
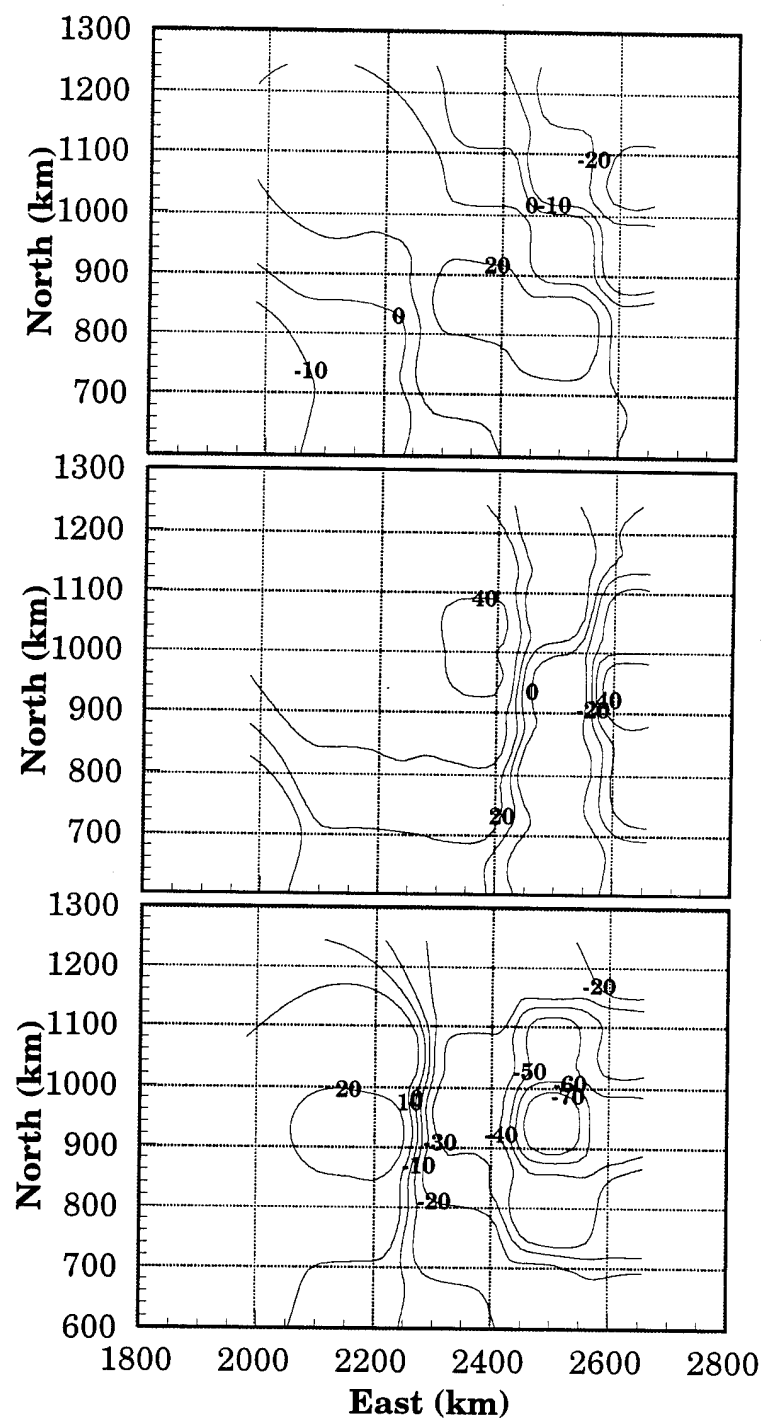
Figure 33: H (top), D (middle) and Z (bottom) components of case 1 at 6 min. Contours created from modeled station data. Contours in nT.
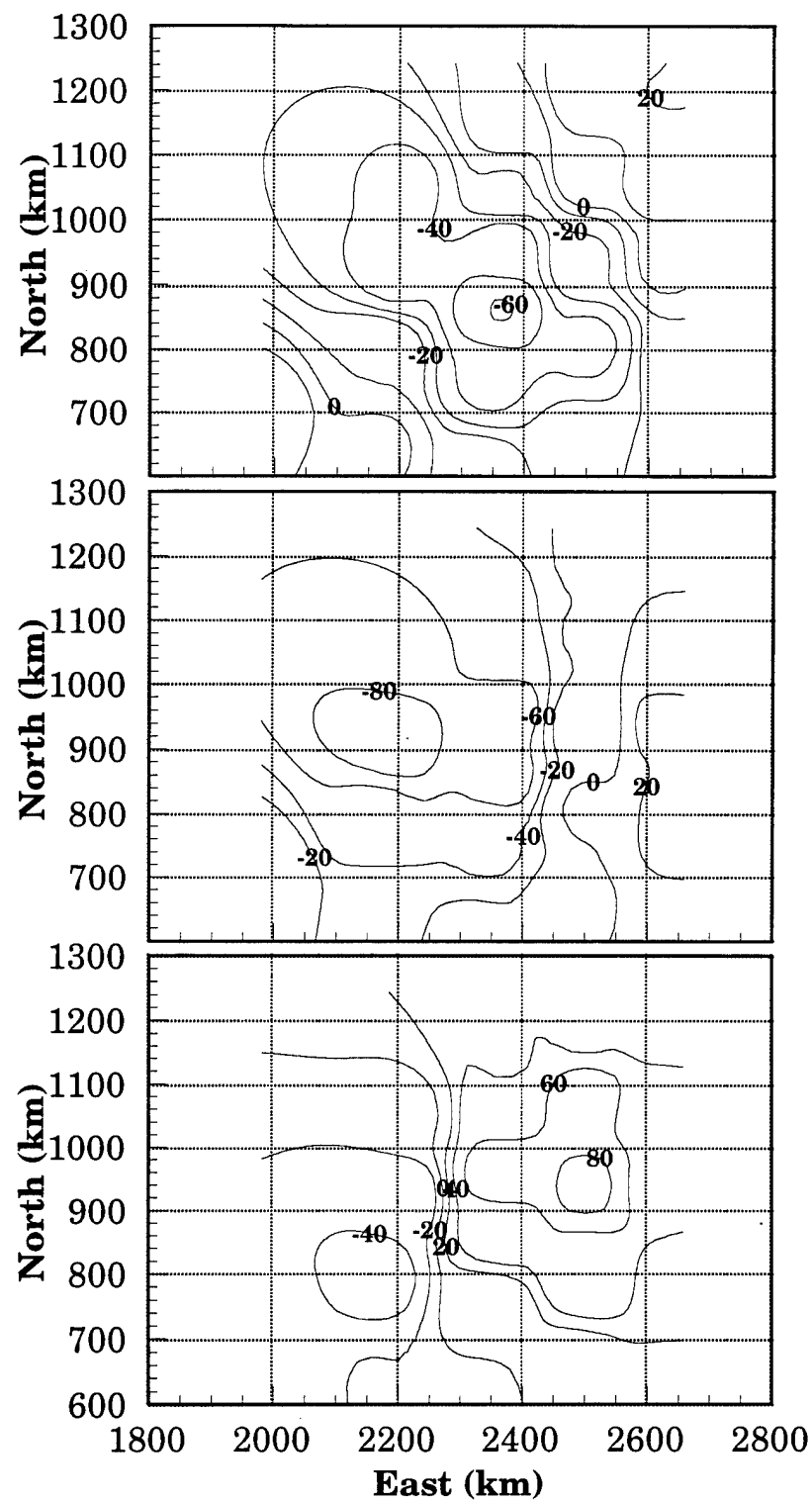
Figure 34: H (top), D (middle) and Z (bottom) components of case 2 at 6 min. Contours created from modeled station data. Contours in nT.
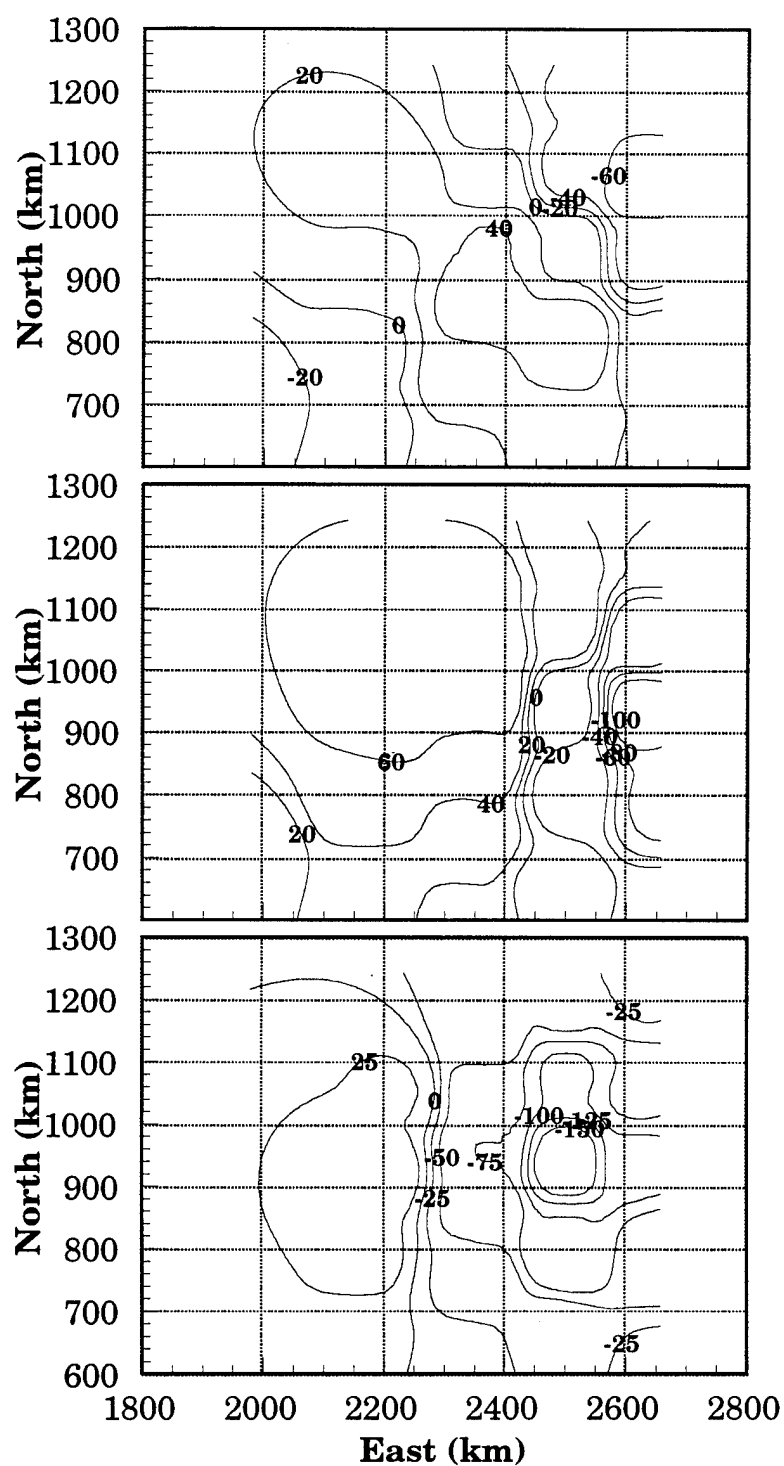
Figure 35: H (top), D (middle) and Z (bottom) components of case 3 at 6 min. Contours created from modeled station data. Contours in nT.

that the coefficients calculated are very close to the true correlation coefficient in each case.

The contour plots can provide a number of useful facts about the twin vortices. The speed of travel is relatively simple. By noting the distance that key features, such as maxima or minima, travel over a period of time it is a trivial exercise to calculate the speed. For this calculation, it is best to use the magnetograms directly in order to minimize error. This allows the time of passage of a peak to be more accurately determined. Determining the direction of travel, however, is best done from contour plots. The whole magnetic field pattern can be seen, making it much easier to note the direction of travel.

It is also possible to determine the polarity of the twin vortices; that is, whether an upward or downward field-aligned current is leading. The magnetic field contours will have either two or three cells, depending on the component being plotted. The pattern of polarity of the cells indicates the polarity of the vortices. When the upward field-aligned current leads, the

Table 1: Correlation coefficients for traveling twin vortices.

	H component	D component	Z component
Case 1	0.960	0.882	0.940
Case 2	0.923	0.799	0.939
Case 3	0.960	0.909	0.941

patterns are as follows:

1. H component has a negative-positive-negative pattern

2. D component has a positive-negative pattern

3. Z component has a positive-negative pattern

For a downward-leading field-aligned current, the above patterns are reversed in polarity.

While the Scandinavian stations are at the right location for traveling twin vortices to pass over, the vortices may not always pass over the center of a group of stations. Figure 36 shows a series of plots for case 2 where the stations were shifted north 20 km from their positions in the above runs. The dots indicate the position of the stations, with the adjacent numbers showing the magnetic field value recorded at that station. Changing the relative positions between the vortices and the stations had no major effect. Shifts of the stations from 40 km to 100 km can be found in Appendix D. The patterns remained the same, which is the most important factor in determining the characteristics of the twin vortices. The peak values, however, change as the vortices are shifted, as a station may no longer be in a position to record those values. This will affect any calculations performed to determine the intensity of the passing current system. Data from Figure 36 and Appendix D show the peak value recorded varied by about 10%.

Figure 36: H (top), D (middle), and Z (bottom) components for case 2 at 6 min. Stations shifted 20 km to the north. Contours in nT.

The stations used made it particularly easy to re-create the magnetic field with very good accuracy. However, twin vortices occur in places other than over uniform magnetometer distributions. The final simulation with the twin vortices model used only a single chain of magnetometer stations, running from SOY to OUL in Figure 31. Data were taken from the stations at 10-s intervals. Given a rate of travel, the time intervals can then be converted into distance intervals. This technique is the same used by *Glassmeier and Heppner* [1992]. There are several shortcomings to this method. It assumes the twin vortices are unchanging structures, which is not the case as they have relatively short lifetimes of 10-20 min. The speed at which they travel must be estimated, though in the run that follows, the known speed of 3 km/s was used. Figure 37 shows the results from this run, from case 2, which can be compared to Figure 29. This run can be considered a "best case" run, because the correct movement speed was known, and the center of the vortices passed over the center of the chain, though using an incorrect speed would only compress or expand the magneticfield pattern and would not affect maxima and minima. Using a single chain produced good results. The shape of the pattern remains intact, which is critical for identifying the vortices and the polarity of the field-aligned currents.

These runs have shown it is possible to gather quality information
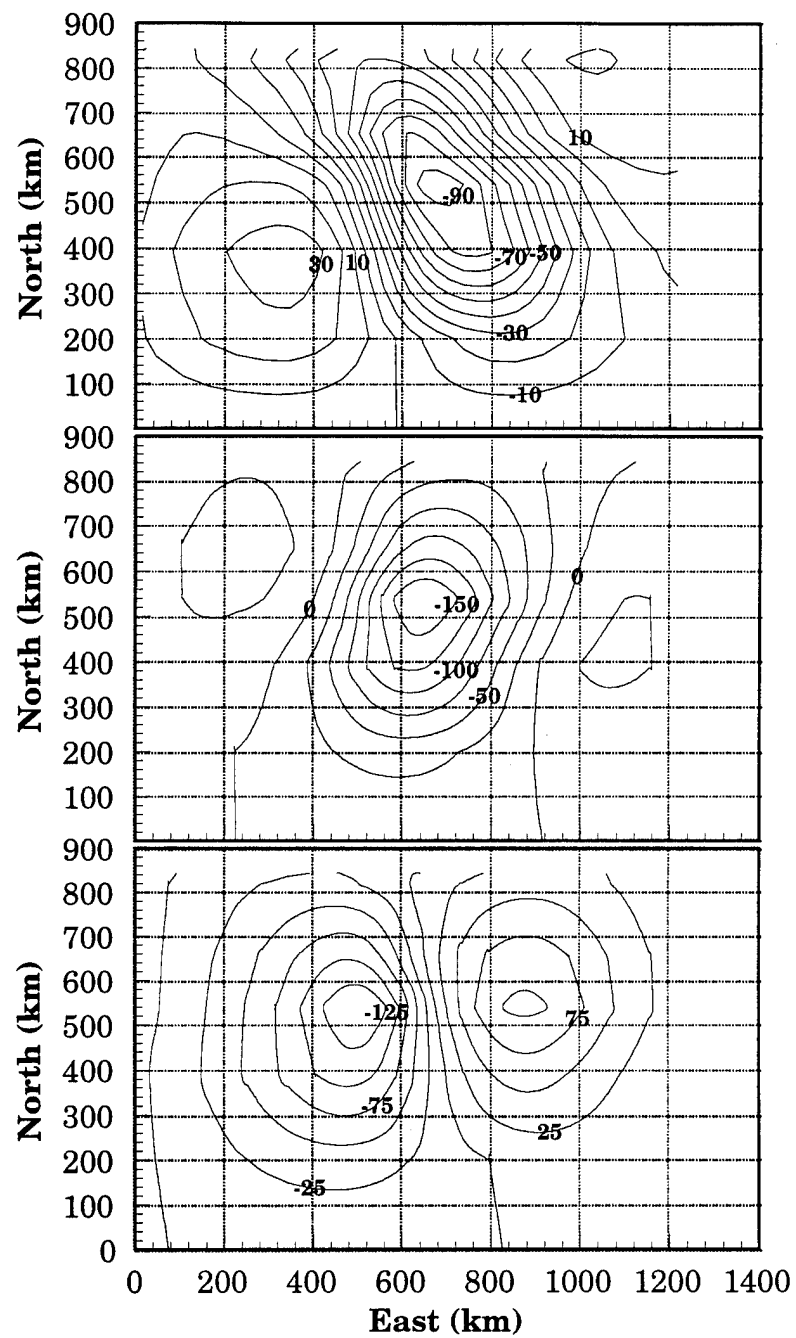
Figure 37: Twin vortices from case 2, re-created from a six-station magnetometer chain. Contours are in nT.

about twin vortices with relatively few ground observing stations. Vortices
with different characteristics leave different magnetic signatures. A
reconstruction of a particular signature does not require tremendous
amounts of data; even a coarse reconstruction will yield information about
vortices' speed of travel, polarity, and possibly current strength if a region of
peak current flow passes over a station. While a grid of magnetometers will
provide the most accurate information, a chain of magnetometers can be used
to simulate a grid, with some loss in accuracy.

CHAPTER V

GLOBAL IONOSPHERIC SUBSTORMS

To fully discover the capabilities and limitations of existing
magnetometer networks, it was necessary to model the networks on a global
scale. Input to the magnetometer simulation came from a magnetosphere-
ionosphere (M–I) coupling substorm model [*Zhu and Kan,* 1990]. The
simulation was first run with magnetometer grid spacing identical to the
data output spacing of the substorm model. This gave a complete picture of
the magnetic ground signature of the substorm, and provided a baseline
signature against which studies using the simulated magnetometer networks
could be compared. The uniformly spaced magnetometers were then replaced
with actual global distributions of magnetometers. Finally, fictitious
magnetometers were added into the actual distribution, filling any holes in
the coverage that might exist. To see if adding magnetometers to existing
networks would provide any additional benefits, magnetometers were added
only on land, leaving the oceans untouched.

The M–I coupling substorm model used is described fully in *Zhu and
Kan* [1990]; a brief summary of the processes modeled follows. Reconnection
on the dayside magnetopause, enhanced due to a southward turning of the
interplanetary magnetic field, causes enhanced antisunward convection of

open field lines and enhanced sunward convection of closed field lines. This enhanced magnetospheric convection drives enhanced ionospheric convection via Alfvén waves transmitted from the magnetosphere to the ionosphere. After the ionosphere has fully responded to the enhanced convection in the magnetosphere, the now-enhanced M–I coupling leads to the onset of the substorm.

The output of the model is in six discrete time steps: quiet time, 4, 12, 20, 28, and 36 min. Data are output in polar coordinates centered on the magnetic north pole. The radius extends from the magnetic north pole to 50°N, in 1° increments. The angle starts at noon, and continues counterclockwise in 7.5° steps. This gives a 40-by-48 point grid, for a total of 1,920 data points. Figure 38 shows the temporal evolution of the
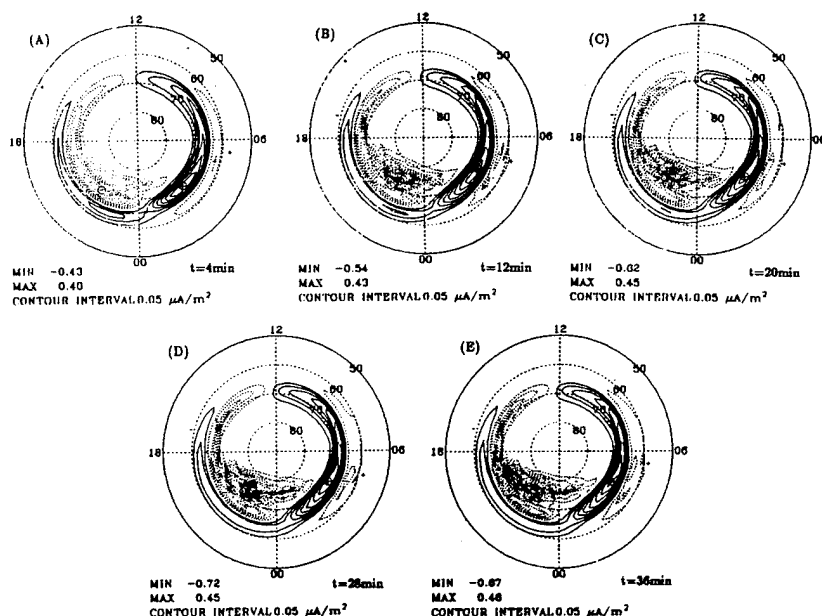
Figure 38: Temporal evolution of the field-aligned currents [*Zhu and Kan*, 1990].
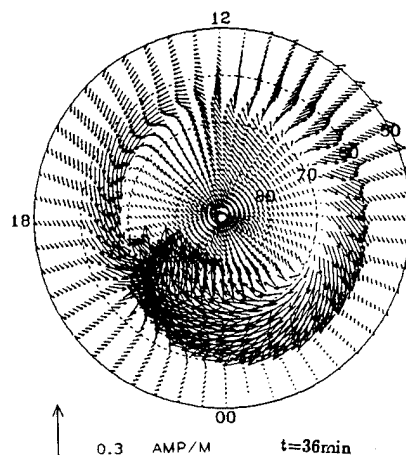
Figure 39: Horizontal currents at 36 min [*Zhu and Kan*, 1990].

field-aligned currents, and Figure 39 shows the horizontal currents at the

end of the model run (at 36 min).

The simulation of the magnetometer networks treated the area covered

as a flat disk, rather than as a curved surface. This simplified the

calculation of the magnetic field, because to do the calculation the polar

coordinates had to be changed into Cartesian coordinates, as the vector cross

product is not defined for polar coordinates. Also, no field was calculated at

the magnetic north pole, since the H and D components are not defined there.

This point was filled in later using values from surrounding points during

the contouring of the data. The horizontal currents were placed 100 km

above the ground, and the field-aligned currents extended from 100 km to

1000 km above the ground. Figures 40-42 show the H, D, and Z components at 28 min, which is near the time of the peak intensity of the substorm.

While it is a fairly simple matter to contour data that are regularly spaced, it is much more difficult to contour data that are irregularly placed. The magnetic field data from the simulated magnetometers are certainly not regularly placed. Several steps were involved in putting these data into a form that could be contoured. The data were first converted to Cartesian coordinates, for no reason other than the graphing software requires it in
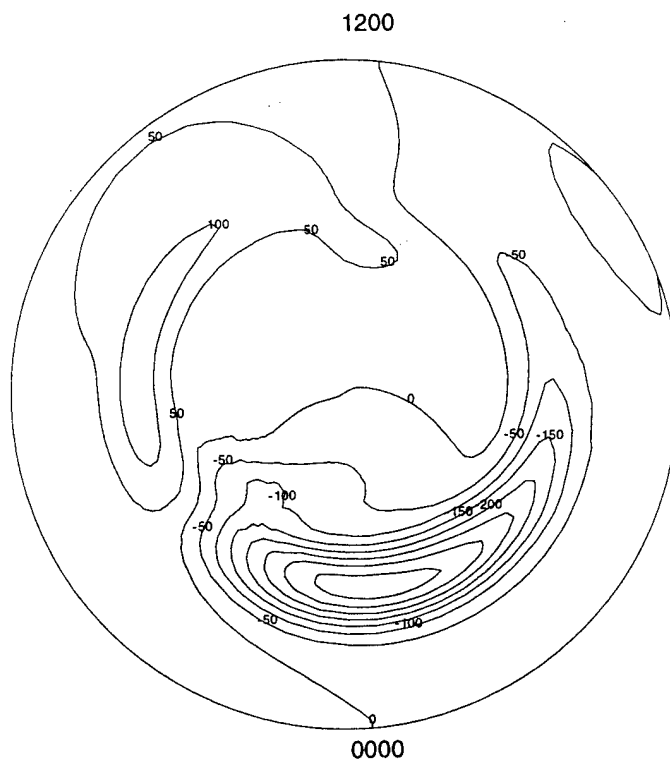
Figure 40: H component of global substorm at 28 min, contours in nT.
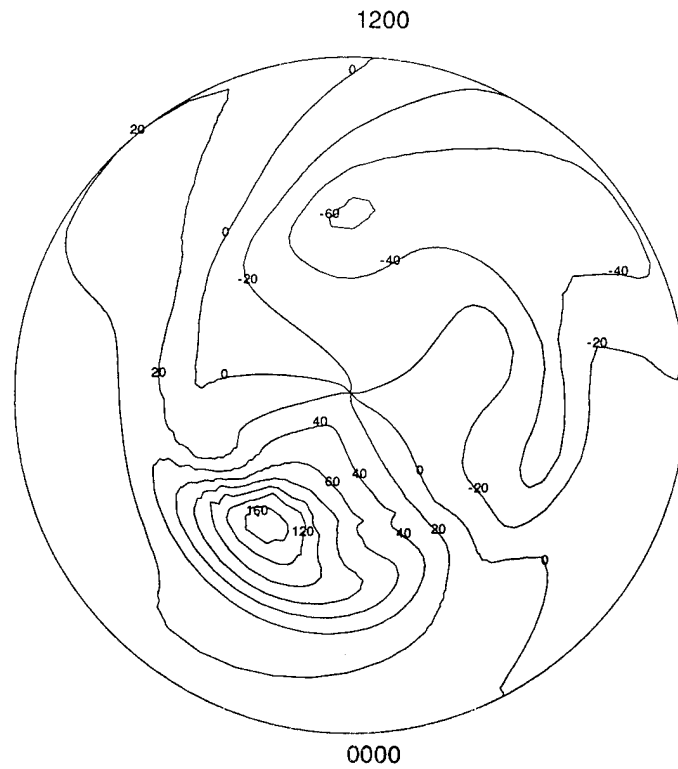
Figure 41: D component of global substorm at 28 min, contours in nT.
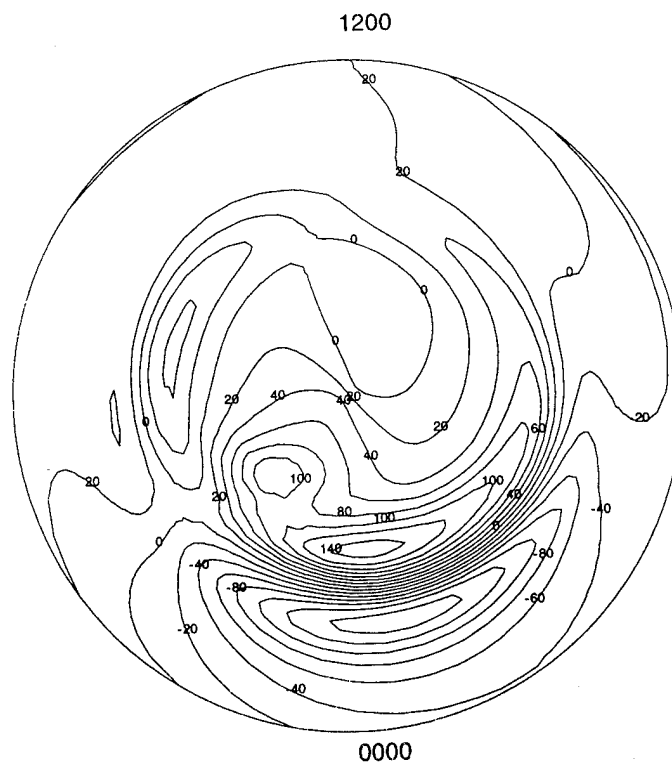
Figure 42: Z component of global substorm at 28 min, contours in nT.

that form for input. Since the simulation domain was a flat disc, there was no distortion of the data in the conversion from polar to Cartesian coordinates. A 50-point by 50-point grid, covering the simulation area, was filled by interpolating between data points. The points were weighted by the inverse of the distance to the grid point, raised to the fourth power. This served to rapidly reduce the effect of outlying points, and in tests using the fourth power gave the most accurate depiction of the data. Once the data were in the uniform grid, it became a simple matter to contour the data. The output presented below is plotted in square graphs, in these the magnetic north pole is located at point (0, 0) and 1 grid point equals 1° of latitude. For each of the runs the station grid was rotated three times with respect to the current grid, in 120° increments. This was an attempt to capture the sensitivity of the distributions to different substorm start times. Rotating the grid in 1° increments would be ideal for a very rigorous test of this, but the larger rotation angle is sufficient to give an idea of the effect of differing onset times. A "best (worst) rotation" was also used, which placed the widest and most uniform distribution of stations under the area with the most (least) concentrated currents, based on Figure 39.

The first run using actual magnetometer station locations used all the stations located above 50°N listed in The World Data Center C2 for Geomagnetism [1993] Data Catalogue, a total of 195 stations as displayed in

Figure 43. Results from the 0° rotation are shown in Figure 44, with the

additional rotations presented in Appendix F. The 195 station distribution

did an adequate job of re-creating the global ground magnetic pattern. The

peak values, both minimum and maximum, are within 60% of the actual

Figure 43: Location of 195 ground magnetometer stations.
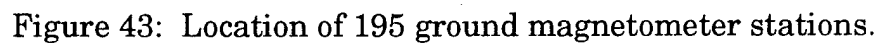
Figure 44: H (top), D (middle), and Z (bottom) components generated using data from 195 stations, 0° rotation. Contours are in nT, axes are in degrees, with 0,0 at the magnetic north pole.

values. The accuracy of these values depends whether or not the peak current strength passed over a station, and on the interpolation scheme used to create the grid. The interpolation scheme used to produce the output shown here effectively takes the nearest points and averages them together. This will produce a somewhat lower peak value; how much lower depends on the distance from the data points to the interpolated grid point. The best rotation yielded peak values that were within 15% of the actual values.

Accuracy in the peak values is important for determining the substorm's strength, but information about its morphology comes from an accurate re-creation of the ground magnetic signature. The key morphological features are the locations of the positive and negative areas, the shapes of those areas, and accurate placement of the zero line dividing the positive and negative areas. The ground magnetic signature recorded by the 195 station distribution is sufficiently accurate to identify the location and morphology of the substorm. For example, by comparing the H component of Figure 44 with Figure 40, it can be seen that the zero line is correctly identified, and the two cells are roughly the right shape. The polarities are the same between the two figures, and the peak values are at least the correct order of magnitude. The same scheme can be followed with the other components to make a subjective evaluation.

In an attempt to gain more accuracy, fictitious stations were added to the 195 real stations to fill in any gaps in the coverage. An additional 31 stations, bringing the total number of stations to 226, were added to North America and Europe. It was felt that in the real world, these would be the easiest places to add stations. Figure 45 shows the location of the additional stations.

A comparison between the output from 226 stations, Figure 46 and Appendix G, with the output from 195 stations, Figure 44 and Appendix F, shows there is very little change. With the additional stations there is a greater chance of having a station under the peak ionospheric current, so in
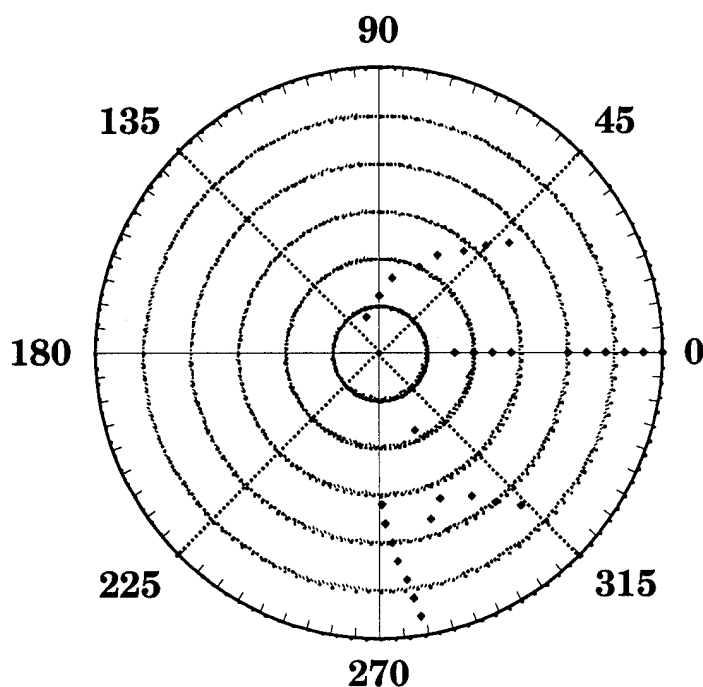
Figure 45: Location of 31 ground magnetometer stations added to the 195 station distribution.

Figure 46: H (top), D (middle), and Z (bottom) components generated using data from 226 stations, 0° rotation. Contours are in nT, axes are in degrees, with 0,0 at the magnetic north pole.

some cases additional accuracy in recording the peak value will be seen. However, there is very little new information concerning the morphological characteristics. Adding these 31 stations would not be a worthwhile or cost-effective undertaking.

In the second run, no stations were added to the former Soviet Union; for the third run 50 stations were added across Siberia. This brings the total number of stations in the simulation to 276. The new additional stations are shown in Figure 47. Output from the third run is shown in Figures 48 and Appendix H. The additional stations did bring increased accuracy to some
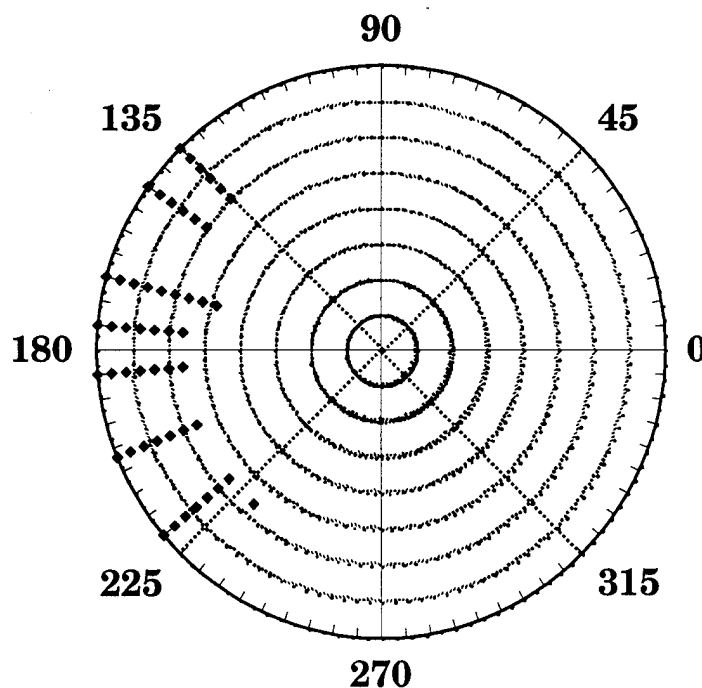
Figure 47: Location of the 50 ground magnetometer stations added to the 226 station distribution.
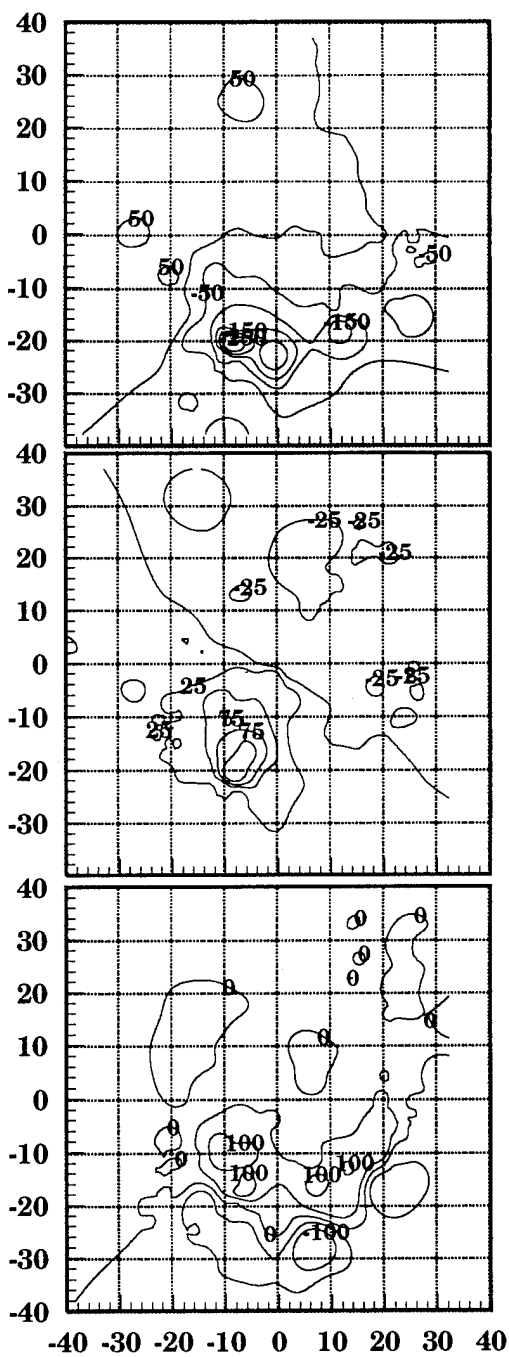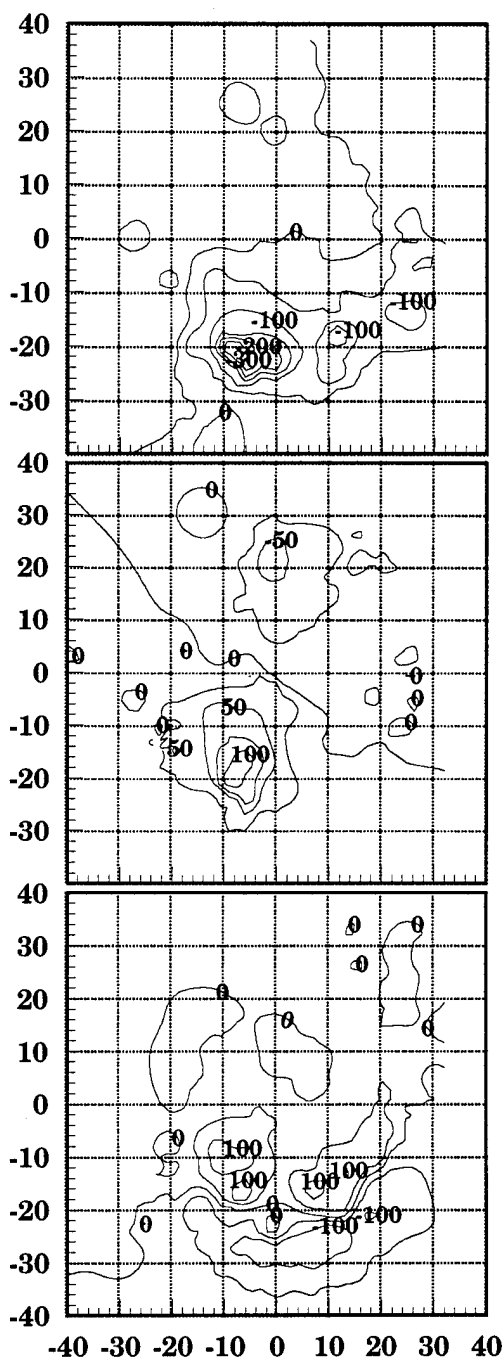
Figure 48: H (top), D (middle), and Z (bottom) components generated using data from 276 stations, 0° rotation. Contours are in nT, axes are in degrees, with 0,0 at the magnetic north pole.

peak values when the stations were in a favorable orientation with respect to the substorm. In the worst case, the additional stations were of no value, but in the best case the peak values were recorded with 90% accuracy. However, the new stations are confined to the lower magnetic latitudes. This limits their effectiveness, as much of the structure of substorms lies in higher latitudes. For the purpose of studying ionospheric substorms, it appears that adding stations across Siberia would not be a worthwhile use of resources.

The fourth and final run used fewer stations rather than more. A distribution of 67 stations was taken from current research [*Richmond and Kamide*, 1988]. Data from these stations were used by Richmond and Kamide to re-create the ionospheric and field-aligned current patterns. If these stations could be used to accurately reproduce the ground magnetic signature from the substorm model, then they should be sufficient to re-create the current patterns with some accuracy, so the goal of this test was to see if 67 stations were enough. The distribution of 67 stations is shown in Figure 49. If the data from the stations in the best rotation were not enough to accurately describe the ground magnetic pattern, then no other orientation would produce better results. If there was enough information in the data to render an accurate picture of the magnetic signature, then the goal was met, and other rotations would only produce diminished results.
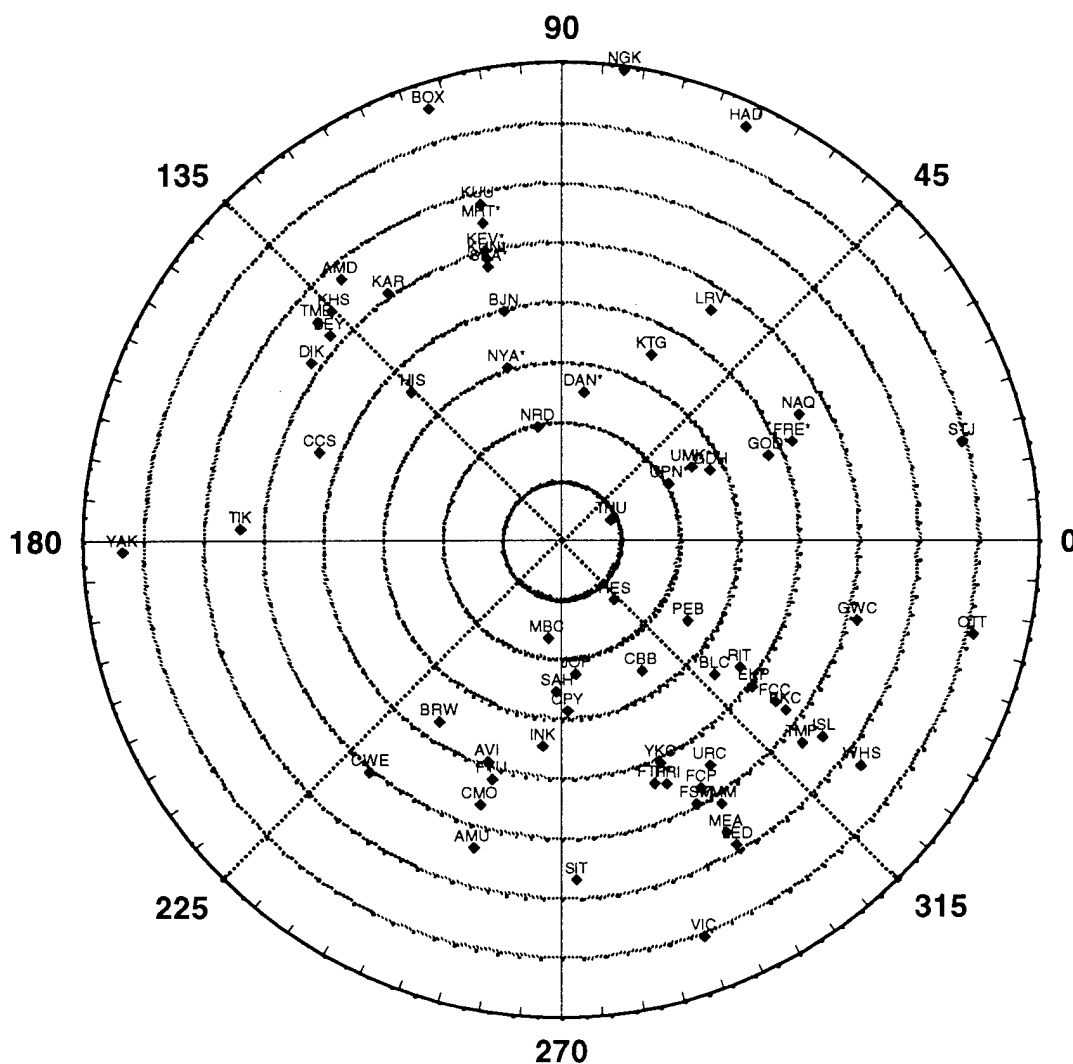
Figure 49: Location of 67 ground magnetometer stations. Stations denoted with an asterisk had no three-letter identifier.

Shown in Figure 50 are the results from the run, at the best rotation. These results are an adequate reproduction of the original pattern. With only 67 stations to cover the northern latitudes, it was expected that the peak values would be missed. The basic characteristics of the original pattern are present, and it is possible that other contouring or interpolating methods
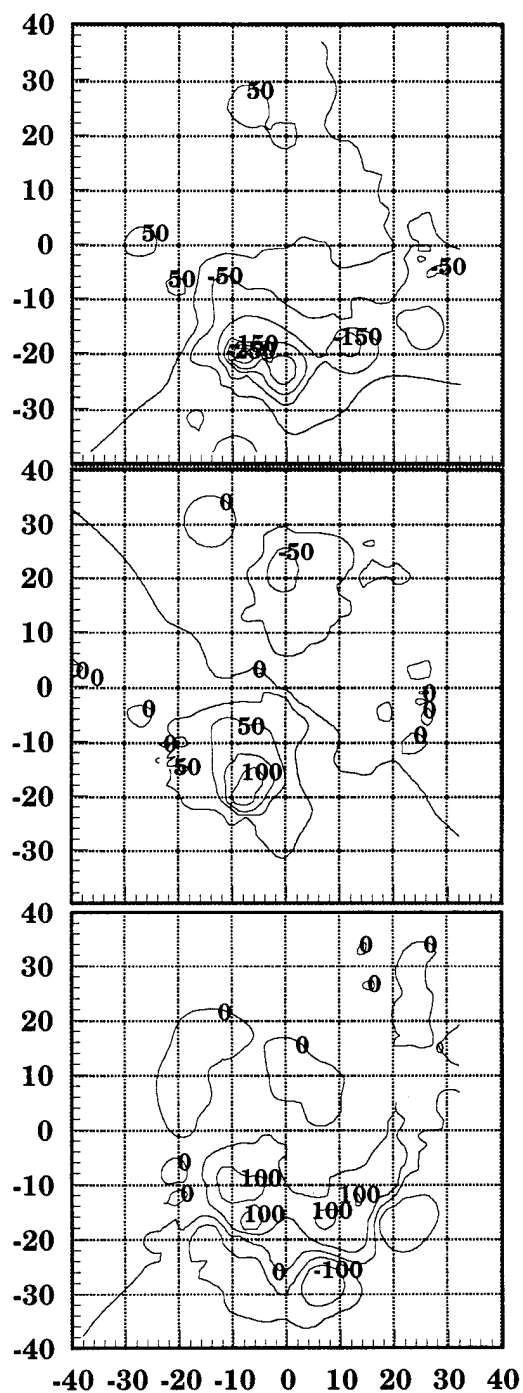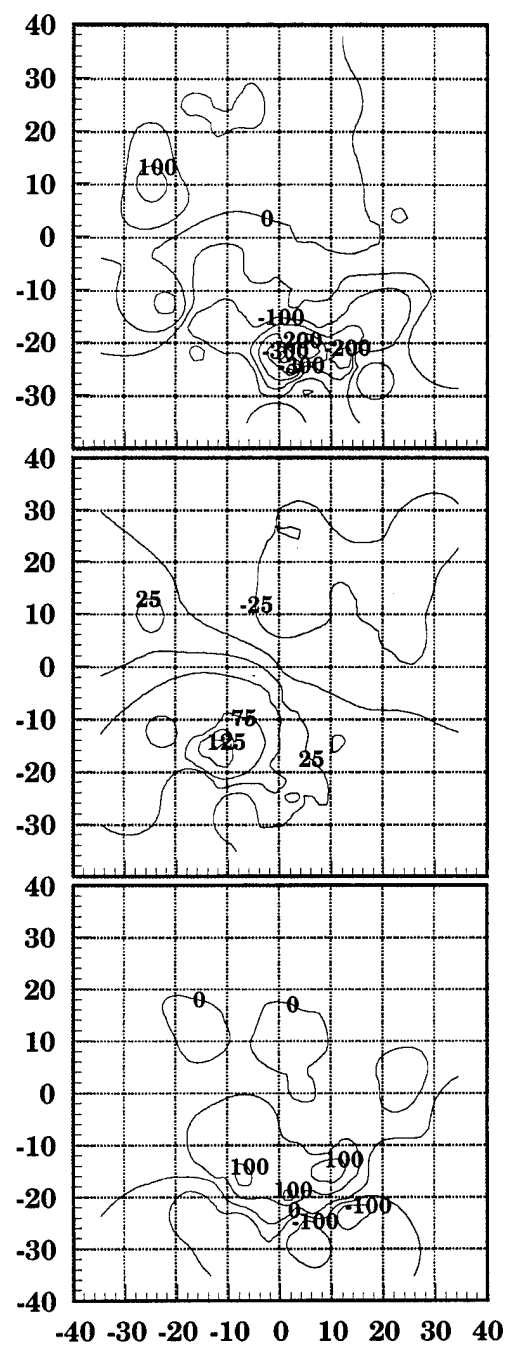
Figure 50: H (top), D (middle), and Z (bottom) components generated using data from 67 stations, 250° or "best" rotation. Contours are in nT, axes are in degrees, with 0,0 at the magnetic north pole.

could produce a more accurate picture. It is difficult to say whether or not the data from the 67 stations are enough. In the best case there is enough information to place the substorm, and track its movement and life cycle. It is likely, though, that peak values will go unrecorded, as the areas of greatest magnetic field strength are relatively small compared to the area covered by the magnetometer networks. In the worst case, it is probable that the substorm will be missed, or at least fail to be recognized as a substorm.

The conclusions drawn thus far have all been subjective, based on a manual evaluation of key features and peak values. To gain more quantified information, correlation coefficients were calculated. The two ground magnetic field data sets being compared, the data set from the 40-by-48 distribution of magnetometers, and the data set from the simulated ground magnetometer stations first had to be put into the same format. The data from the simulated stations had already been put into a 50-by-50 grid, so to match this the 40-by-48 grid point data set was interpolated to fill out a similar grid. Table 2 shows the correlation coefficients. Appendix D briefly discusses the capabilities and limitations of the correlation coefficient. As in the previous chapter, the 95% confidence interval is fairly narrow, ranging from ±0.01 for the highest coefficients to ±0.1 for the coefficients near 0.5. This means the coefficients are very close to the coefficients that would be

Table 2: Correlation coefficients for global substorm model.

		H component	D component	Z component
195 stations	**0 degrees**	0.88830	0.89003	0.87921
	120 degrees	0.90242	0.88723	0.74545
	190 degrees (best)	0.89739	0.92224	0.85603
	240 degrees	0.88889	0.91476	0.90109
	280 degrees (worst)	0.80535	0.89119	0.90985
276 stations	**0 degrees**	0.89515	0.88463	0.91947
67 stations	**250 degrees (best)**	0.79308	0.84218	0.85358
	315 degrees (worst)	0.73895	0.78400	0.84012

obtained from infinitely large data sets, and any error in the calculated coefficient is insignificant and will not affect the interpretation of the results.

These coefficients indicate the reconstruction of the magnetic field using data from the simulated ground was successful. The coefficients for the 276-station run do not demonstrate that large gains in re-creating the structure of the magnetic field signature are possible by the addition of more ground magnetometer stations. Unexpectedly high coefficients were returned by the 67-station data set. The values for the best case of the 67 stations fall within the range of values returned by the various rotations of

the 195 stations, indicating that 67 stations is a sufficient number of stations to reconstruct the magnetic field, and thus reconstruct the ionospheric current system, at least morphologically.

To assess how well the actual values were recorded, the difference between the known magnetic field pattern, generated by the uniform 40-by-48 distribution of magnetometers, and the pattern calculated from the 195 stations, was plotted against the known magnetic field values. The difference is shown in Figure 51. This clearly shows that the method of interpolating to fill a grid from the magnetic field values recorded at the

Full grid
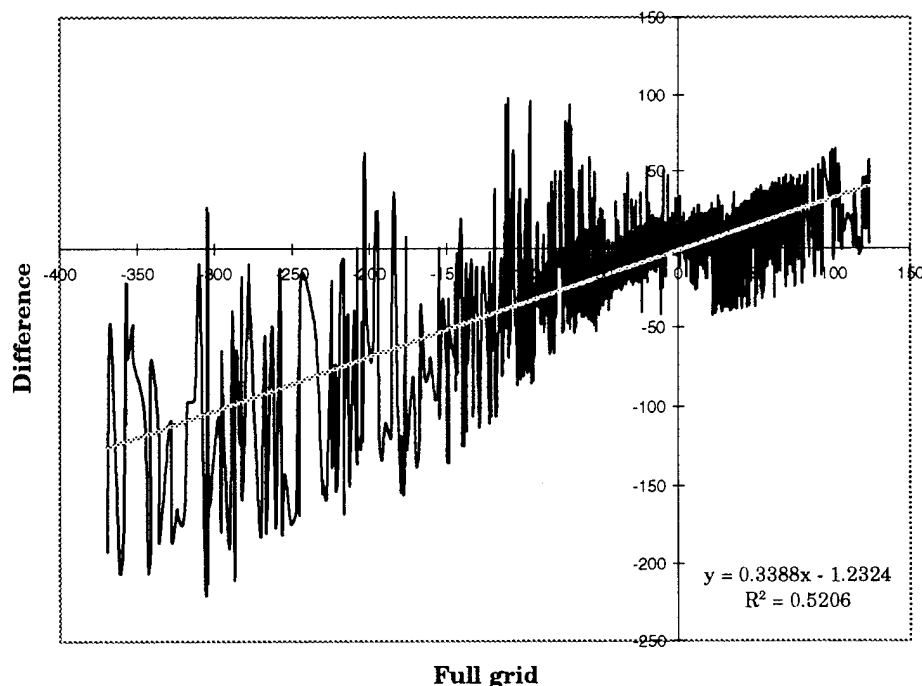
Figure 51: Difference between actual magnetic field values and values from station data as a function of actual magnetic field values. This is for H component, 195 stations, 190° rotation.

stations underestimates the magnetic field strength. Underestimation of the

magnetic field strength is not a surprise, because if the peak values were not

recorded, interpolation will only propagate the lower values throughout the

grid. As an estimate of the underestimation, a linear regression was

performed on the differences from all the data sets. The slope of the line fell

within 0.30 to 0.45. This or more advanced curve-fitting techniques may

offer a way to adjust the magnetic field values recorded at the stations to

more closely approximate the actual magnetic field values. This is an area

for further study.

Figure 52 shows a scatter plot for the H component full data set versus

the 195-station data set. This plot shows a high concentration of values near
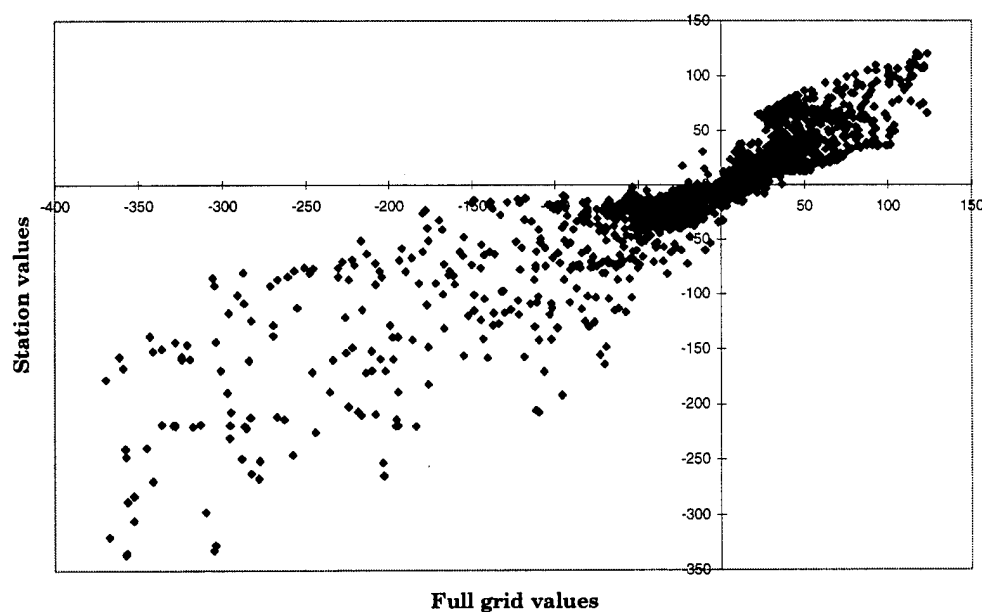
Figure 52: Scatter plot of H component values from full 40 by 48
grid versus values recorded by 195 stations at 190° rotation.

the origin, which is to be expected since the areas of intense magnetic fields
are relatively small. This led to concern that the correlation coefficients are
artificially high, since it would seem to be easier to reconstruct the areas with
little or no magnetic field, and the points near the origin appear well
correlated. Figure 53 is a histogram of the values taken from the full grid. A
large proportion of the magnetic field values falls between -50 and 50 nT. To
test the theory that the high correlation coefficients were due to the large
number of points near zero, histograms of all the full-grid data sets were
made. Points falling in the bins near the origin were discarded, and the data
were recorrelated. This would give a clearer picture on how accurately
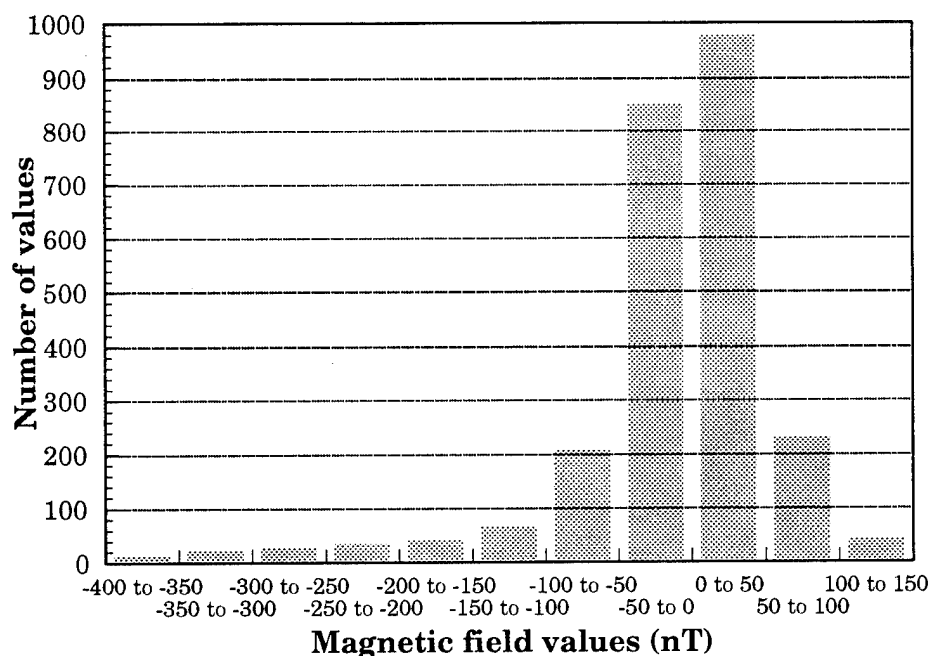
Figure 53: Histogram of data from H component. Values are from 40-by-
48 grid.

the stations were able to record the ground magnetic field pattern where the field strength was not nearly zero. These values provide most of the information and structure, as opposed to the values closer to zero which make up the background. Table 3 shows correlation coefficients without the central values. The coefficients, almost without exception, increased. This means the stations recorded enough information about areas of larger magnitude magnetic fields to provide for an accurate reconstruction of the pattern.

Table 3: Correlation coefficients for global substorm model. Data near zero have been removed.

		H component	D component	Z component
195 stations	**0 degrees**	0.91243	0.90049	0.89913
	120 degrees	0.91663	0.89384	0.75539
	190 degrees (best)	0.90574	0.92594	0.88335
	240 degrees	0.95027	0.89269	0.91969
	280 degrees (worst)	0.95040	0.94908	0.94390
276 stations	**0 degrees**	0.89828	0.91371	0.94368
67 stations	**250 degrees (best)**	0.92804	0.91296	0.93043
	315 degrees (worst)	0.87727	0.71180	0.86312

These runs have shown it is possible to capture a global picture of an ionospheric substorm with existing magnetometer distributions. The next step was to determine if it was possible for existing magnetometers to resolve any fine structures in a substorm. More specifically, could the data from magnetometers be used to locate the substorm current wedge? The current wedge is a field-aligned current that flows from the magnetosphere into the ionosphere at the dawnward side of the substorm, across the ionosphere as a westward auroral electrojet, and back up to the magnetosphere as a field-aligned current at the duskward side of the substorm. It is thought to act as a short circuit, disrupting the current flow across the tail of the magnetosphere [*Lui,* 1994]. The magnetic ground signature of the current wedge can be seen most clearly in the Z component (Figure 42), but also in the H component (Figure 40). It is the small area of increased magnetic field strength near the pole, at about 2000 local time. Looking at the output from the 195 stations, it is difficult to tell if the footprint of the current wedge can be seen, or contours in that area are the result of errors in interpolation or contouring. Since the strength of the current wedge changes rapidly with time, changes in the ground magnetic signature were examined. This was done by filling in a regular grid through interpolation using data for the Z component from the magnetometer stations. Grids from different time slices were then differenced – more specifically the 20-min grid was subtracted

from the 28-min grid, and the 28-min grid was subtracted from the 36-min grid. The differenced grids were then contoured to highlight the changed areas. The results from this exercise were surprisingly good, and are shown in Figures 54-58. In all cases, including the grids generated with data from the 67 stations, the magnetic signature from the substorm current wedge was located to within a few hundred kilometers. While the magnitude of the differenced magnetic field is relatively small, about 5% of the original magnetic field strength, it clearly stands out and highlights the speed at which the current wedge changes compared to the rest of the substorm. Figure 59 shows the difference between two time slices using the data from the 40-by-48 grid. The area of the substorm current wedge is quite prominent here also, but the magnitudes are up to five times greater than those in the plots from station data. This demonstrates that the data from the stations were able to capture the correct structure of the ground magnetic field, but peak values were missed. Real-world data would have to be examined to determine if such small signatures, like those from the differenced station data, would be lost in the background noise, or if the background would cancel out, leaving distinct magnetic signatures. The area of the current wedge is relatively small compared to the total area of the simulation domain. It is to be expected that detecting the current wedge would be more dependent on the location of the substorm with respect to the

Figure 54: Difference between 36 min and 28 min (left) and between 28 min and 20 min (right) for 195 stations, 0° rotation, contours in nT.

Figure 55: Difference between 36 min and 28 min (left) and between 28 min and 20 min (right) for 195 stations, 120° rotation, contours in nT.

Figure 56: Difference between 36 min and 28 min (left) and between 28 min and 20 min (right) for 195 stations, 190° ("best") rotation, contours in nT.

Figure 57: Difference between 36 min and 28 min (left) and between 28 min and 20 min (right) for 195 stations, 240° rotation, contours in nT.
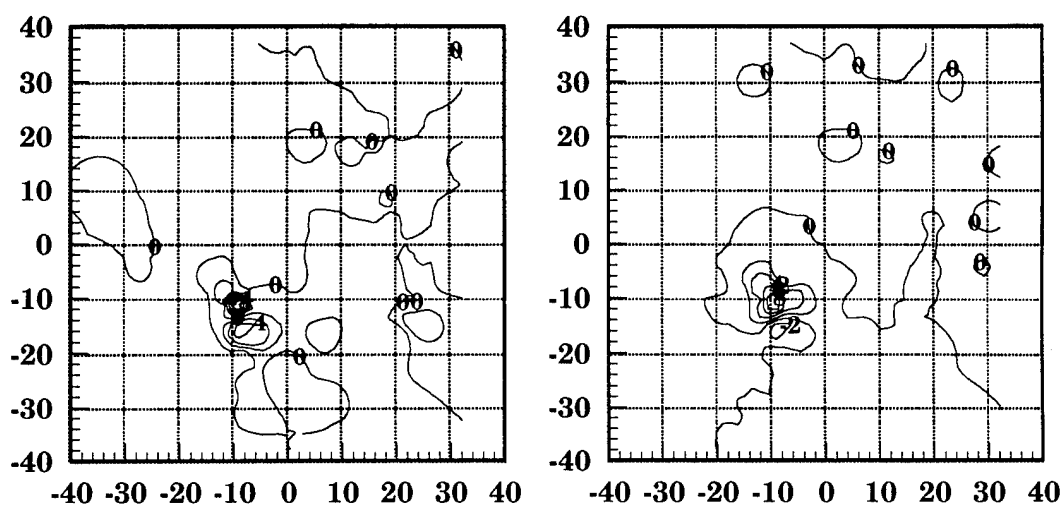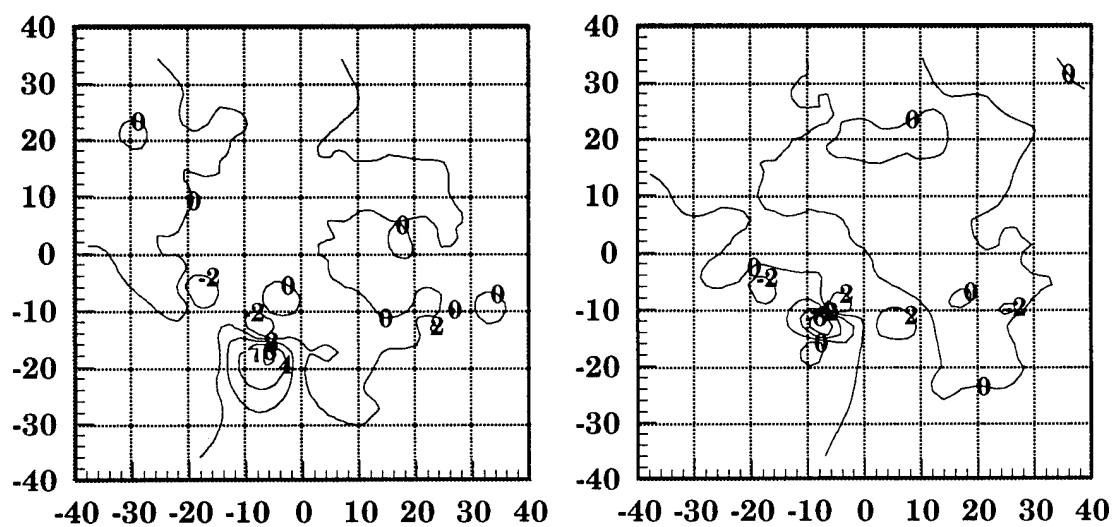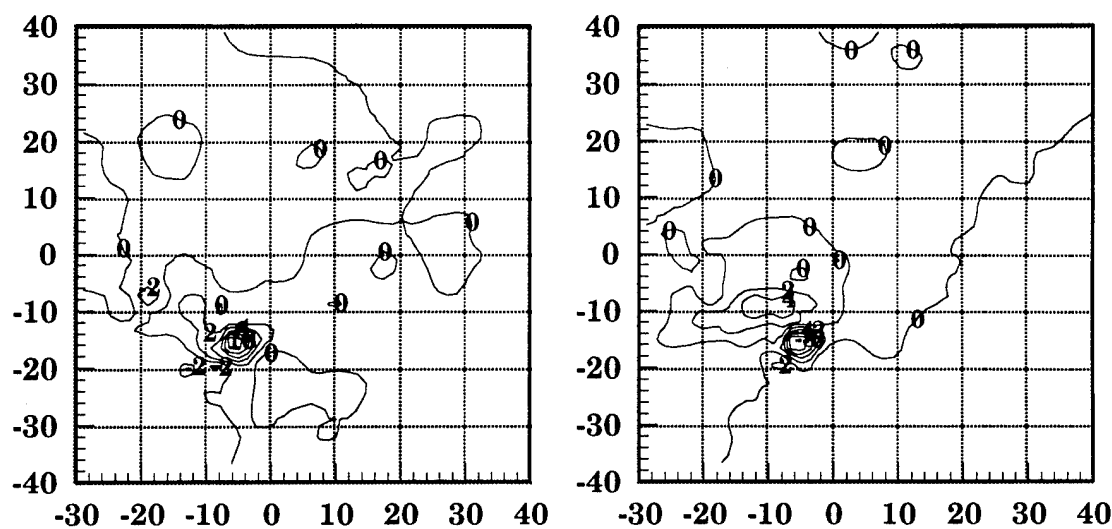
Figure 58: Difference between 36 min and 28 min (left) and between 28 min and 20 min (right) for 67 stations, 250° ("best") rotation, contours in nT.
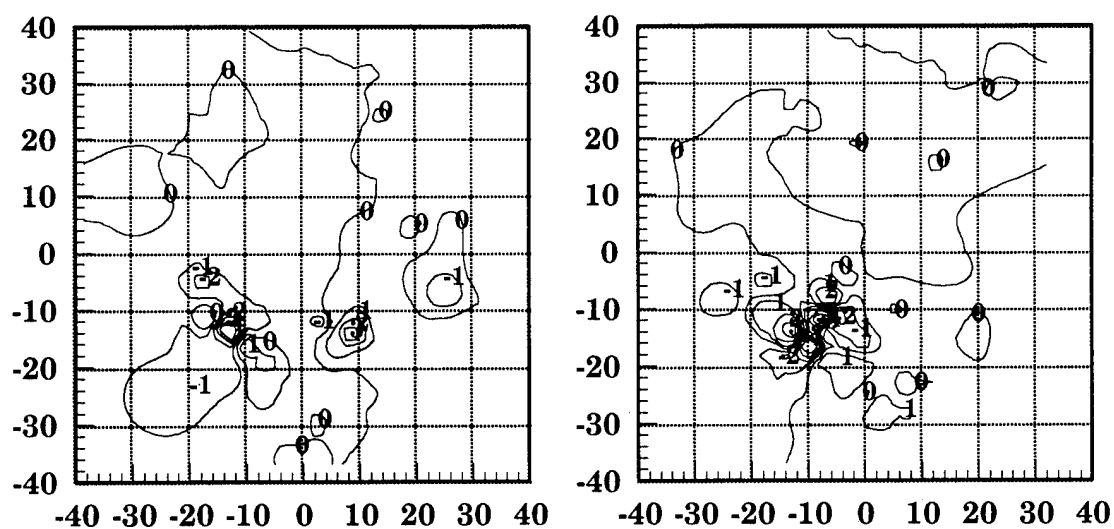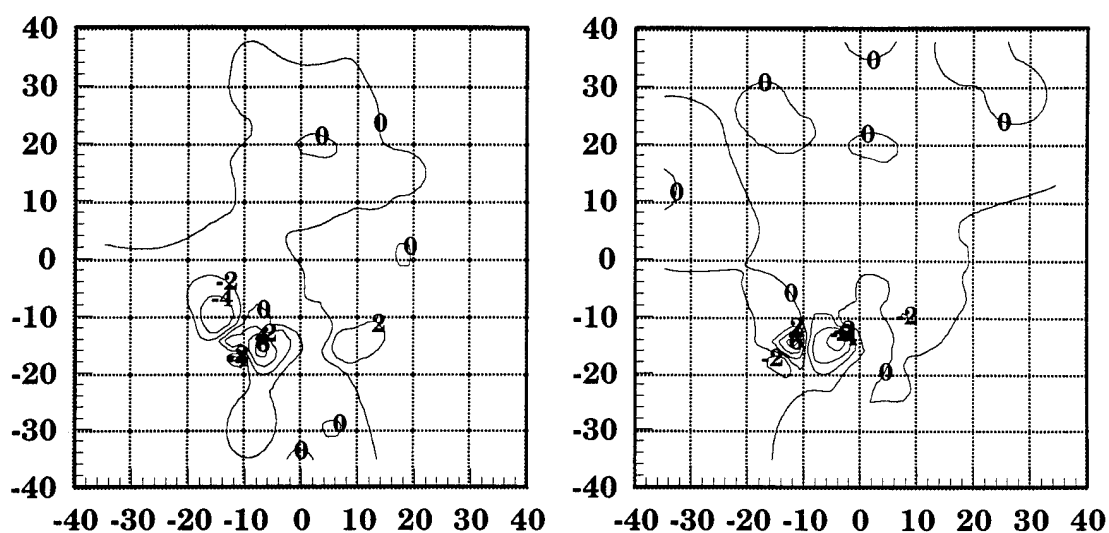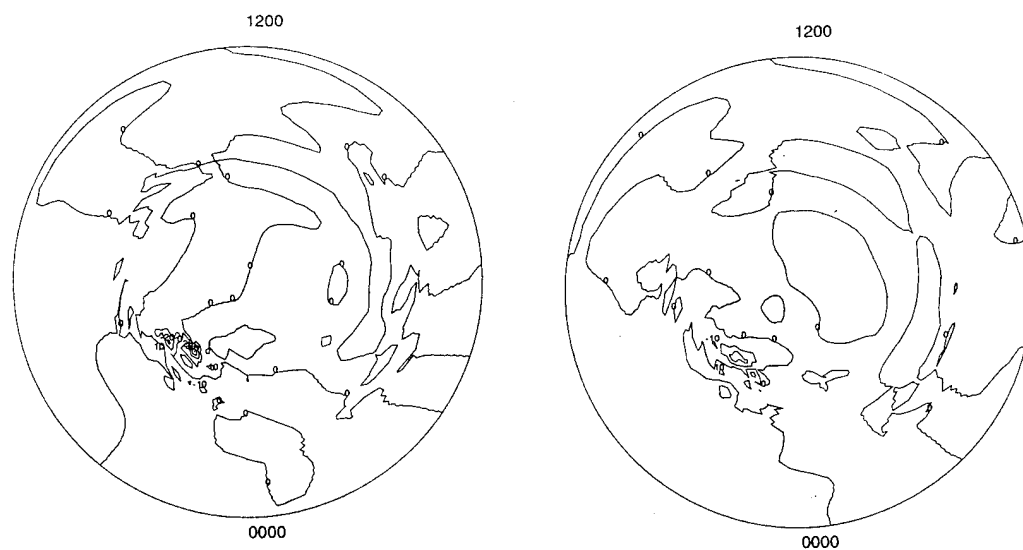

Figure 59: Difference between 36 min and 28 min (left) and between 28 min and 20 min (right) for data from 40-by-48 station grid.

ground stations. Correlation coefficients were calculated using only data from a 2000-km by 2000-km area under the current wedge. These values are shown in Table 4. Generally, the correlation coefficients are lower than the previous coefficients calculated for the whole substorm. The magnitude of the coefficients can be related back to the structure of the magnetic field pattern. The H component has the least complex magnetic field structure in the current wedge area. This is reflected by the higher correlation coefficients for the H components. At the other extreme, the Z component, which has the most activity in that area, shows the least correlation. As was expected, the coefficients were very low for the worst case orientation of the 67 stations.

Table 4: Correlation coefficients for global substorm. Data are taken from area under the substorm current wedge.

		H component	D component	Z component
195 stations	190 degrees (best)	0.91376	0.87407	0.94547
	280 degrees (worst)	0.87384	0.90030	0.81570
276 stations	0 degrees	0.91647	0.81450	0.77253
67 stations	250 degrees (best)	0.84096	0.81464	0.78813
	315 degrees (worst)	0.65705	0.54200	0.67325

It would appear, then, that the existing magnetometer networks are sufficient to study ionospheric substorms. No large gains in accuracy can be made by adding more magnetometers; however, more magnetometers do increase the likelihood of recording peak magnetic field strengths. With some luck, even limited magnetometer distributions can be used to provide accurate information about global substorms, and perhaps more sophisticated data analysis techniques than those used here can enhance the quality and usefulness of the data provided. Limited magnetometer distributions can also be successfully used to pinpoint areas of activity that take place on a shorter time scale than the substorm itself, but the substorm must be oriented properly with respect to the station distribution to obtain accurate magnetic field strengths.

CHAPTER VI

SUMMARY AND CONCLUSION

Summary

A model was developed that was used to simulate a ground-based magnetometer. This simulated magnetometer was used in conjunction with simple current systems to validate the model, and to gain an understanding of the sensitivities of the magnetic field to variations in the current system. With the model validated, it became a powerful tool to study the response of the ground magnetic signature to ionospheric currents, and to discover the capabilities and limitations of ground magnetometer networks already in place. This tool was first used to verify Fukushima's theory, which states that the field-aligned current and Pedersen current will cancel in a uniform conductivity ionosphere that is parallel to the ground with perpendicular field-aligned currents. The theory was tested using a number of different current systems. Models of more complex current systems, traveling convection twin vortices and global ionospheric substorms, were used as input into distributions of the simulated ground magnetometer. The output from these runs was studied to determine the abilities of existing magnetometer chains, and the potential for improvement by adding additional magnetometers.

Conclusion

From the studies conducted with simple wire currents, it was seen that the bulk of the magnetic field is caused by the most local currents. This result was expected since the Biot-Savart law is an inverse square law, but it is always comforting to see even the most basic theory pan out in practice. A more complex and less intuitive theory, Fukushima's theory, was also shown to be correct within the limits of the models and for the conditions stated above. This theory allows ionospheric modelers to discard the effects of the field-aligned and Pederson currents when considering the ground magnetic effect of an ionospheric storm for certain storm configurations, and also provides a known result against which models can be tested.

Traveling convection twin vortices were modeled and passed conveniently over a fairly dense region of magnetometers. By creating contour plots of the magnetic field data rather than generating magnetograms, the data are much easier to digest and understand, and the contoured output provides a more effective way of presenting large quantities of data. It is my recommendation that the community use contour plots instead of stacked magnetograms when presenting data from 2-D arrays of magnetometers. Through this method it was shown that only a limited station distribution, or even a single line of stations, is needed to re-create the ground magnetic field pattern caused by the twin vortices. Correlating

the station data with the gridded data from the model supports this conclusion. Stations in the Scandinavian Magnetometer Array are at the correct latitudes to observe twin vortices, and the stations are close enough to each other so the peak magnetic field recorded will likely be close to the actual peak. In this initial study the 22 simulated stations were able to record at least 70% of the peak values. The combination of an accurately reconstructed ground magnetic signature and peak values that are close to their true values is of great benefit to researchers calculating the ionospheric currents.

The same method of ground magnetic field reconstruction and analysis was applied on a global scale to study global ionospheric substorms. It was shown that there is no appreciable benefit to adding many more ground magnetometer stations, other than increasing the likelihood of capturing peak magnetic field values. Subjective and objective methods of comparing the reconstructed magnetic field with the model output reveals that the ground magnetic field can be successfully re-created from as few as 67 stations. How successful depends on the relative orientation between the substorm and the ground magnetometer distribution. The re-created magnetic field strength will always be low, however. If peak magnetic field strength is not recorded, the interpolation that takes place will not restore it. In this study using from 67 to 276 ground magnetometer stations, the

method on average records values that are 30-50% of the actual magnitude of the magnetic deflections. It must also be noted that while the modeled stations do a good job of re-creating the ground magnetic field pattern, a point-by-point comparison between the data set from the stations and the known data set would reveal wide variations between the two data sets.

Areas for Further Study

This research has answered a number of questions; however, it seems as if there are now even more questions unanswered. Many aspects of the research could be enhanced, and there are several paths for new research to take. The ionospheric models used is one area that could be improved. The ionosphere was treated as a flat sheet, when in fact it does have a vertical dimension and currents that vary with height. The field-aligned currents are also not necessarily perpendicular to the ionosphere at all heights. Improving the ionospheric models would provide magnetic signatures closer to what is actually observed, though these changes should not affect the results of this research. The modeled ground magnetometer distributions could also be made more realistic. Most researchers today agree that the Earth is not the flat disc it was treated as in the global substorm study. Placing the magnetometers on the surface of a sphere rather than a plane would change the distance between magnetometers and between the magnetometers and ionospheric currents. The introduction of induced

ground currents would also affect the magnetic field recorded by the ground magnetometers.

The methodology used to study the results also has room for further improvement. Interpolation is relied upon quite heavily to produce results, but the method of interpolation used is quite simple. There undoubtedly exist more elegant solutions to the problem of interpolating from a nonuniform grid, and it is quite likely these solutions would provide better results. Infusing the interpolation scheme with some knowledge of magnetic field behavior could possibly provide a more accurate picture of the ground magnetic signature; however, doing this runs the risk of confining the result to a presupposed answer. The difference between the actual magnetic field values and the reconstructed magnetic field values appears roughly to be a function of the actual magnetic field values, as seen in Figure 54. Discovering this function could provide researchers with the ability to better approximate magnetic field strengths, and hence ionospheric current strengths. Inverting the reconstructed magnetic field to obtain the ionospheric current patterns would test how accurate the method of inversion is, in addition to how well correlated the magnetic field data have to be to obtain an accurate picture of the ionospheric currents.

Using actual magnetometer measurements is an obvious next step to the research. The magnetic field pattern could be constructed and compared

to the theoretical patterns presented here. This would allow an examination into the effects of random background magnetic field fluctuations on the reconstructed signature. Looking for the substorm current wedge using real data would be a very valuable and informative test. The magnetic signature of the current wedge is very obvious in noise-free modeled data – it is not clear if the signature would be lost in noisy real-world data.

The simulated magnetometer developed for this research has proved to be a valuable tool, when used in conjunction with ionospheric current models. The usefulness of this tool can be increased by using it to study more realistic ionospheric current systems, on a more realistic simulation domain (i.e., a curved Earth). Comparing output from the simulated magnetometer with actual magnetometer data will provide more insight into the accuracy and limitations of the simulated magnetometer. These areas of future research should be pursued, as the results can provide the research community with valuable information about the accuracy of methods currently employed.

REFERENCES

Friis-Christensen, E., M. A. McHenry, C. R. Clauer, and S. Vennerstrøm, Ionospheric traveling convection vortices observed near the polar cleft: a triggered response to sudden changes in the solar wind, *Geophys. Res. Lett., 15,* 253, 1988.

Fukushima, N., Equivalence in ground geomagnetic effect of Chapman-Vestine's and Birkeland-Alfvén's electric current-systems for polar magnetic storms, *Rep. Ionos. Space Res. Jpn., 23(3),* 219, 1969.

Glassmeier, K. H., Traveling magnetospheric convection twin-vortices: observations and theory, *Ann. Geophysicae, 10,* 547, 1992.

Glassmeier, K. H., and C. Heppner, Traveling magnetoshperic convection twin vortices: Another case study, global characteristics, and a model, *J. Geophys. Res., 97,* 3977, 1992.

Glassmeier, K. H., M. Hönisch, and J. Untiedt, Ground-based and satellite observations of traveling magnetospheric convection twin vortices, *J. Geophys. Res. 94,* 2520, 1989.

Heikkila, W. J., T.S. Jorgensen, L. J. Lanzerotti, and C. G. Maclennan, A transient auroral event on the dayside, *J. Geophys. Res. 94,* 15291, 1989.

Jacobs, J. A., *Geomagnetism, Vol. 1,* Academic Press, London, 1987.

Kelley, M. C., *The Earth's Ionosphere,* Academic Press, San Diego, Calif., 1989.

Lui, A. T. Y., Mechanisms for the substorm current wedge, *Proceedings of the Second International Conference on Substorms,* 195, November 1994.

McHenry, M. A., and C. R. Clauer, Modeled ground magnetic signatures of flux transfer events, *J. Geophys. Res., 92,* 11231, 1987.

Moore, D. S. and G. P. McCabe, *Introduction to the practice of statistics, 2nd ed.,* W. H. Freeman and Co., New York, 1993.

Needham, J., *Science and Civilisation in China, Vol. 4,.* Cambridge University Press, Cambridge, U.K., 1962.

Reitz, J. R., F. J. Milford, and R. W. Christy, *Foundations of Electromagnetic Theory, 4th ed.*, Addison-Wesley Publishing Company, Reading, Mass., 1993.

Richmond, A. D., and Y. Kamide, Mapping electrodynamic features of the high-latitude ionosphere from localized observations: technique, *J. Geophys. Res., 93,* 5741, 1988.

Schunk, R. W., L. Zhu, and J. J. Sojka, Ionospheric response to traveling convection twin vortices, *Geophys. Res. Lett., 21,* 1759, 1994.

Tascione, T. F., *Introduction to the Space Environment*, Orbit Book Company, Malablar, Flor., 1988.

Zhu, L., and J.R. Kan, Effects of ionospheric recombination time scale on the auroral signature of substorms, *J. Geophys. Res. 95,* 10389, 1990.

Zhu, L., J. J. Sojka, R. W. Schunk, and D. J. Crain, A time-dependent model of polar cap arcs, *J. Geophys. Res., 98,* 6139, 1993.

World Data Center C2 for Geomagnetism, *Data Catalogue No. 23*, Kyoto University, Kyoto, Japan, 1993.

APPENDICES

APPENDIX A: TWIN VORTICES CASE 1

This appendix contains contour plots for the magnetic field caused by ionospheric currents from the traveling convection twin vortices model. The plots are for case 1, which had an upward field-aligned current leading, at 1 min and 3 min. Output from the full 221 grid point (east-west) by 95 grid point (north-south) is presented first, followed by the output from the simulated Scandinavian magnetometer network.
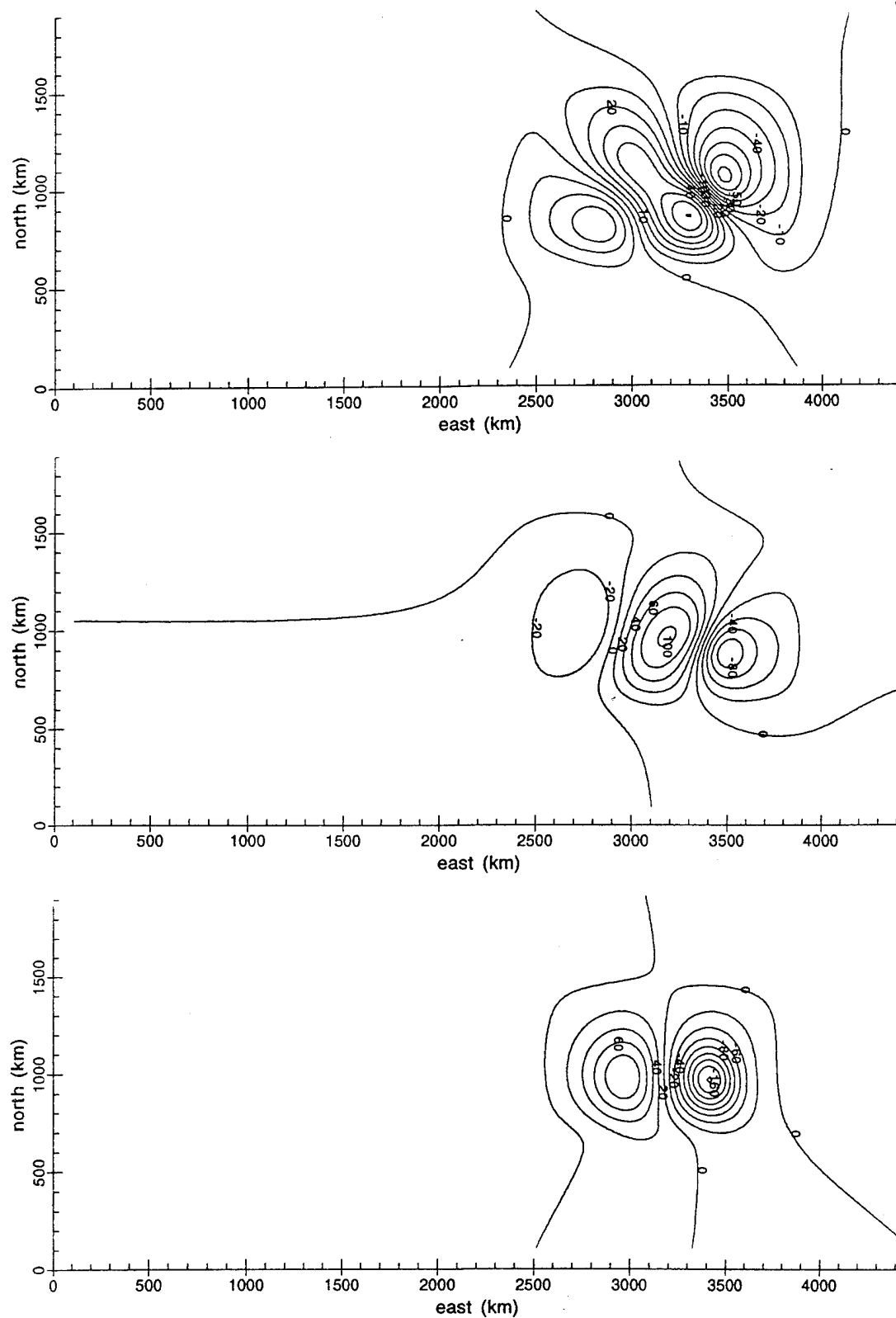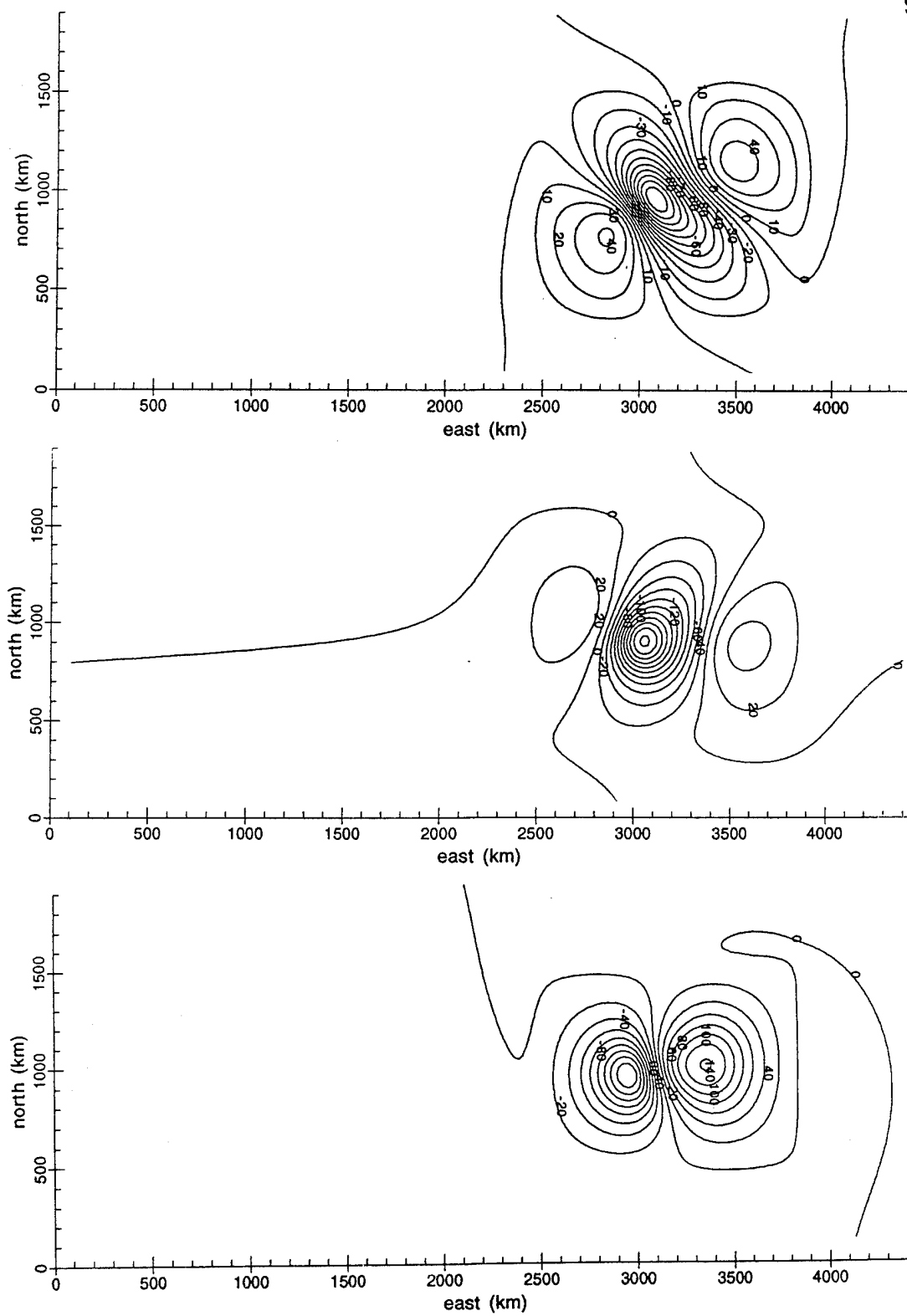
Figure A1: H (top), D (middle), and Z (bottom) components of case 1 at 1 min, in nT.
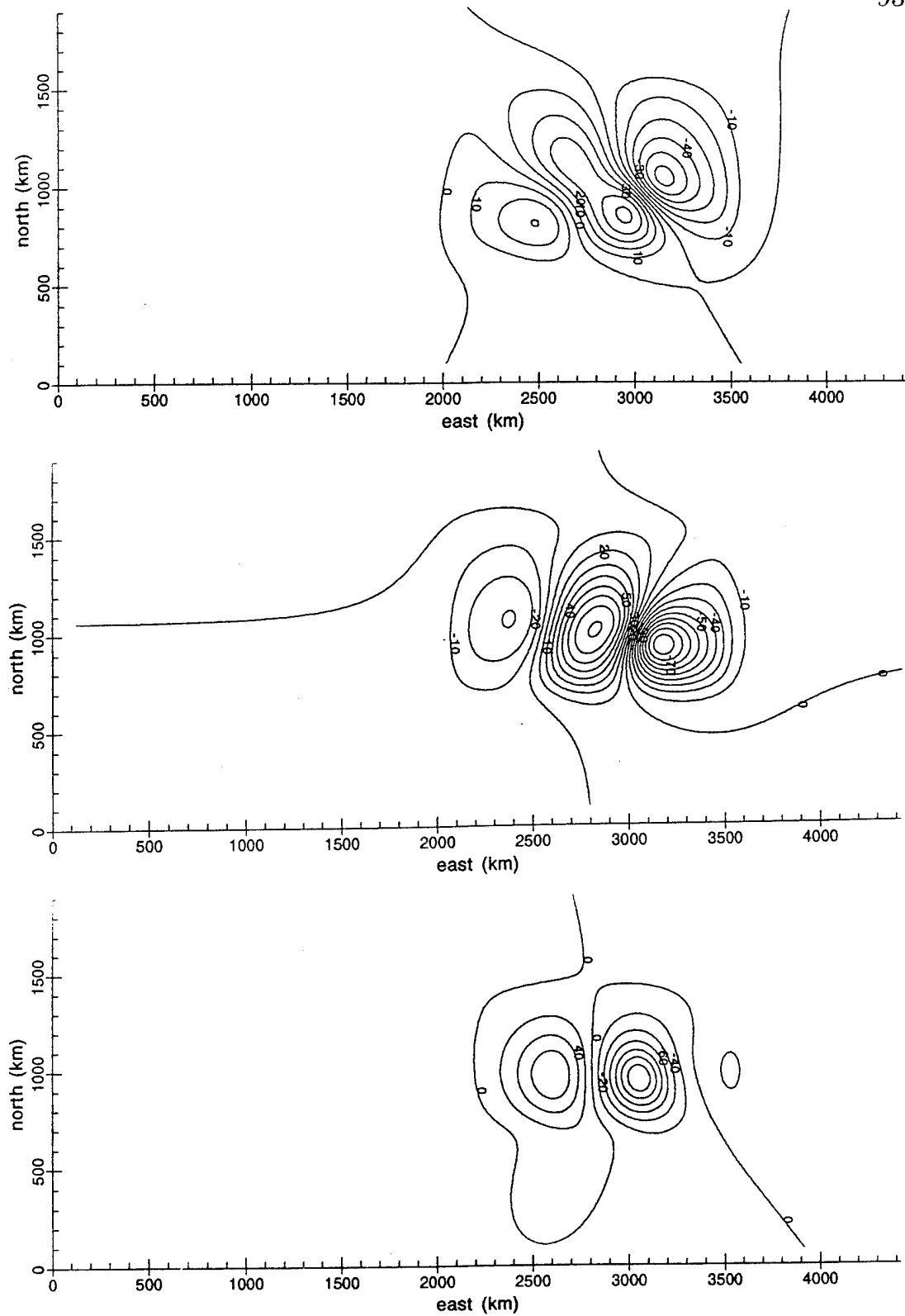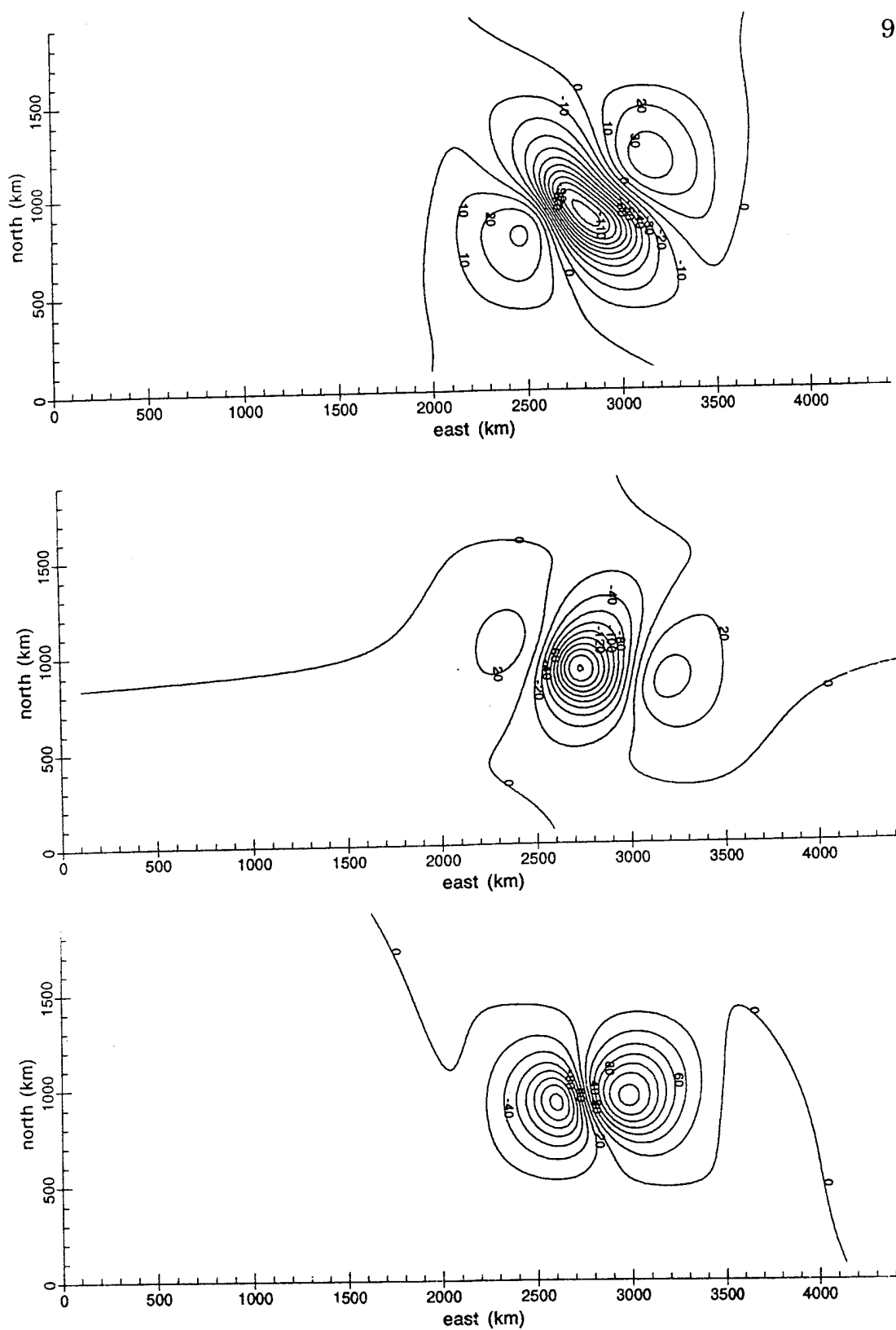
Figure A2: H (top), D (middle), and Z (bottom) components of case 1 at 3 min, in nT.
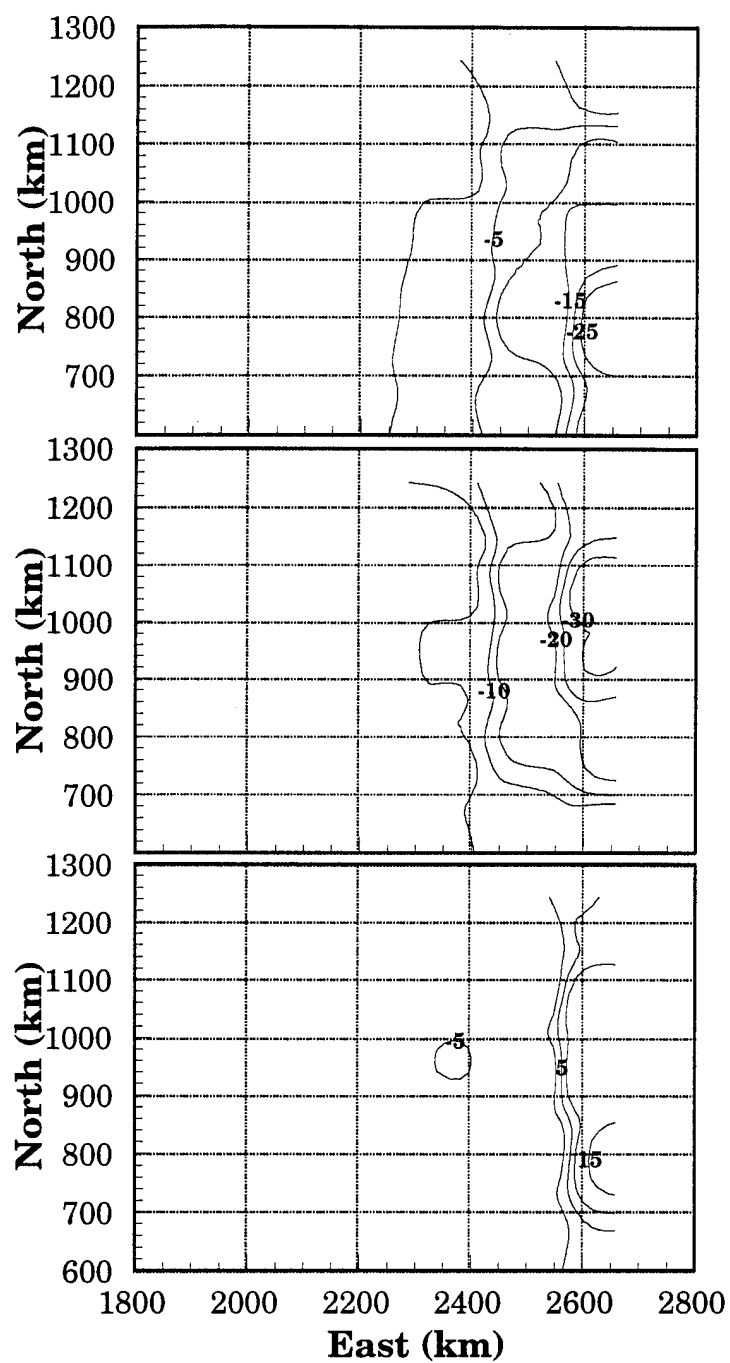
Figure A3: H (top), D (middle), and Z (bottom) components of case 1 at 1 min. Contours created from modeled station data, and are in nT.
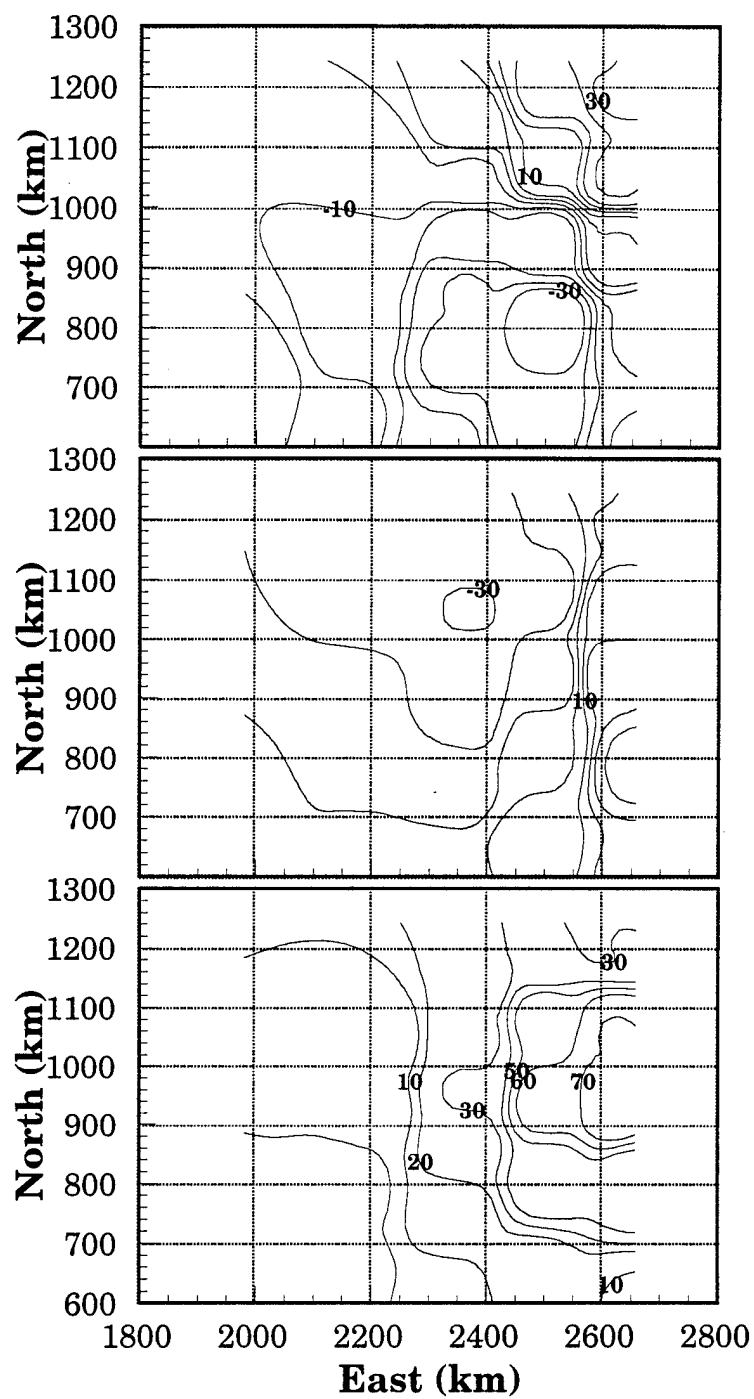
Figure A4: H (top), D (middle), and Z (bottom) components of case 1 at 3 min. Contours created from modeled station data, and are in nT.

APPENDIX B: TWIN VORTICES CASE 2

This appendix contains contour plots for the magnetic field caused by ionospheric currents from the traveling convection twin vortices model. The plots are for case 2, which had an downward field-aligned current leading, at 1 min and 3 min. Output from the full 221 grid point (east-west) by 95 grid point (north-south) is presented first, followed by the output from the simulated Scandinavian magnetometer network.

Figure B1: H (top), D (middle), and Z (bottom) components of case 2 at 1 min, in nT.

Figure B2: H (top), D (middle), and Z (bottom) components of case 2 at 3 min, in nT.
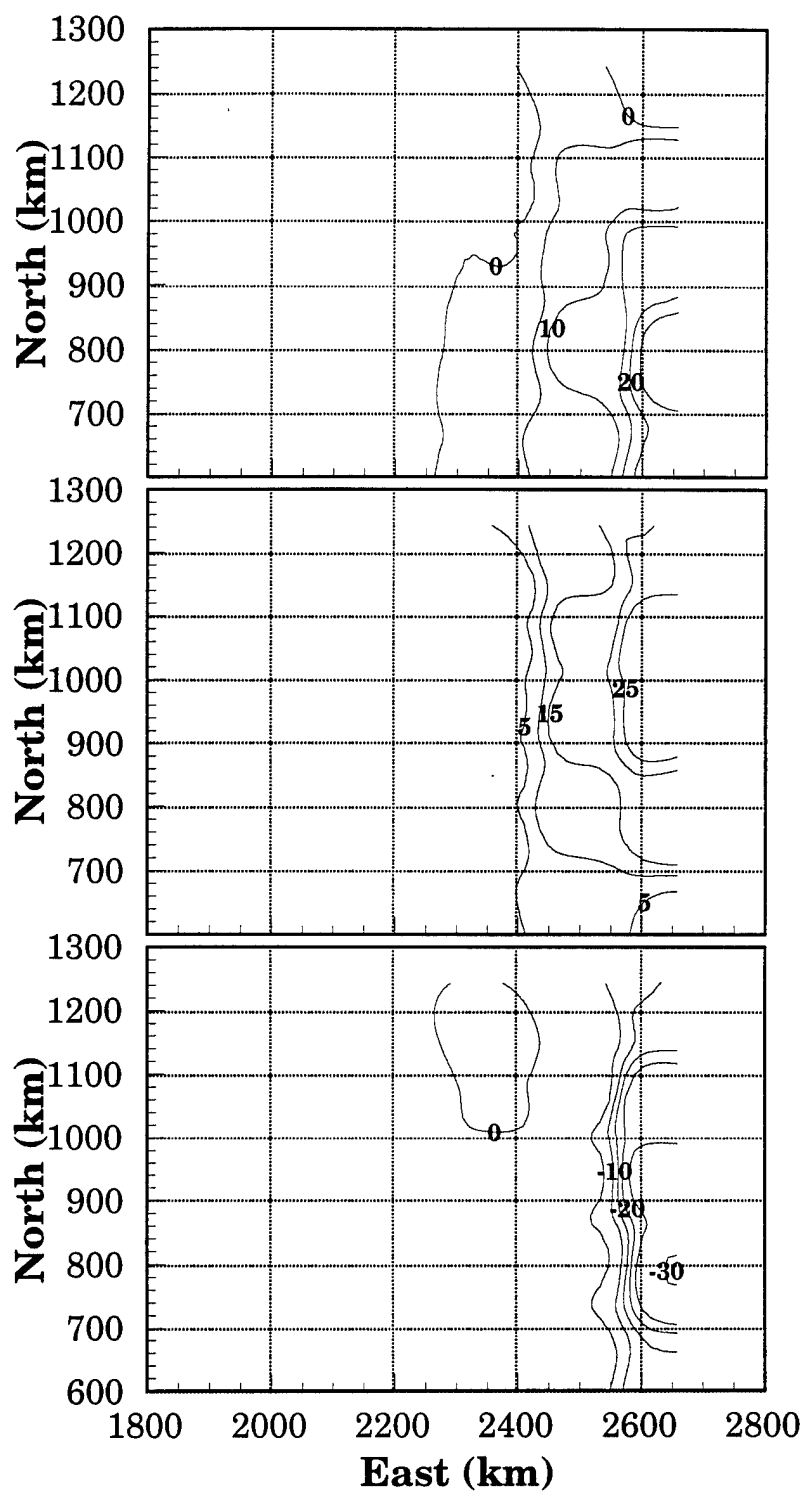
Figure B3: H (top), D (middle), and Z (bottom) components of case 2 at 1 min. Contours created from modeled station data, and are in nT.
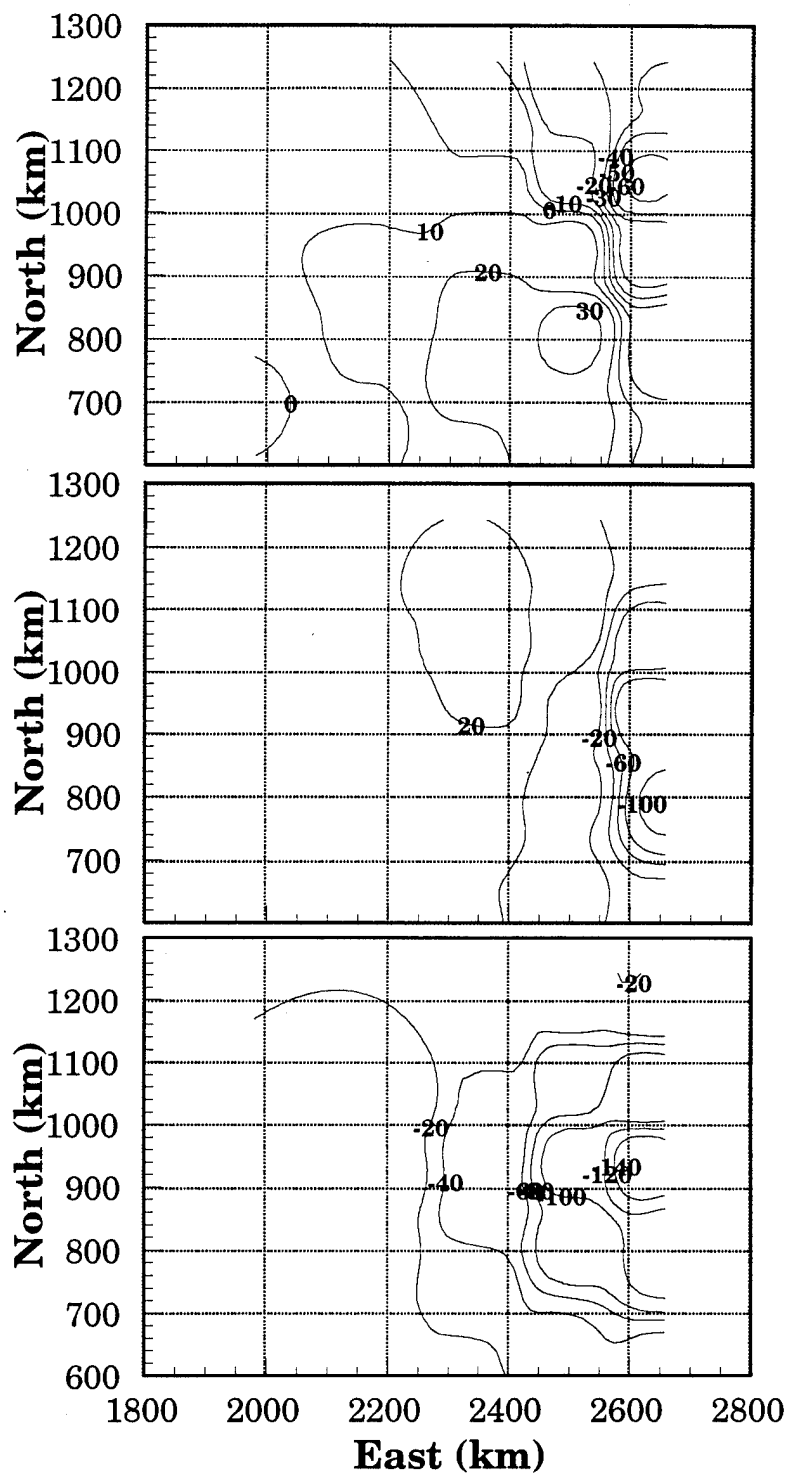
Figure B4: H (top), D (middle), and Z (bottom) components of case 2 at 3 min. Contours created from modeled station data, and are in nT.

APPENDIX C: TWIN VORTICES CASE 3

This appendix contains contour plots for the magnetic field caused by ionospheric currents from the traveling convection twin vortices model. The plots are for case 3, which had an upward field-aligned current leading with no field-aligned current decay, at 1 min and 3 min. Output from the full 221 grid point (east-west) by 95 grid point (north-south) is presented first, followed by the output from the simulated Scandinavian magnetometer network.
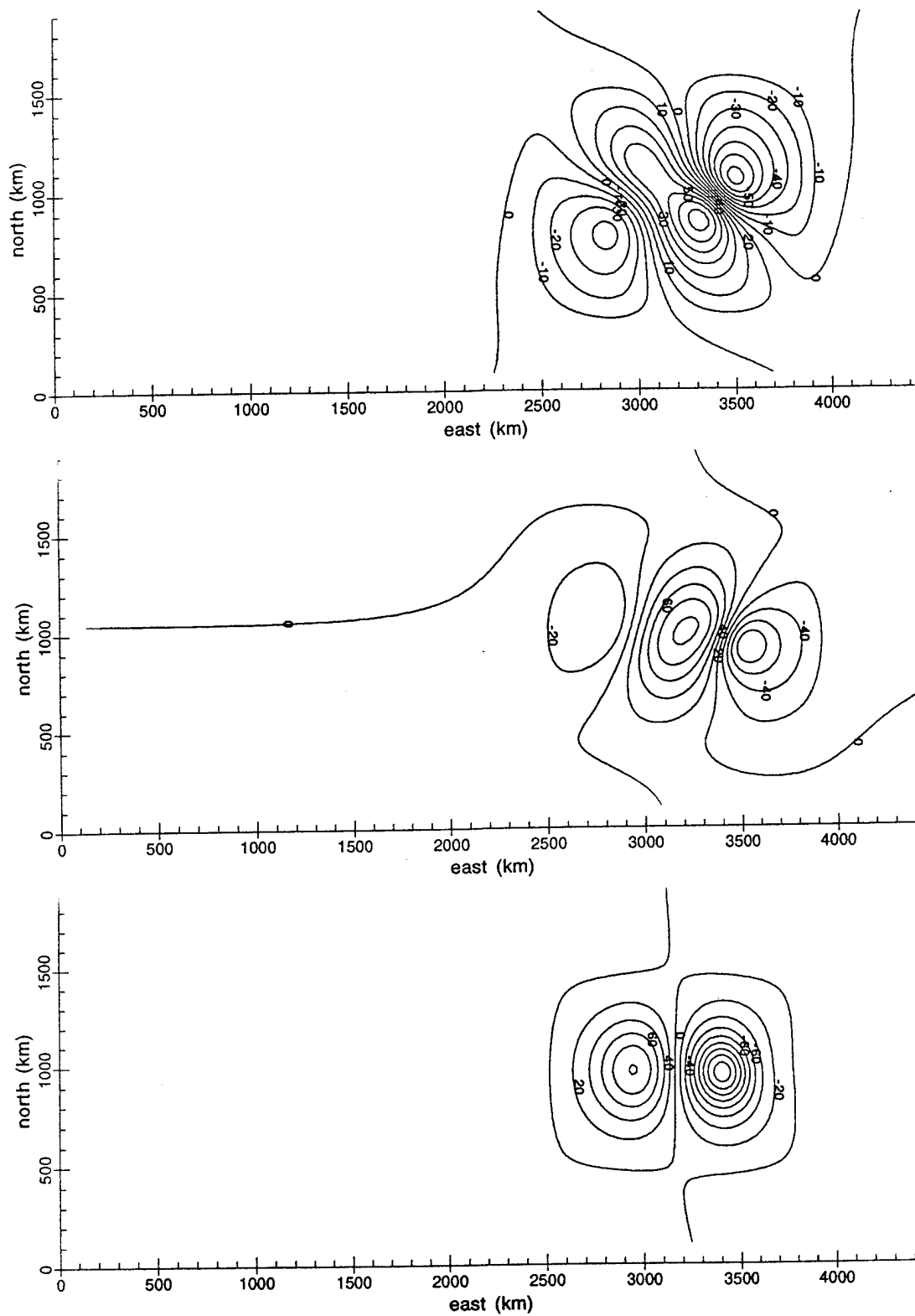
Figure C1: H (top), D (middle), and Z (bottom) components of case 3 at 1 min, in nT.
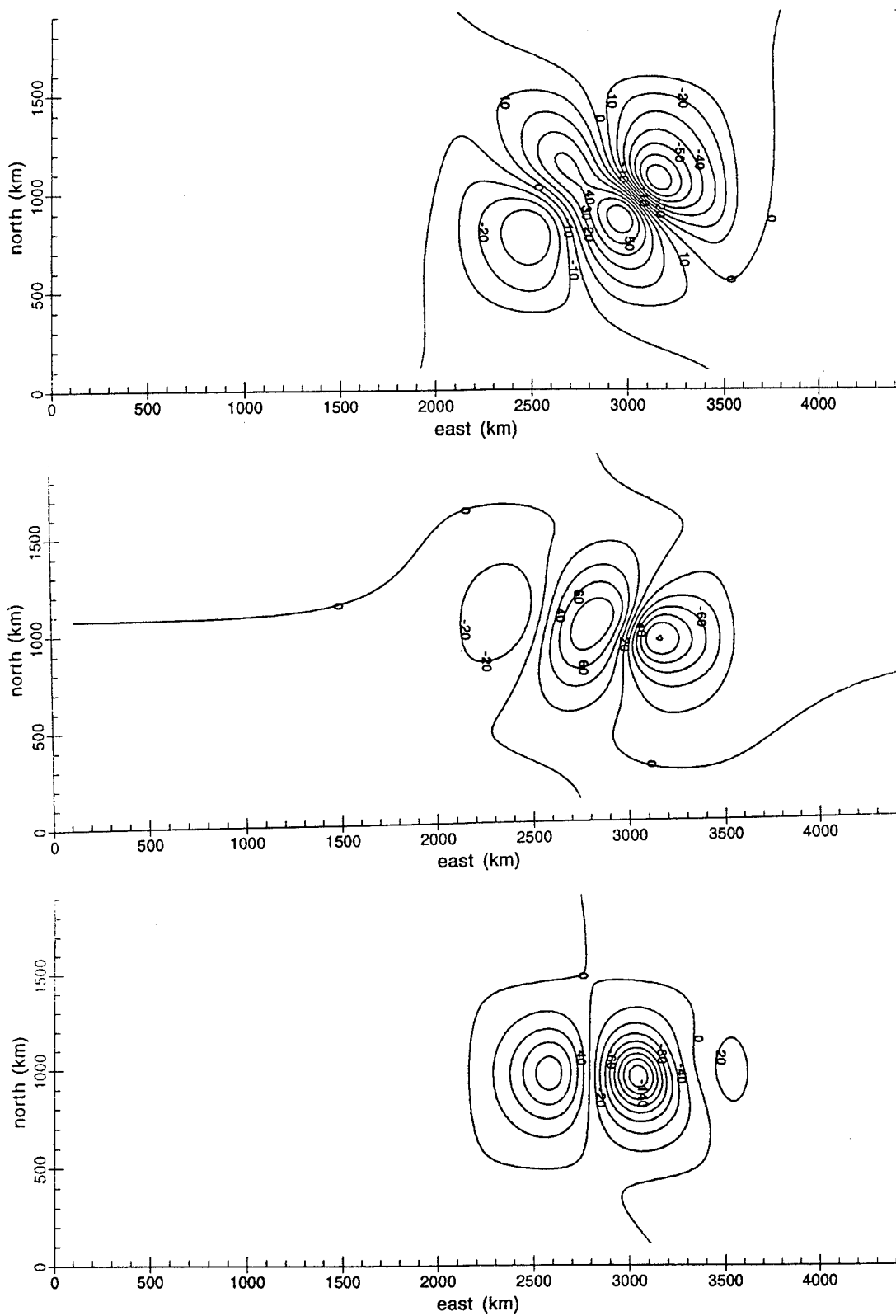
Figure C2: H (top), D (middle), and Z (bottom) components of case 3 at 3 min, in nT.
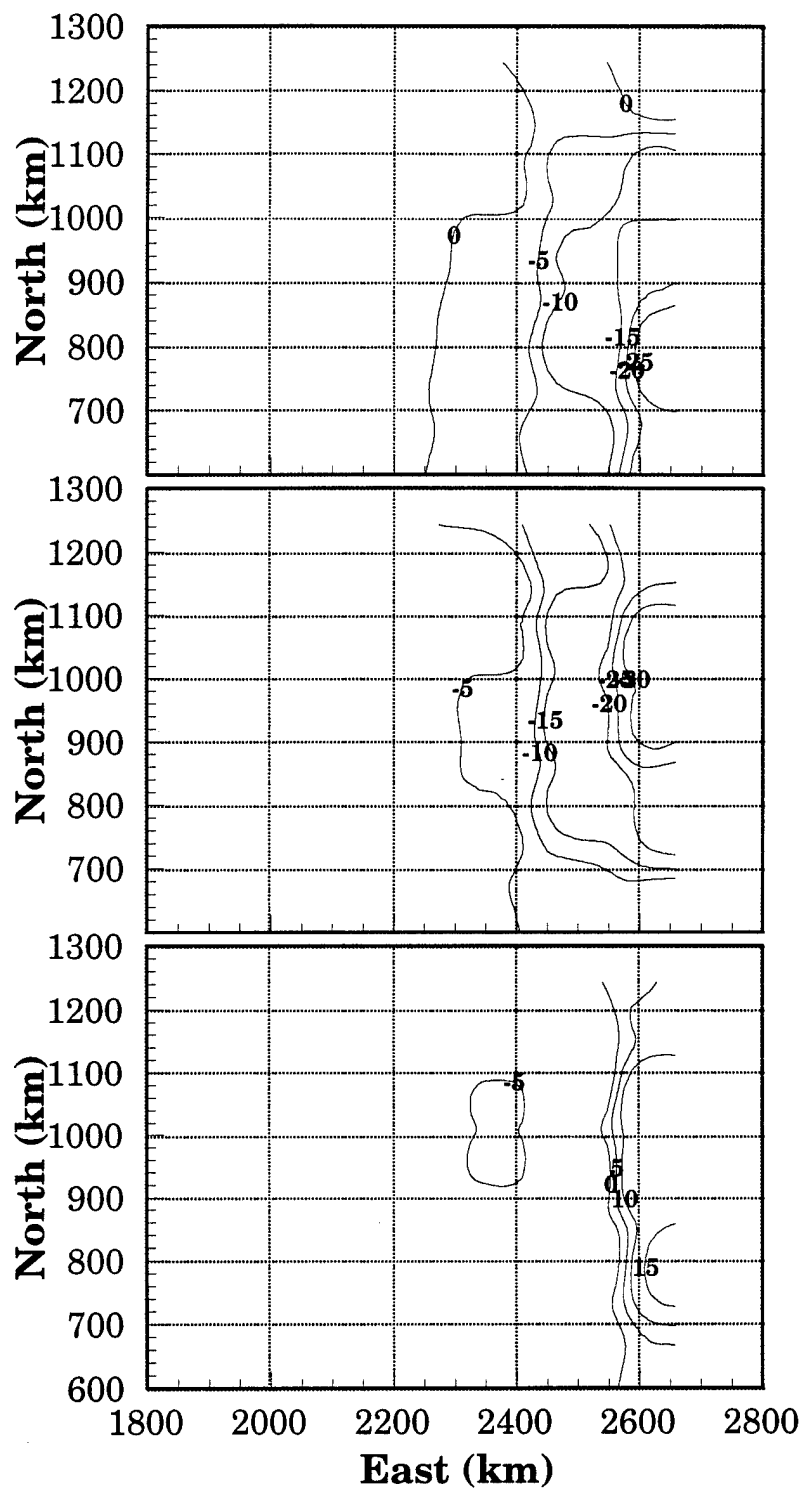
Figure C3: H (top), D (middle), and Z (bottom) components of case 3 at 1 min. Contours created from modeled station data, and are in nT.
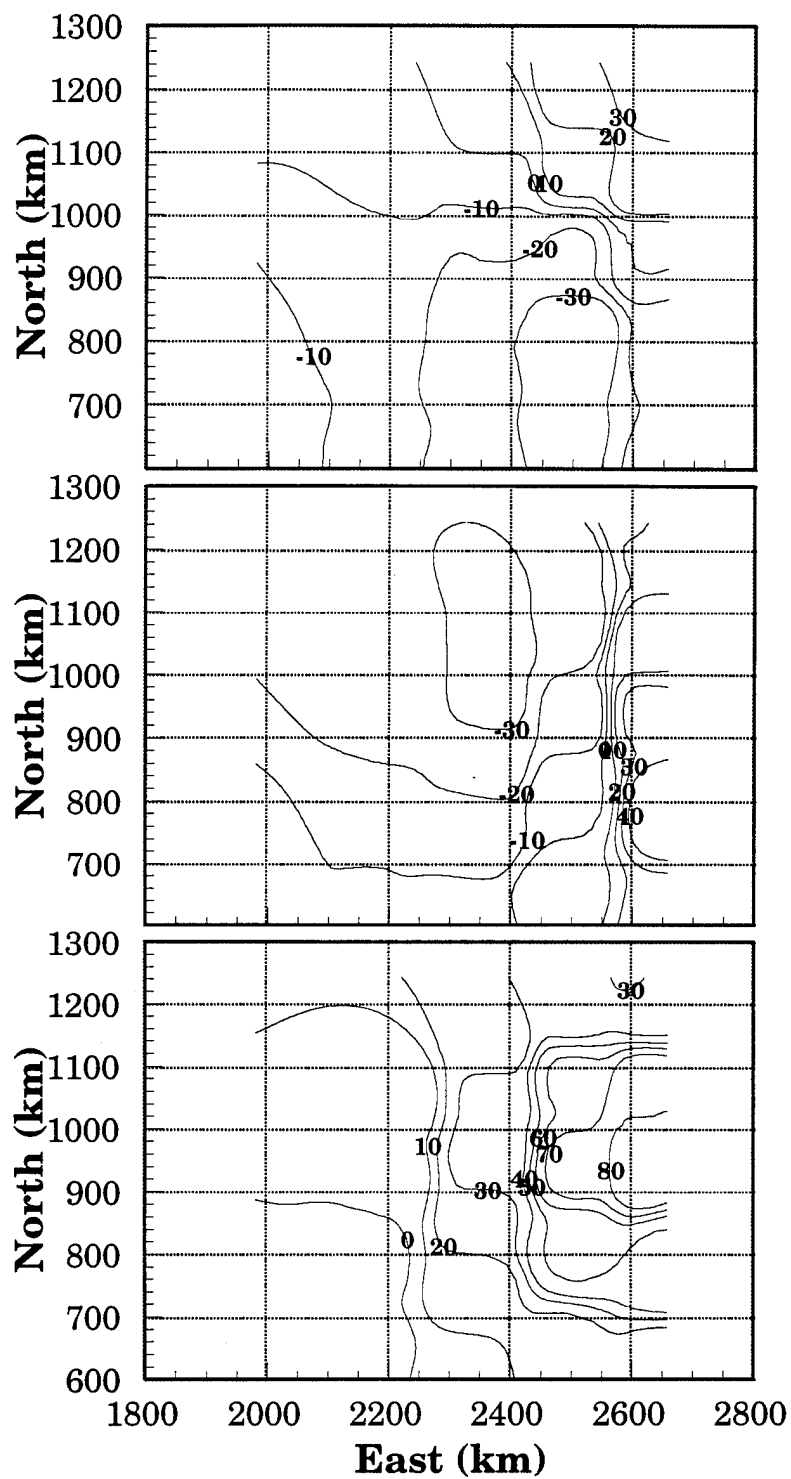
Figure C4: H (top), D (middle), and Z (bottom) components of case 3 at 3 min. Contours created from modeled station data, and are in nT.

APPENDIX D: A BRIEF LOOK AT CORRELATION COEFFICIENTS

Correlation coefficients are relied upon to determine the accuracy of the reconstruction of the ground magnetic signature using data from the simulated stations. A closer examination of the meaning, strengths, and weaknesses of correlation coefficients is in order to better understand the results presented in the text.

The formula for correlation coefficients is

$$\rho = \frac{1}{n-1} \sum \left(\frac{x - \bar{x}}{s_x} \right) \left(\frac{y - \bar{y}}{s_y} \right) \tag{7}$$

where ρ is the correlation coefficient, n is the number of data points, x and y are the values from the data sets with $\bar{x}$ and $\bar{y}$ being the average of the x data set and y data set respectively, s_x is the standard deviation for the x values, and s_y is the standard deviation for the y values. The correlation coefficient is a measure only of the linear association of the two data sets. Its range is from -1 to 1, with these extreme values occurring only in the case of perfect linear association and 0 occurring when the two sets are completely independent of each other. The correlation coefficient does not depend on units, as any dimensions are removed when the values are divided by the
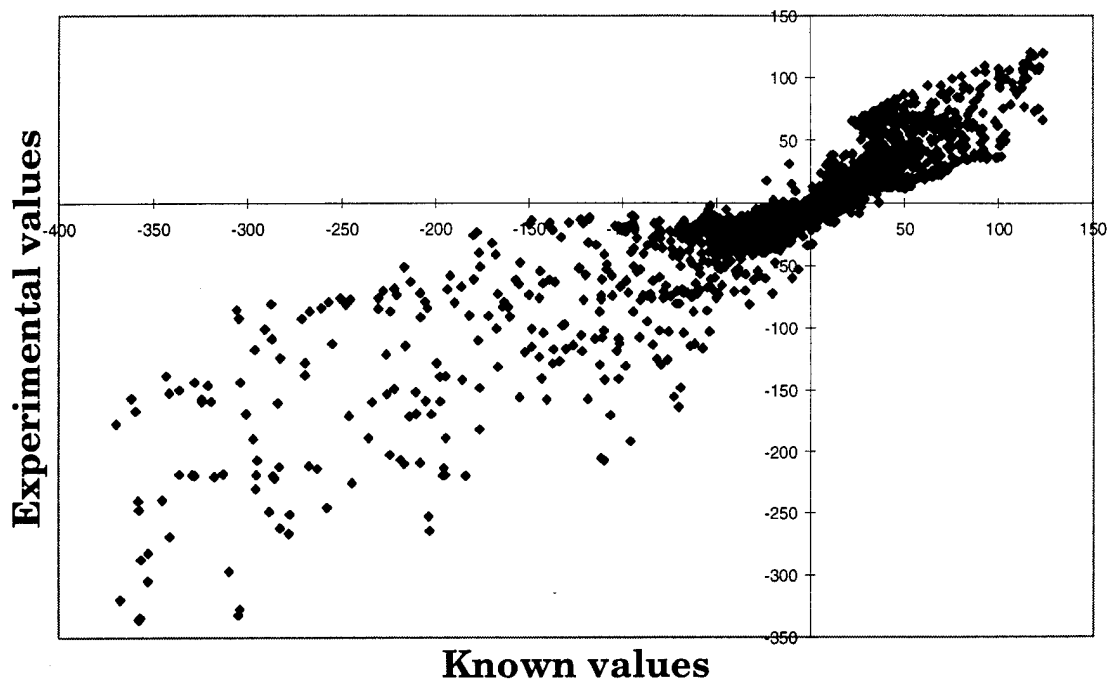
Figure D1: Scatter plot of two data sets.

standard deviation. It is important to note that adding the same value to all values of one data set will not change the correlation [*Moore and McCabe*, 1993].

As an example of how the correlation coefficient works, data from Chapter V will be examined. Figure D1 (identical to Figure 51) above shows a scatter plot between two sets of data: the known data set and the experimental data set. If these two data sets were perfectly correlated, the graph would be a straight line through the origin with a slope of 1. These

data are not perfectly correlated, however, and the coefficient is 0.8974. This is close to 1, and may give the impression that the two data sets are nearly identical. This is not the case; as discussed earlier, adding a constant to all values of one data set does not change the correlation coefficient. The two sets could have very different magnitudes, yet still have a high correlation coefficient.
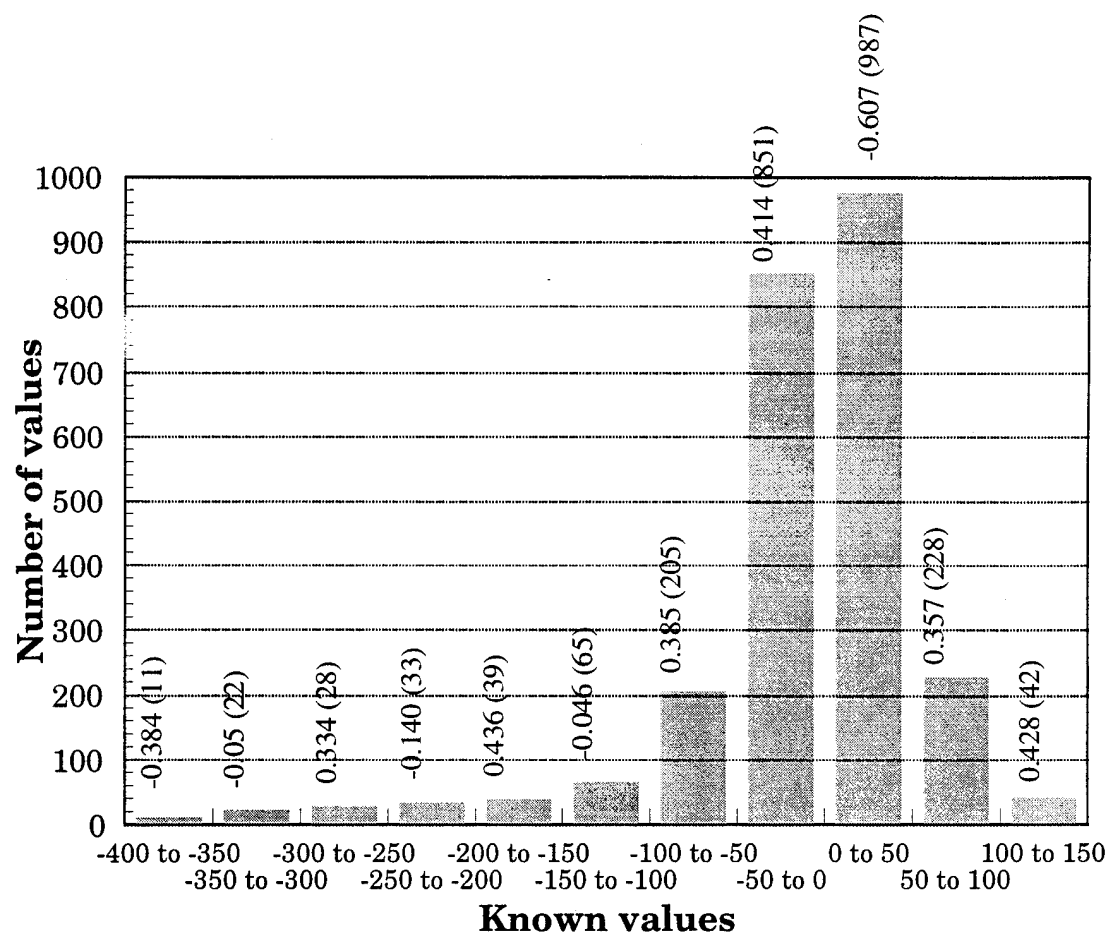

Figure D2: Histogram of known values from Figure D1.

To illustrate this further, Figure D2 shows a histogram of the values from the known data set. Above each bin is the correlation coefficient for that bin with its corresponding experimental values; the number in parenthesis is the number of data points. It is quite obvious that no single bin has a correlation coefficient close to the 0.89 obtained for the full data set. In fact, the third bin from the right (from 0 to 50 nT) has a definite negative correlation. It would appear from this way of presenting the data that there is a very poor correlation between the two data sets. Which method, then, presents an accurate description of the relationship between the two data sets? A good analogy to this situation is a picture on a computer screen. When viewing the whole picture, it will look fine. Increasing the magnification to the point where individual pixels are visible renders the picture unrecognizable. No information has been lost between the two views, yet they look quite different. Figure D3 shows what happens when the "magnification is decreased" from Figure D2, and correlation coefficients are calculated for larger samples. Neighboring pairs of bins were correlated together (with the exception of the first 3 bins, which were correlated together), making apparent the trend towards larger coefficients with more complete data samples. This trend continues until all the data are correlated together, giving the correlation coefficient of 0.89.
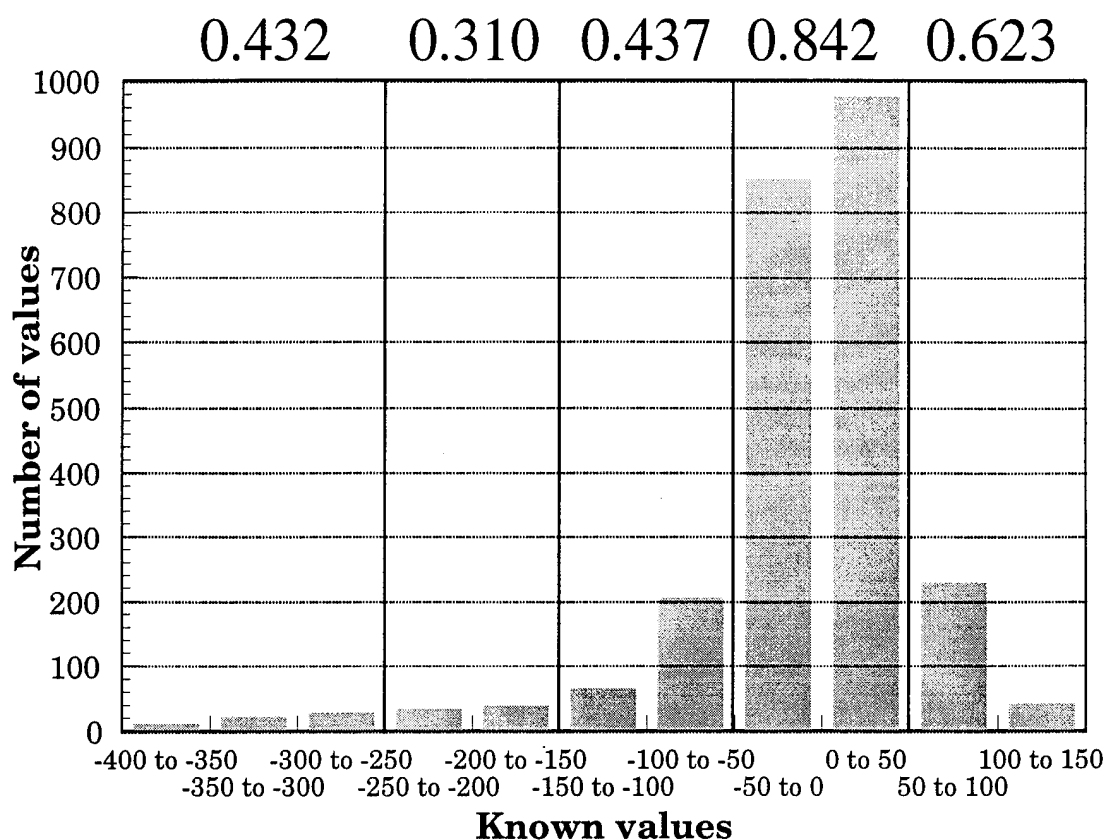
Figure D3: Correlation coefficients for groups of bins. Coefficients are located along top of chart.

The high correlation coefficient for the complete data sets indicates there is a strong relationship between the two data sets. Taken as a whole, the experimental data set was able to capture the patterns and trends of the known data set. This does not mean, however, that the values of the points in the experimental data set have the same magnitude as the values in the known data set, as adding a constant to all values of one data set will not

affect the correlation coefficient. The low correlation coefficients for individual bins demonstrates that smaller samples do not contain enough information about the whole pattern to give an accurate reconstruction. The two largest bins have individual correlation coefficients of 0.414 and -0.607, but when the data from the two are combined the coefficient jumps dramatically to 0.842. The bottom line of all this is correlation coefficients approaching 1 indicate there are strong similarities in the behavior of the data sets; the correlation coefficient cannot be used to infer anything about the relative magnitudes of the points in the data sets.

APPENDIX E: PLOTS OF SCANDINAVIAN STATIONS

MOVED RELATIVE TO TWIN VORTICES

These plots are a continuation similar to Figure 36, where the Scandinavian stations were moved relative to the modeled traveling convection twin vortices. This was done to determine what effects position would have on the ability of the stations to resolve the magnetic field. These figures can be compared with Figure 34.
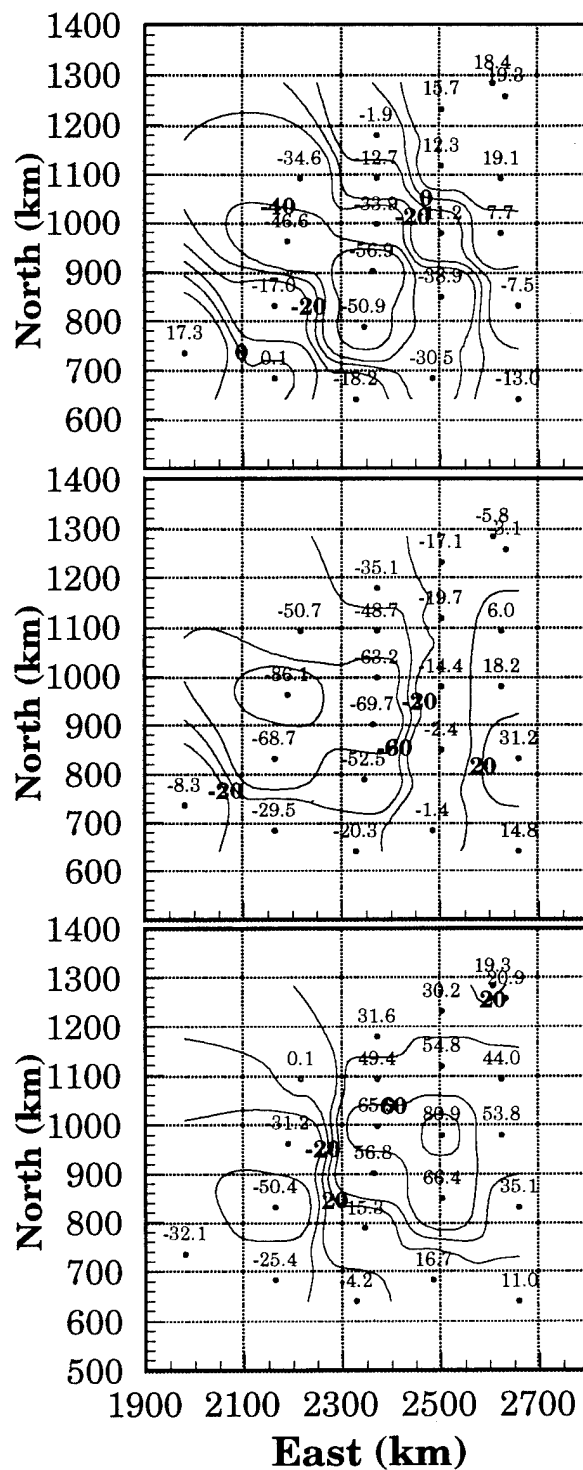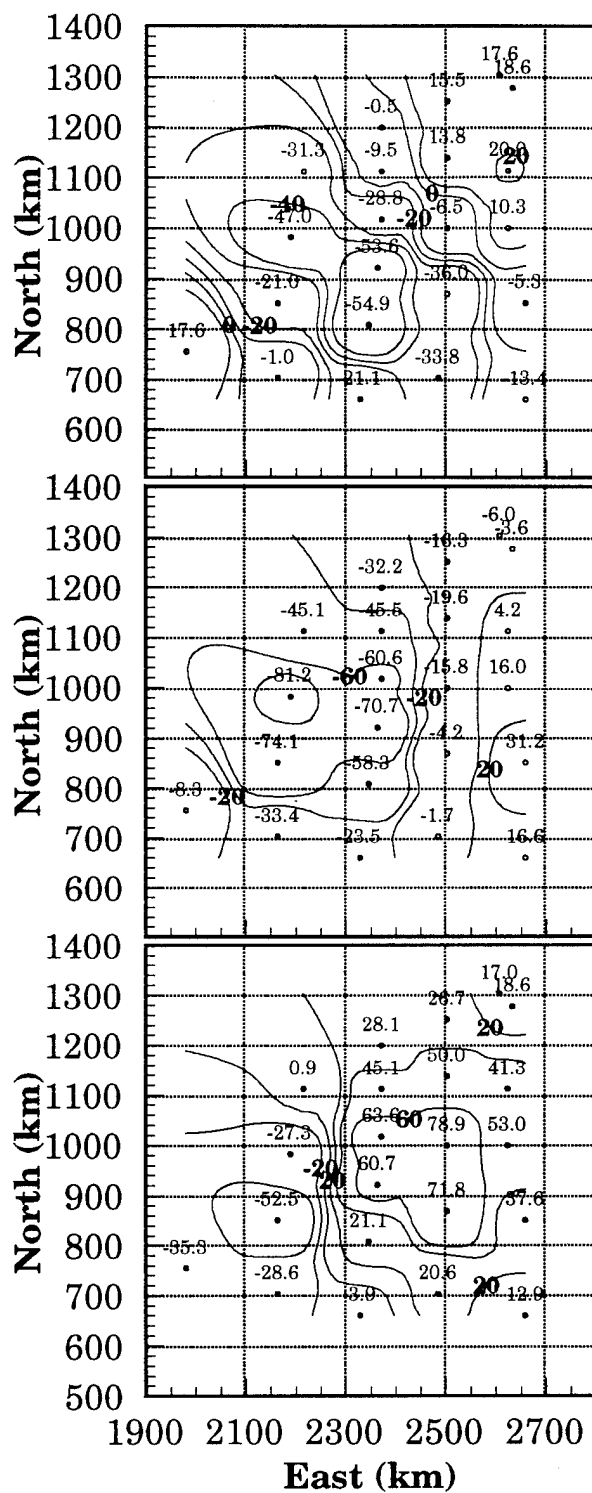
Figure E1: H (top), D (middle), and Z (bottom) components for case 2 at 6 min. Stations shifted 40 km to the north. Contours in nT.
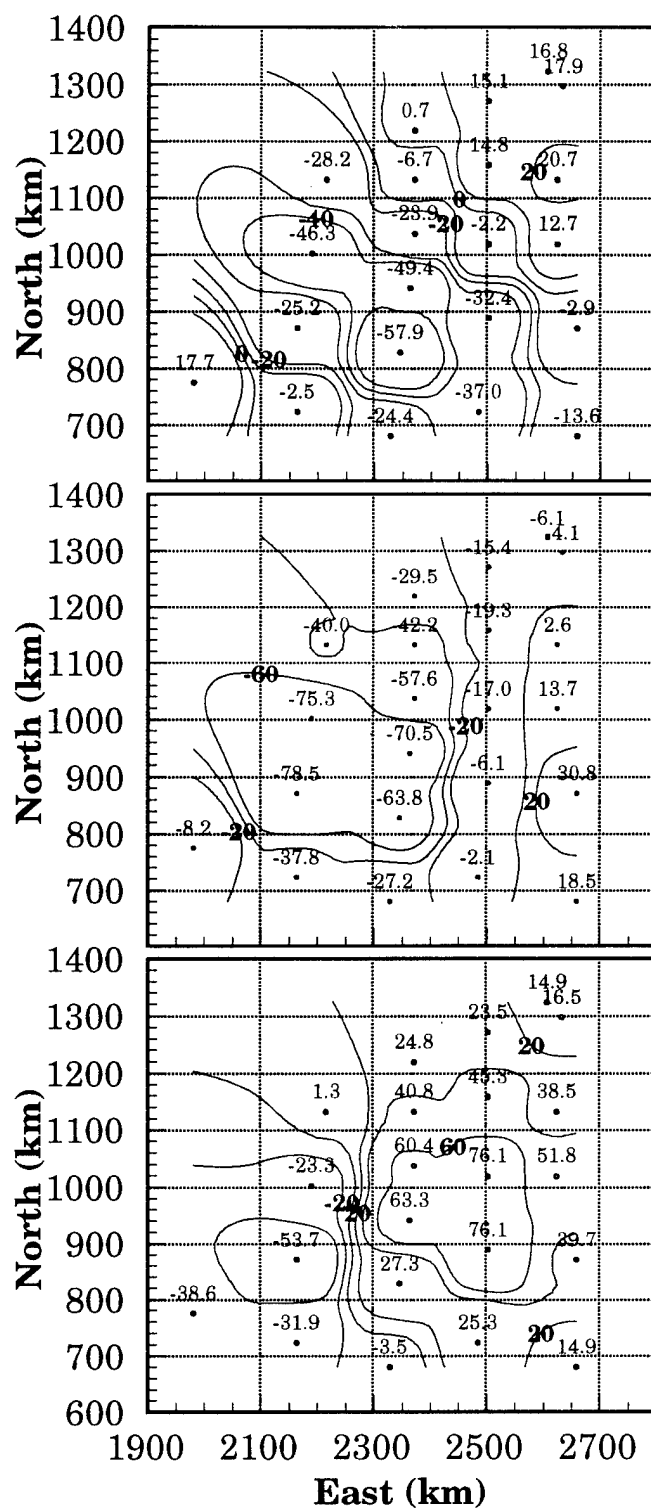
Figure E2: H (top), D (middle), and Z (bottom) components for case 2 at 6 min. Stations shifted 60 km to the north. Contours in nT.

Figure E3: H (top), D (middle), and Z (bottom) components for case 2 at 6 min. Stations shifted 80 km to the north. Contours in nT.
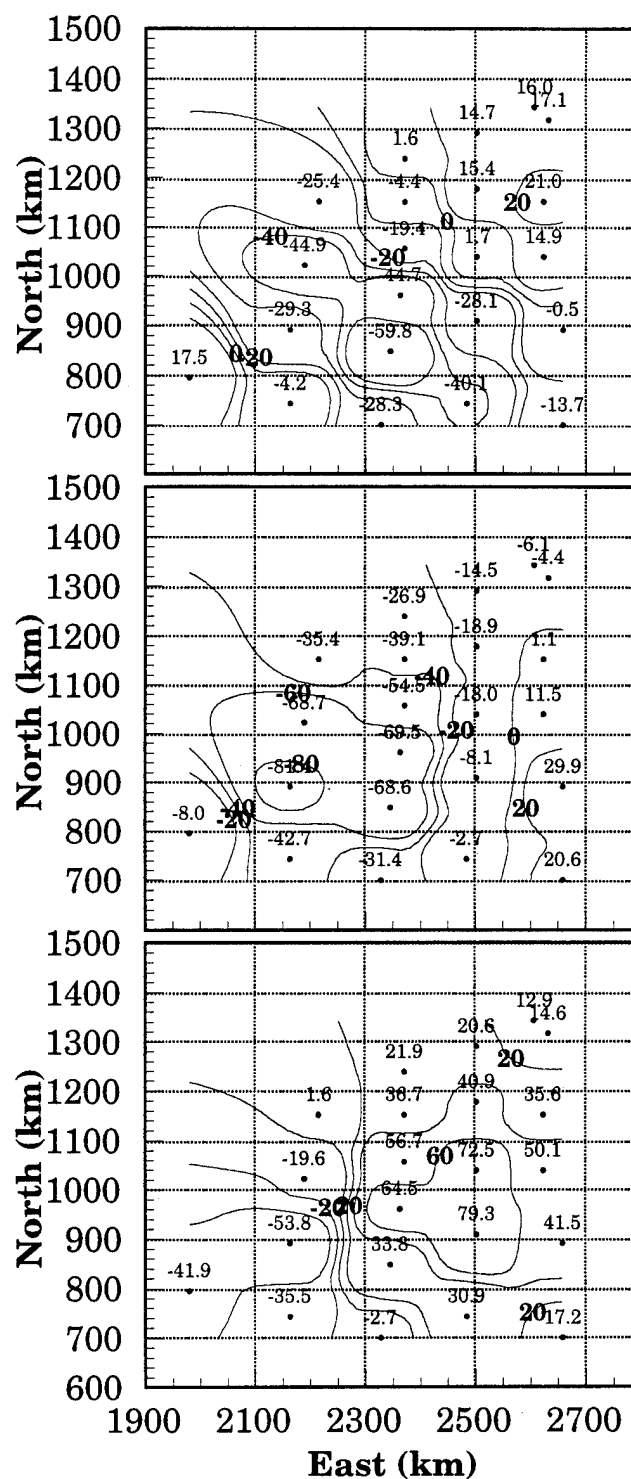
Figure E4: H (top), D (middle), and Z (bottom) components for case 2 at 6 min. Stations shifted 100 km to the north. Contours in nT.

APPENDIX F: ADDITIONAL ROTATIONS FOR 195 STATIONS

This appendix contains contour plots for the magnetic field caused by ionospheric currents from the global substorm model. Rotations presented here are 120°, 190° or "best" rotation, and 240°. Data were recorded by the 195 magnetometer distribution. Plots can be compared to Figures 40-42.
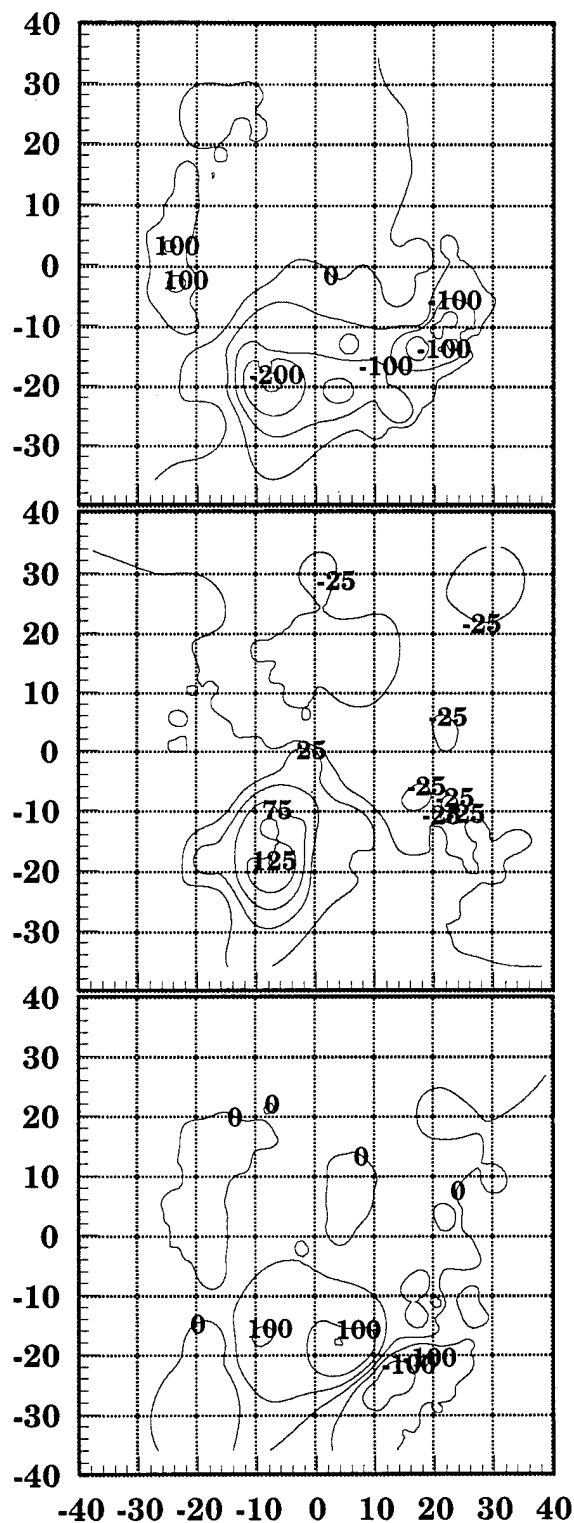
Figure F1: H (top), D (middle), and Z (bottom) components generated using data from 195 stations, 120° rotation. Contours are in nT, axes are in degrees, with the magnetic north pole at 0,0.
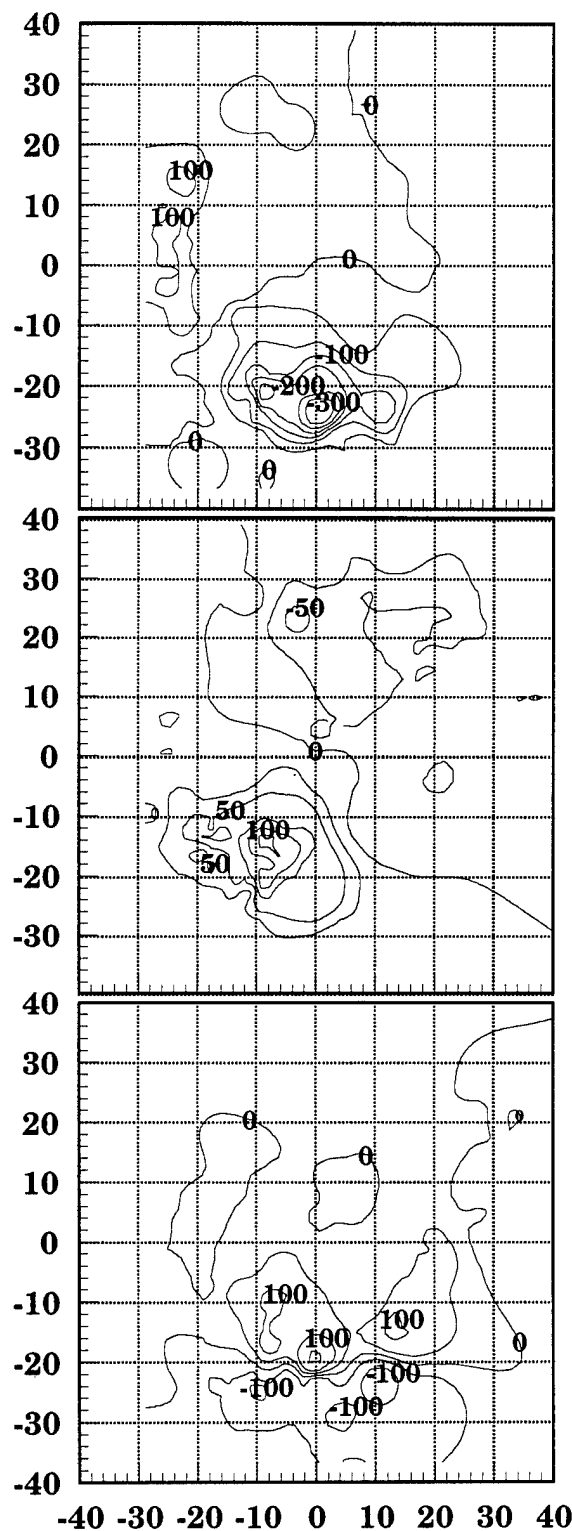
Figure F2: H (top), D (middle), and Z (bottom) components generated using data from 195 stations, 190° or "best" rotation. Contours are in nT, axes are in degrees, with the magnetic north pole at 0,0.
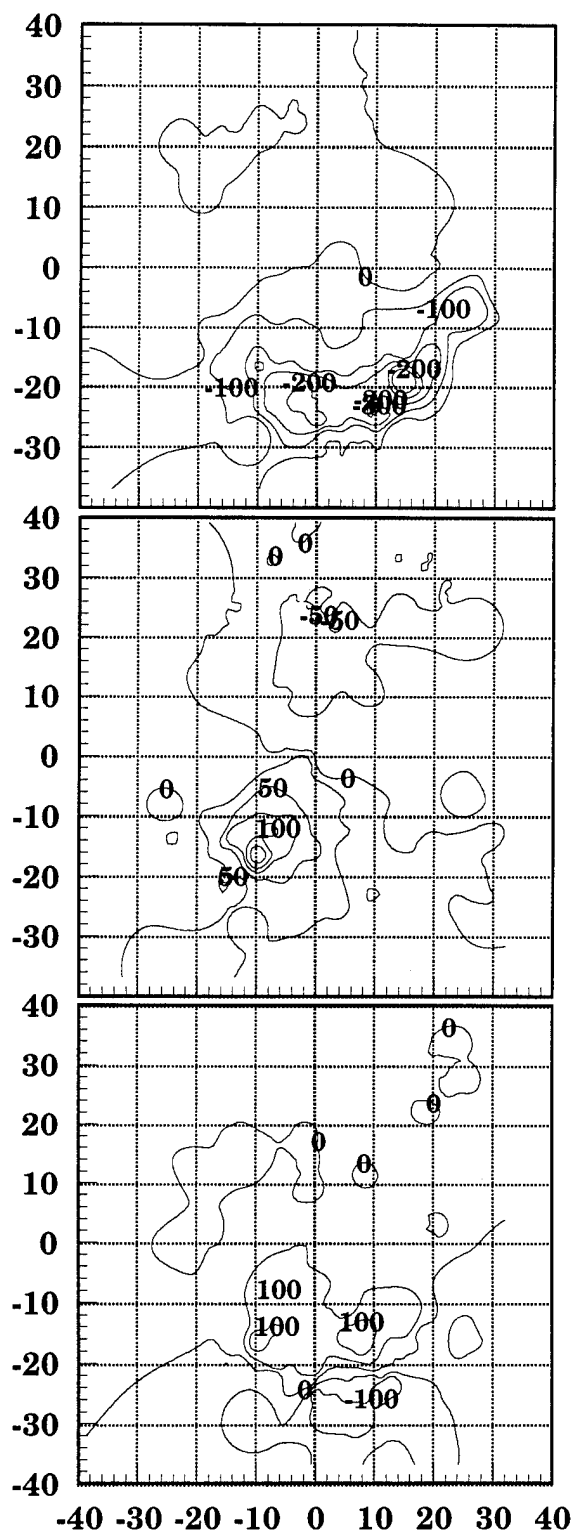
Figure F3: H (top), D (middle), and Z (bottom) components generated using data from 195 stations, 240° rotation. Contours are in nT, axes are in degrees, with the magnetic north pole at 0,0.

APPENDIX G: ADDITIONAL ROTATIONS FOR 226 STATIONS

This appendix contains contour plots for the magnetic field caused by ionospheric currents from the global substorm model. Rotations presented here are 120° and 240°. Data were recorded by the 226 magnetometer distribution. Plots can be compared to Figures 40-42.
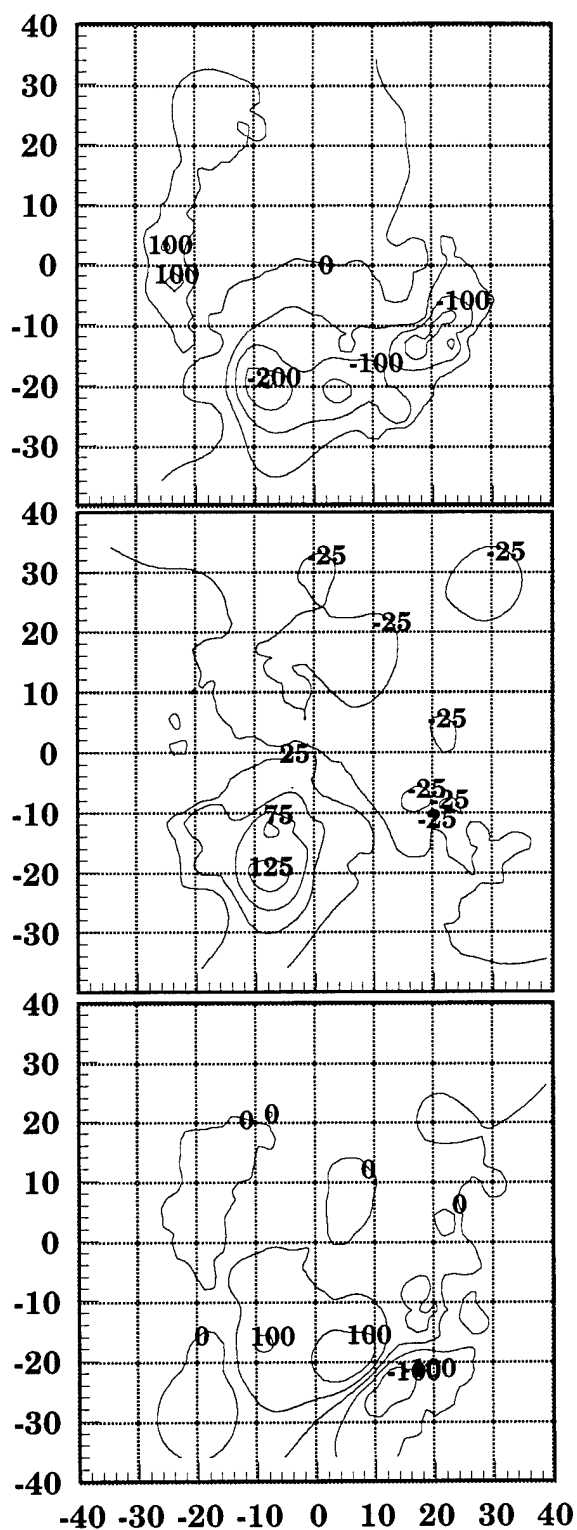
Figure G1: H (top), D (middle), and Z (bottom) components generated using data from 226 stations, 120° rotation. Contours are in nT, axes are in degrees, with the magnetic north pole at 0,0.
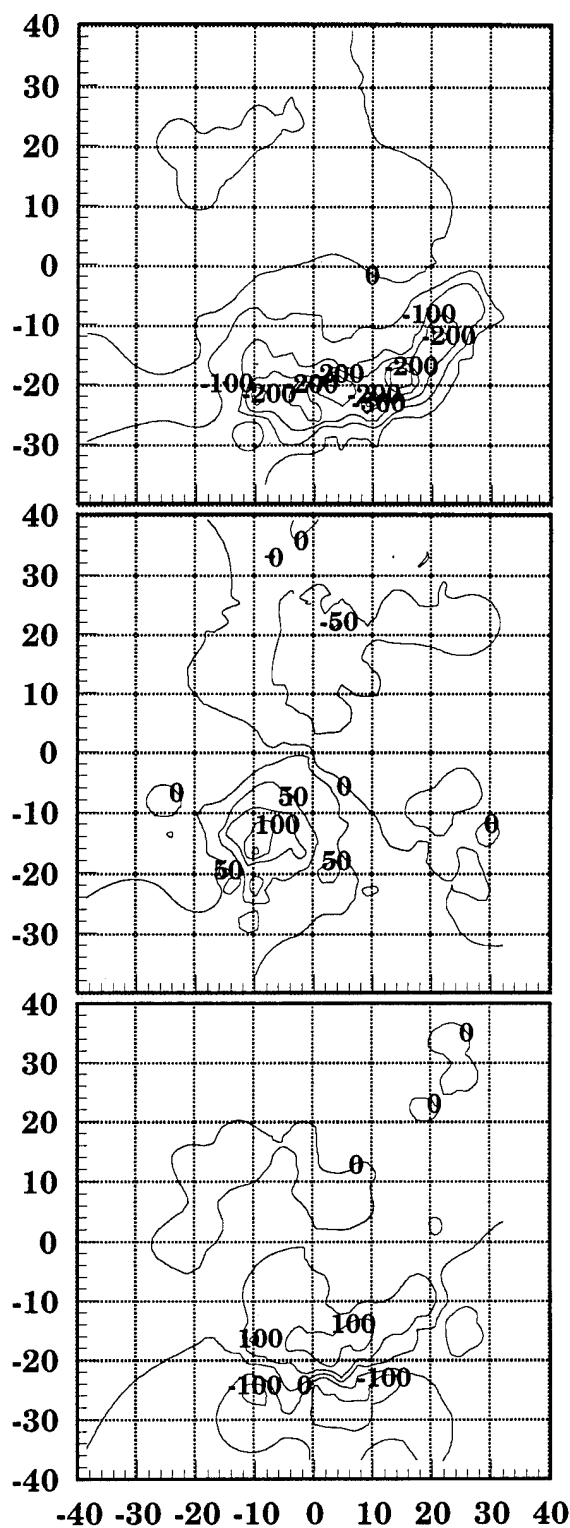
Figure G2: H (top), D (middle), and Z (bottom) components generated using data from 226 stations, 240° rotation. Contours are in nT, axes are in degrees, with the magnetic north pole at 0,0.

APPENDIX H: ADDITIONAL ROTATIONS FOR 276 STATIONS

This appendix contains contour plots for the magnetic field caused by ionospheric currents from the global substorm model. Rotations presented here are 120° and 240°. Data were recorded by the 276 magnetometer distribution. Plots can be compared to Figures 40-42.
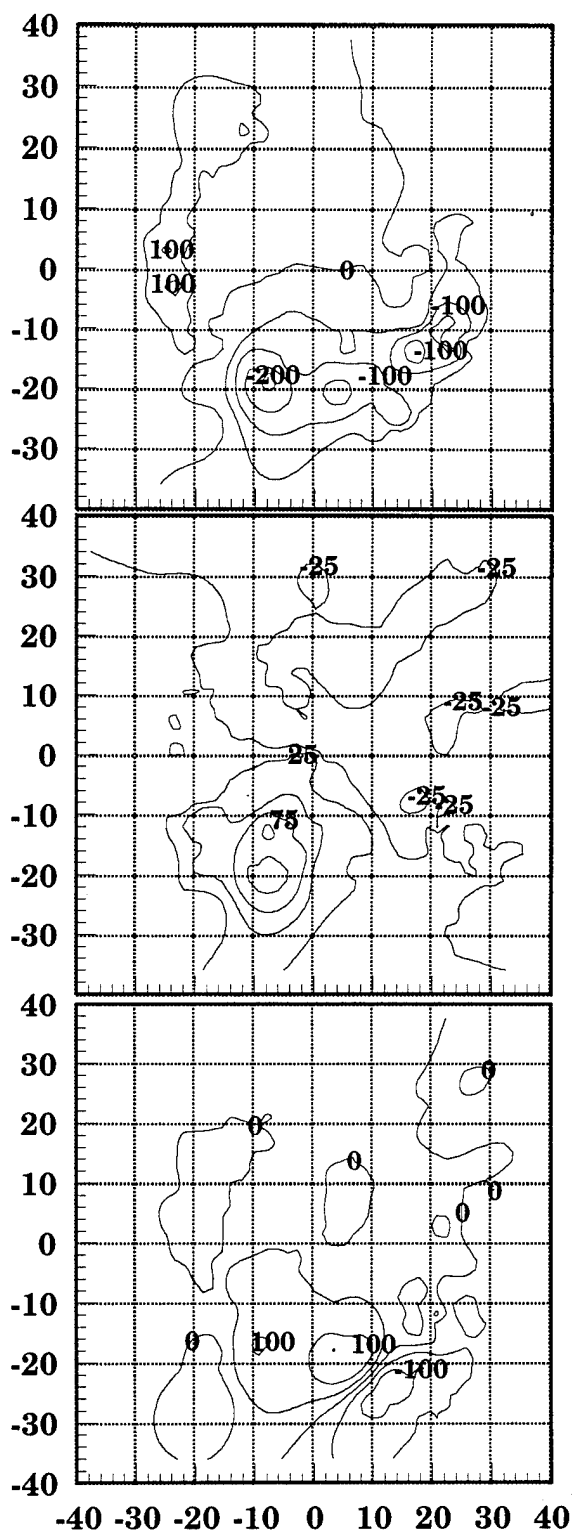
Figure H1: H (top), D (middle), and Z (bottom) components generated using data from 276 stations, 120° rotation. Contours are in nT, axes are in degrees, with the magnetic north pole at 0,0.
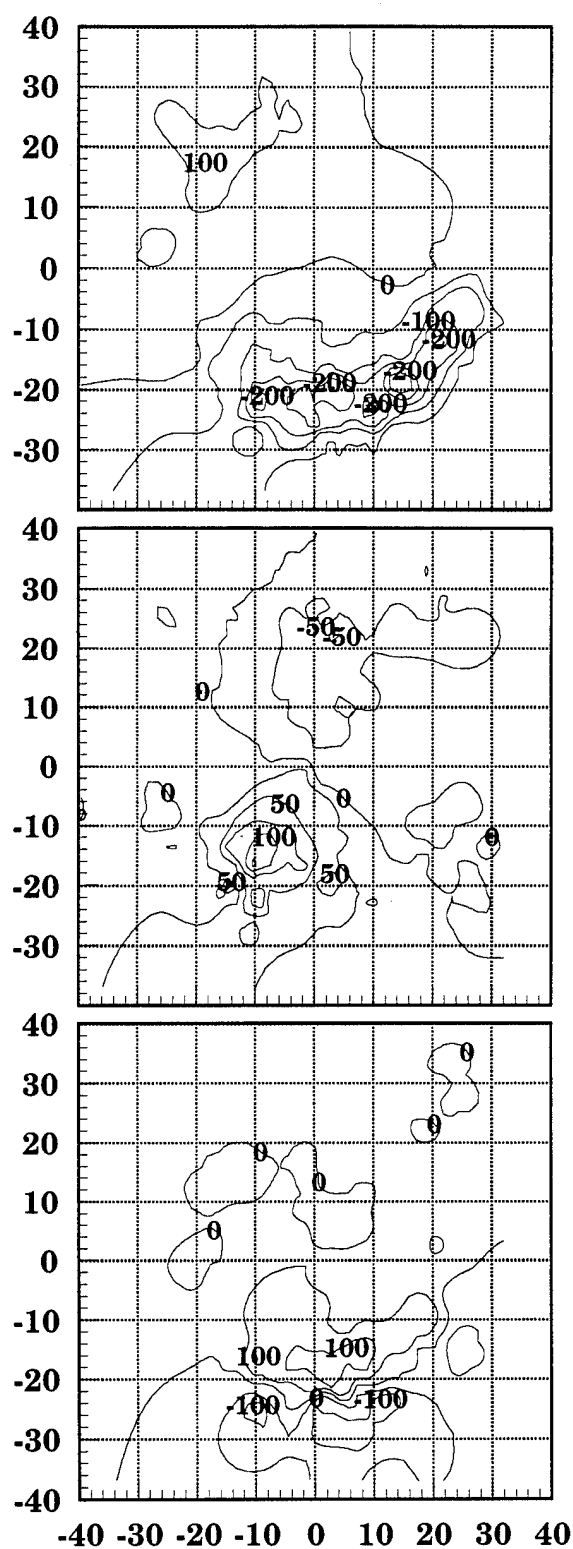
Figure H2: H (top), D (middle), and Z (bottom) components generated using data from 276 stations, 240° rotation. Contours are in nT, axes are in degrees, with the magnetic north pole at 0,0.